

# Accuracy determination of the KATRIN FT-ICR mass spectrometers using ${}^6\text{Li}$ and ${}^7\text{Li}$

Bestimmung der Genauigkeit der KATRIN-FT-ICR-Massenspektrometer mittels  ${}^6\text{Li}$  und  ${}^7\text{Li}$

DIPLOMARBEIT IN PHYSIK VON  
HENDRIK GOLZKE

Bei Prof. Dr. G. Drexlin  
und Prof. Dr. K. Blaum

Institut für experimentelle Kernphysik  
Fakultät für Physik  
Karlsruher Institut für Technologie

In Kooperation mit dem  
Max-Planck-Institut für Kernphysik  
Heidelberg

24. September 2012



# Eidesstattliche Erklärung

Hiermit versichere ich, dass ich die vorliegende Arbeit selbständig verfasst und keine, außer der genannten Quellen und Hilfsmittel benutzt habe.

Heidelberg, 24. September 2012

Ort, Datum

Hendrik Golzke



# Zusammenfassung

Das KARlsruher Tritium Neutrino (KATRIN) Experiment zielt darauf ab, die Neutrinomasse auf 0,2 eV (95 % KI) genau zu bestimmen. Dafür wird die kinetische Energie der  $\beta$ -Elektronen des Tritiumzerfalles nahe des Endpunktes genau vermessen. Die Massendifferenz zwischen Tritium und Helium abzüglich der Masse und maximalen kinetischen Energie des Elektrons ergibt die Neutrinomasse. Damit die nötige Auflösung erreicht werden kann, müssen systematische Effekte klein gehalten werden und sehr gut untersucht sein.

Da Tritium in  ${}^3\text{He}$  zerfällt, aber auch Cluster wie  $\text{T}_3^+$  und  $\text{T}_5^+$  bildet, wird ein breitbandiges Massenspektrometer mit einer Präzision  $\Delta m/m$  von mindestens  $1 \cdot 10^{-4}$  benötigt. Das einzige System, welches dies on-line leisten kann, ist ein breitbandiges Fourier-Transformations-Ionen-Zyklotronresonanz-Massenspektrometer (FT-ICR MS). Hierbei werden Ionen mit einer Penningfalle gefangen und über die Eigenfrequenzen der Teilchenbewegung deren Masse bestimmt. Je eine Penningfalle wird am Ein- und Ausgang der DPS2-F, einer der KATRIN-Pumpsektionen, eingebaut werden und dient dort der Detektion der Teilchen im Strahlrohr und der Überprüfung der Pumpeffizienz beziehungsweise der Reduktion der Ionenanzahl. Die eingesetzten Ionenfallen sind zylindrische Penningfallen, die einen Innendurchmesser von 70 mm haben, um den Strahlquerschnitt beziehungsweise den nutzbaren Flußschlauch des KATRIN-Aufbaus nicht zu verringern.

Das komplette FT-ICR MS System wurde von Stahl-Electronics entworfen und am Max-Planck-Institut für Kernphysik (MPIK) in Heidelberg aufgebaut, erweitert und getestet. Zwei Hauptfallen und eine Ersatzfalle sind komplett zusammengebaut. Beide Hauptfallen sind verkabelt und einsatzbereit. Für die Inbetriebnahme am KATRIN-Experiment sei auf ein bald erscheinendes Handbuch von Stahl-Electronics und die Dissertation von Marta Ubieto Diaz [UD11] verwiesen.

Die vorliegende Arbeit beschäftigt sich zum größten Teil mit einer vom KATRIN-Fallendesign abgeleiteten Falle. Insbesondere auf mögliche Probleme beim Ioneneinfang bei KATRIN und am MPIK wird eingegangen. Die Genauigkeit der Massenbestimmung hängt von der Messmethode ab, wobei in dieser Arbeit mehrere Methoden vorgestellt und verglichen werden. Die systematischen Fehler der Penningfalle im MPIK-Testaufbau wurden vermessen. Abschließend werden die finalen

Funktionstests der KATRIN-Fallen vorgestellt und ein Ausblick auf zukünftige Experimente gegeben.

Es folgt eine Kurzzusammenfassung der einzelnen Kapitel, für eine genaue Erläuterung sei auf die englische Version der Kapitel verwiesen.

**1 Die Neutrinophysik** hat einige wichtige Grundbausteine für unser Verständnis des Universums geliefert. Die erste Erwähnung des Neutrinos war im Jahre 1930 durch Pauli. Bis dahin war unverständlich, warum beim  $\beta$ -Zerfall eine kontinuierliche Energieverteilung der entstehenden Elektronen, beim  $\alpha$ -Zerfall hingegen eine diskrete Energie der entstehenden Teilchen beobachtbar war. Um die Energieerhaltung zu wahren, postulierte Pauli ein weiteres, sehr leichtes Teilchen, das Neutrino.

Nicht nur ist die Masse des Neutrinos klein, aufgrund seiner fehlenden elektrischen und Farbladung tritt es hauptsächlich über die schwache Wechselwirkung in Erscheinung. Dementsprechend lang dauerte es bis zum ersten direkten Nachweis des Elektronenneutrinos im Jahre 1956. Später wurden auch die anderen beiden Neutrinogenerationen Myon- und Tauonneutrino nachgewiesen.

Da die abgestrahlte Leistung und die ablaufenden Kernfusionsprozesse der Sonne recht gut bekannt sind, kam bald die Idee auf, den Neutrinofluss der Sonne zu vermessen und mit den Erwartungen zu vergleichen. Das Homestake-Experiment konnte bei seiner Messung des Neutrinoflusses von 1970 bis 1994 jedoch nur ein Drittel der erwarteten Ereignisrate nachweisen. Eine Erklärung dafür sind die sogenannte Neutrinooszillationen. Hierbei sind die Eigenzustände der Masse und die der schwachen Wechselwirkung nicht identisch. Dies ist natürlich nur möglich, wenn es Eigenzustände unterschiedlicher Masse gibt. Durch diesen Effekt kann eine Umwandlung von Elektronenneutrinos in die beiden anderen Generationen stattfinden, was wiederum das Defizit des Homestake-Experimentes erklären könnte.

Um die Neutrinomasse zu bestimmen bieten sich neben der Vermessung der Oszillationen auch kosmologische Modelle, der  $\beta$ -Zerfall und der neutrinolose doppelte  $\beta$ -Zerfall an. Jede dieser Methoden hat ihre eigenen Vorteile, wobei für KATRIN der  $\beta$ -Zerfall von Tritium benutzt wird. Diese Methode hat den Vorteil, dass nur kinematische Größen bestimmt werden

müssen und als theoretisches Modell lediglich die gut nachgeprüfte Energie- und Impulserhaltung genutzt wird. Der Tritiumzerfall hat die zweitniedrigste Massendifferenz zwischen Mutter- und Tocherkern von allen Betastrahlern und eine niedrige Halbwertszeit von zwölf Jahren, was die Messung erleichtert, da somit viele Hochenergieelektronen zur Verfügung stehen.

Um die gewünschte Auflösung von 0,2 eV zu erreichen wird beim KATRIN-Experiment die Magnetisch-Adiabatische-Collimation kombiniert mit einem Elektrostatischen Filter (MAC-E-Filter) benutzt. Diese integrierenden Hochpassfilter wandeln die transversale kinetische Energie der Elektronen fast vollständig in longitudinale um, welche dann mittels eines Retardierungspotentials zur Elektronenfilterung benutzt wird. Um die systematischen Effekte klein, die erwartete Ereignisrate jedoch hoch, zu halten, wird eine fensterlose Quelle mit gasförmigen Tritium benutzt. Dabei sind hohe Anforderungen an die Druckstabilisierung zu stellen. Über mehrere Pumpsektionen werden das Tritium und dessen Zerfallsprodukte abgepumpt um nur die Zerfallselektronen zum MAC-E-Filter zu leiten. In einer dieser Pumpsektionen werden die Penningfallen, von denen diese Arbeit hauptsächlich handelt, positioniert werden.

Hier können sie nicht nur die Art der Moleküle und Ionen im Strahlrohr, sondern auch die Effizienz der Pumpsektion mit nur kurzen Unterbrechungen der Neutrinomassenmessung genau bestimmen. Ein Vorspektrometer mit geringerer Energieauflösung und ein Hauptspektrometer lassen im weiteren Verlauf nur Elektronen nahe der Endpunktsenergie passieren. Diese werden dann von einem Siliziumdetektor nachgewiesen.

**2 Penningfallen** dienen der Speicherung und Massenbestimmung von geladenen Teilchen. Sie sind im einfachsten Fall eine Überlagerung von einem elektrostatischem Quadrupolpotential und einem homogenen magnetischen Feld. Dabei sorgt das magnetische Feld dafür, dass geladene Teilchen radial eingesperrt werden. Die Überlagerung durch das elektrostatische Quadrupolfeld bewirkt, dass die Teilchen zusätzlich in axialer Richtung eingefangen werden. Die vorliegenden Fallen nutzen zur Erzeugung des elektrostatischen Feldes drei ringförmige Elektroden, somit handelt es sich um sogenannte dreipolige, zylindrische Penningfallen mit offenen Endkappen.

Aus der bekannten Zyklotronbewegung mit der Winkel Frequenz  $\omega_c = Bq/m$  eines Teilchens mit Masse  $m$  und Ladung  $q$  im Magnetfeld  $B$  kann, falls das Magnetfeld hinreichend genau bekannt ist, das Masse-zu-Ladungs-Verhältnis der gespeicherten Teilchen er-

rechnet werden. Generell kann ein gespeichertes Teilchen durch drei unabhängige Oszillationen beschrieben werden: Die modifizierte Zyklotronbewegung um die Magnetfeldlinien, welche bei verschwindendem elektrostatischem Potential in die freie Zyklotronbewegung übergeht, die Magnetronbewegung in der selben Ebene wie die Zyklotronbewegung, allerdings um das Fallenzentrum, und die axiale Oszillation zwischen den Endkappen.

Über die mittlere Elektrode, die Ringelektrode, können die gefangenen Teilchen in radialer Richtung angeregt werden. Diese Oszillation wird nach erfolgter Anregung über induzierte Ströme auf der Ringelektrode nachgewiesen. In idealen Penningfallen wäre die gemessene Frequenz unabhängig von der Ionenenergie, in realen Fallen verschiebt sich die Frequenz allerdings leicht. Dafür sind zum einen Abweichungen vom idealen Quadrupolfeld, aber auch Abweichungen vom homogenen Magnetfeld und relativistische Effekte hauptverantwortlich. Für weitere Frequenzverschiebungen sorgen eine ungenaue Ausrichtung der Felder zueinander, induzierte Spiegelladungen auf den Elektroden und Raumladungseffekte.

Zur Anregung und Detektion von gespeicherten Teilchen stehen für die vorhandenen Fallen ein radiales Dipol- oder Quadrupolfeld zur Verfügung. Um diese zu erzeugen und um Anregung und Detektion zu trennen, ist die Ringelektrode achtfach segmentiert.

**3 Der FT-ICR Versuchsaufbau** am MPIK in Heidelberg besteht aus einer Vakuumkammer und einem 4,7 T Magneten. In der Vakuumkammer befinden sich eine Glühemissionsquelle, einige optische Elemente, eine Penningfalle und ein Faradaybecher.

Die Ionenquelle erzeugt einfach ionisierte Lithiumionen in der natürlichen Isotopenverteilung und besitzt optische Elemente um den Ionenstrahl zu fokussieren und abzulenken. Die des Weiteren benutzte Linse ist eine dreiteilige Quadrupollinse, die sowohl zur Fokussierung als auch zur Ablenkung der Ionen benutzt werden kann. Da sie dafür Sorge trägt, dass die Ionen in den Magneten eingeschossen werden, besteht sie selbst aus nicht-magnetischen Materialien.

Die benutzte Penningfalle entspricht von den Maßen und Materialien den KATRIN-Fallen. Sie hat allerdings anstatt einer vierfach segmentierten eine achtfach segmentierte Ringelektrode. Hinter der Ionenfalle ist ein Faradaybecher positioniert, um bei geerdeten Fallenelektroden den Ionenstrom durch den Magneten und bei Messbetrieb die Anzahl der gespeicherten Ionen zu bestimmen.

Das induzierte Ionensignal auf der Ringelektrode, welches durch einen Vor- und Nachverstärker erhöht wird, wird mittels eines Transientenrekordes auf einem PC gespeichert. Dieses Zeitsignal wird mehrfach gemittelt und fouriertransformiert. Anhand der Fourieramplituden im errechneten Spektrum können Ionen identifiziert und anhand ihrer Fourierfrequenz Ionenmassen errechnet werden.

**4 Der Ionentransport** in die Falle ist wichtige Voraussetzung für eine Messung. Um die Bahn der Ionen zu verfolgen wurde der Aufbau am MPIK im Simulationsprogramm Simion nachgebildet.

Leider ist Simion von Haus aus nicht in der Lage Rotationsfelder darzustellen. Deswegen wurde das Magnetfeld durch fünf Leiterschleifen angenähert und mit dem Gesetz von Biot-Savart berechnet. Bei dieser Studie wurde herausgefunden, dass selbst kleine Verschiebungen und Verdrehungen der Symmetrieachse des Magnetfeldes zur Symmetrieachse des Aufbaus die Ionentransmission stark reduzieren.

Des Weiteren wurde simuliert, wie die Einfangeffizienz der Falle und der Aufenthaltsort der gespeicherten Teilchen von dem Potential der Endkappen abhängt. Die Voraussetzungen wurden ähnlich zu KATRIN gewählt: Die Teilchendichte über den Strahlrohrquerschnitt wurde als konstant angenommen. Hierbei ist zu bemerken, dass es im Allgemeinen leichter ist Teilchen nahe des Fallenrandes zu fangen, da an dieser Stelle das Potential steiler verläuft. Außerdem konnte beobachtet werden, dass ein höheres Potential die Ionenwolke in der Mitte der Falle axial stark komprimiert.

Um eventuelle Abweichungen von den erwarteten Frequenzen und Probleme beim Einfang zu erklären, wurde das Magnetfeld im homogenen Bereich vermessen. Dabei stellte sich heraus, dass die Korrekturspulen des Magneten nicht optimal eingestellt waren. Um dies zu beheben wurde der Magnet geschimmt. Mit mäßigen Erfolg, da zwei der drei Korrekturspulen sich als defekt herausstellten. Um den beobachteten Feldverlauf zu ergründen, wurden einige Computersimulationen mit COMSOL Multiphysics durchgeführt.

Zur Überprüfung der Magnetfeldmessungen wurde der magnetische Flaschenterm zusätzlich mit Lithiumionen vermessen.

**5 Frequenzverhältnismessungen** geben Auskunft über die Genauigkeit der benutzten Falle, sofern die benutzten Massen hinreichend gut bekannt sind. Für Lithiumionen ist dies der Fall, so dass über das Frequenzverhältnis von  ${}^6\text{Li}^+$  zu  ${}^7\text{Li}^+$  die Auflösung und die systematischen Fehler der Penningfalle bestimmt

werden können, da die Massen deutlich präziser bekannt sind, als sie der Aufbau dieser Arbeit bestimmen kann.  ${}^6\text{Li}^+$  hat zudem den Vorteil, dass es ein Isobar von molekularem Tritium ist, die Ergebnisse also übertragbar sind.

Hierfür werden die beiden Ionensorten mit einem Dipolfeld nahe ihrer reduzierten Zyklotronfrequenz angeregt und die reduzierte Zyklotronfrequenz als Funktion der Anregungsamplitude detektiert. Zusätzlich wird über die Quadrupoldetektion auch die Seitenbandfrequenz der reduzierten Zyklotronbewegung aufgezeichnet. Anhand des Zusammenhanges der Frequenzverschiebung mit steigender Anregungsamplitude können die Anharmonizitäten der Falle und des Magnetfeldes bestimmt werden.

Die Frequenzverschiebung durch relativistische Effekte liefert hierbei unmittelbar den Radius der Ionen in Abhängigkeit von der Anregungsspannung. Mit diesem Wert kann der elektrostatische Fehler der Falle berechnet werden. Hat man diese zwei Werte, kann der magnetische Flaschenterm bestimmt werden. Schlussendlich kann mit den Frequenzverschiebungen und Anharmonizitäten noch der Magnetronradius der gefangenen Ionen abgeschätzt werden.

Um das Massenverhältnis zu bestimmen existieren verschiedene Methoden, die miteinander verglichen werden. Die in kommerziellen Geräten am häufigsten benutzte Methode ist die Detektion der reduzierten Zyklotronfrequenz. Extrapoliert man diese zu 0 V Fallenspannung kann mit dem vorhandenen Massenspektrometer eine Genauigkeit  $\delta m/m$  von  $3 \cdot 10^{-7}$  erreicht werden. Ähnlich gut ist die Detektion über die Summenfrequenz, sie weist allerdings einen höheren statistischen Fehler auf, da für das weniger häufige  ${}^6\text{Li}^+$  das Signal-zu-Rausch-Verhältnis bei Quadrupoldetektion deutlich schlechter als bei Dipoldetektion ist.

Aus diesem Grund wurde eine Methode erdacht, die die Dipoldetektion von beiden Ionensorten und die Quadrupoldetektion von  ${}^7\text{Li}^+$  ausnutzt. Auf diese Art und Weise kann der statistische Fehler deutlich reduziert werden. Die Abweichung vom Literaturwert ist bei hohen Fallenspannungen deutlich geringer als in der reinen Dipoldetektion. Die Extrapolation zu 0 V Fallenspannung liefert jedoch einen ähnlichen Wert für die Genauigkeit.

Als letzte Methode wird die Konversion von Magnetronradius zu reduziertem Zyklotronradius mittels einer Quadrupolanregung detektiert. Diese Methode hat die geringste Genauigkeit, besitzt allerdings bei etwas besserem Vakuum noch erhebliches Potential. Interessanterweise zeigt diese Methode die kleinsten Abweichungen vom Literaturwert bei hohen Fallenspannungen.

In einem weiteren Messlauf wurde die Coulombwechselwirkung, also der Effekt der gespeicherten Ionenanzahl auf das Frequenzverhältnis, untersucht, wobei kein signifikanter Effekt erkennbar ist. Allerdings spielt die Reihenfolge, in der die Ionensorten angeregt werden, eine große Rolle. Nur wenn zuerst das häufigere  ${}^7\text{Li}^+$  angeregt wird, ist  ${}^6\text{Li}^+$  detektierbar. Grund hierfür ist vermutlich einen Abschirmungseffekt durch die größere Ladungswolke.

**6 Abschließende Tests der KATRIN-Fallen** ergaben eine einwandfreie Funktionsfähigkeit der Vorverstärker, auch bei 77 K. Zusätzlich wurde die spektrale Rauschdichte des kryogenen Vorverstärkers bei 77 K mit angeschlossenen Detektionselektroden vermessen. Dabei ergab sich ein Wert von weniger als  $2 \text{ nV Hz}^{-1/2}$ . Grund für die niedrige Rauschdichte ist die Verwendung von rauscharmen GaAs-Transistoren. Da über die Kapazitäten der Fallenelektroden relativ einfach externe Signale einkoppeln können, ist dieser Wert sehr gut und liegt innerhalb der Anforderungen. Unerwünschte Oszillationen waren nicht beobachtbar oder bei Frequenzen, die weit von den bei KATRIN erwarteten entfernt liegen.

Weiterhin wurden zwei Penningfallen für KATRIN zusammengebaut, verkabelt und mit Vorverstärkern und Filterboards versehen. Ein grundlegender Funktionstests wurde für beide Fallen durchgeführt und es konnte nachgewiesen werden, dass mit den Penningfallen Ionen gefangen, gespeichert, angeregt und detektiert werden können. Hierbei wurde nicht nur die reduzierte Zyklotronfrequenz, sondern auch die drei stärksten Seitenbänder detektiert.

Das FT-ICR-Detektionssystem für KATRIN wurde überprüft und die komplette Funktionsfähigkeit verifiziert. Stahl-Electronics wird ein Handbuch erstellen, in welchem die Inbetriebnahme des KATRIN FT-ICR MS Systems dargestellt wird. Der Auslieferung an KATRIN steht somit nichts mehr im Wege.

**7 Zusammenfassung und Ausblick** Neben einer kurzen Zusammenfassung der Ergebnisse wird ein Ausblick auf zukünftige Experimente mit der Kopie der KATRIN-Falle am MPIK gegeben. Da die Arbeit für das KATRIN-Projekt nun abgeschlossen ist, wird die Forschung in Zukunft auf das PIPERADE-Projekt, welches exotische Ionen speichern, reinigen und sammeln will, ausgerichtet sein. Hierbei werden einige wichtige Erkenntnisse für die KATRIN-Fallen gewonnen werden: Es werden im Rahmen von PIPERADE Cleaningprozeduren untersucht, welche wiederum die Isolation von weniger häufigen Ionensorten aus einer dichten

Ionenwolke erlauben. Außerdem wird ermittelt werden, welches Verhältnis von gefangenen zu gesuchten Ionen maximal aufgelöst werden kann. Mit einer Gasionierungsquelle können Ionenströme mit zwei Ionensorten in beliebigen Verhältnissen erzeugt werden. Über die so erzeugte Ionenwolke in der Penningfalle wird der Einfluss der Coulombwechselwirkung experimentell besser untersucht werden und parallel wird sie mit den Hochleistungsgrafikkarten des MPIK simuliert werden. Dafür dient das Simbuca-Programm [VG12], das in der Lage ist tausende Ionen mit Coulombwechselwirkung in einer Penningfalle ohne Näherung der Wechselwirkung zu simulieren. So kann hoffentlich die Lücke zwischen dem Experiment mit vielen Ionen und der theoretischen Beschreibung mit lediglich einem oder zwei Ionen geschlossen werden.



# Contents

<b>Introduction</b>	<b>1</b>
<b>1 Neutrinos</b>	<b>3</b>
1.1 Discovery	3
1.2 Neutrino oscillations	3
1.3 Determination of the neutrino mass	4
1.3.1 $\beta$ decay	4
1.3.2 Neutrinoless double $\beta$ decay	5
1.3.3 Time-of-flight method	6
1.3.4 Cosmological determination	6
1.4 The KATRIN experiment	6
1.4.1 The tritium $\beta$ spectrum	7
1.4.2 Principle of a MAC-E Filter	7
1.4.3 Experimental set-up	8
<b>2 Penning traps</b>	<b>13</b>
2.1 The ideal Penning trap	13
2.2 The real Penning trap	13
2.2.1 Field inhomogeneities and relativistic effects	13
2.2.2 Misalignment and distortion of fields	15
2.2.3 Coulomb interaction	16
2.2.4 Image charges	16
2.3 Excitation methods	16
2.3.1 Dipolar excitation	16
2.3.2 Quadrupolar excitation	17
2.3.3 Fourier limit and SWIFT	17
2.4 Detection via induced image charges	18
<b>3 FT-ICR set-up at the MPIK in Heidelberg</b>	<b>19</b>
3.1 Thermionic emission source	19
3.2 Ion optics	20
3.3 Superconducting magnet	20
3.4 Penning trap	21
3.5 Detectors	21
3.5.1 Image charge detection system	21
3.5.2 Faraday cup	22
3.6 Transient recorder	23
<b>4 Ion Transport</b>	<b>25</b>
4.1 Simulation of the trapping procedure with Simion	25
4.1.1 Simulation and calculation of the magnetic field	25
4.1.2 Transport simulation	26
4.1.3 Trapping efficiency	26
4.2 Magnet tests	29
4.2.1 NMR-probe measurements	29
4.2.2 Hall-probe measurements	30

4.2.3	Shimming of the magnet . . . . .	30
4.2.4	Simulation of the magnetic field . . . . .	33
4.2.5	$B_2$ measurement with ${}^7\text{Li}^+$ after shimming . . . . .	35
<b>5</b>	<b>Frequency ratio measurements</b>	<b>37</b>
5.1	Timing scheme and data acquisition . . . . .	37
5.2	Trap imperfections . . . . .	39
5.2.1	Extracting the modified cyclotron radius . . . . .	39
5.2.2	Electrostatic shifts . . . . .	40
5.2.3	Shifts from the magnetic bottle . . . . .	40
5.2.4	Extracting the magnetron radius . . . . .	40
5.2.5	Misalignment of fields . . . . .	42
5.2.6	Image charges . . . . .	42
5.3	Comparison of different mass ratio determination methods . . . . .	42
5.3.1	Conventional method . . . . .	42
5.3.2	Sideband measurement using the quadrupolar detection . . . . .	44
5.3.3	Sideband measurement using the dipolar and quadrupolar detection . . . . .	44
5.3.4	Quadrupolar conversion profiles . . . . .	45
5.3.5	Discussion and comparison of the four methods . . . . .	47
5.4	Coulomb interaction studies . . . . .	48
<b>6</b>	<b>Final test of the KATRIN Penning trap installation</b>	<b>51</b>
6.1	Cryogenic test of the KATRIN preamplifier . . . . .	51
6.2	Trapping of ions . . . . .	52
<b>7</b>	<b>Conclusion and outlook</b>	<b>55</b>
	<b>Bibliography</b>	<b>57</b>

# List of Figures

1.1	Impact of the neutrino mass on the endpoint of the tritium $\beta$ spectrum . . . . .	5
1.2	The selection rule for double $\beta^-$ decay . . . . .	6
1.3	Principle of a MAC-E-Filter . . . . .	7
1.4	Overview about the KATRIN set-up . . . . .	8
1.5	Rear system, source and transport system . . . . .	9
1.6	The DPS2-F . . . . .	9
1.7	KATRIN's spectrometers . . . . .	10
2.1	The different kind of Penning traps . . . . .	14
2.2	The ion motion in a Penning trap . . . . .	14
2.3	Dipolar excitation . . . . .	16
2.4	Quadrupolar excitation . . . . .	17
3.1	FT-ICR set-up at the MPIK . . . . .	19
3.2	Thermionic emission source . . . . .	19
3.3	Einzel lens . . . . .	20
3.4	The cylindrical Penning trap . . . . .	21
3.5	The preamplifier . . . . .	22
3.6	The postamplifier . . . . .	22
3.7	Faraday cup . . . . .	23
3.8	Network used for determining the capacity of the Faraday cup . . . . .	23
4.1	The magnetic field along the symmetry axis in the inhomogeneous region . . . . .	25
4.2	Simulation of the trapping efficiency for varying trapping voltage . . . . .	27
4.3	Probability density of trapped ions for different trapping potentials . . . . .	28
4.4	Position of the measured data points for Fig. 4.9 . . . . .	29
4.5	The magnetic field along the z-axis for different radii . . . . .	29
4.6	The magnetic field along a fixed radius . . . . .	30
4.7	Hall probe measurements . . . . .	30
4.8	Shimming the z correction coil . . . . .	31
4.9	The magnitude of the magnetic field in planes perpendicular to the symmetry axis . . . . .	32
4.10	Model for the simulation of shim coils . . . . .	33
4.11	Simulated magnetic field . . . . .	34
4.12	$B_2$ deduced from the frequency shift of lithium ions . . . . .	35
5.1	Timing scheme . . . . .	38
5.2	Exemplary FT-ICR spectrum . . . . .	38
5.3	FFT frequency measurements from an exemplary amplitude scan . . . . .	39
5.4	FFT amplitude measurements from an exemplary amplitude scan . . . . .	39
5.5	Effect of the number of trapped ions on the Fourier frequency . . . . .	43
5.6	The difference of $R$ from its literature value for the conventional mass determination method . . . . .	43
5.7	The difference of $R$ from its literature value for the for pure sideband detection . . . . .	44
5.8	The difference of $R$ from its literature value for the detection of $\nu_+$ and $\nu_+ + \nu_-$ . . . . .	45
5.9	Conversion profile of ${}^7\text{Li}^+$ . . . . .	45
5.10	Conversion profile of ${}^6\text{Li}^+$ . . . . .	46

---

5.11	The difference of $R$ from its literature value for the quadrupolar conversion profiles . . . . .	47
5.12	Amplitude of the modified cyclotron peak for varying ion numbers . . . . .	48
5.13	The effect of Coulomb interaction . . . . .	48
5.14	The effect of Coulomb screening on the modified cyclotron frequency of ${}^6\text{Li}^+$ . . . . .	49
6.1	Transfer function of the preamplifier . . . . .	51
6.2	Voltage noise density of the preamplifier . . . . .	52
6.3	Connection of the KATRIN devices . . . . .	53
6.4	A typical FT-ICR spectrum . . . . .	53

## List of Tables

5.1	Modified cyclotron radius for varying trapping voltages . . . . .	40
5.2	Magnetron frequency for different trapping voltages . . . . .	41
5.3	Sum frequency of ${}^6\text{Li}^+$ and ${}^7\text{Li}^+$ for different trapping voltages taken from quadrupolar conversion profiles . . . . .	46



# Introduction

I am not much impressed by the neutrino theory. In an ordinary way I might say that I do not believe in neutrinos. But I have to reflect that a physicist may be an artist, and you never know where you are with artists.

---

(Sir A. Eddington, [Edd39, p. 112])

Sir Arthur Stanley Eddington's quotation summarises the history of the elementary particle called neutrino in its own way. Back in 1938, when the astrophysicist Eddington pronounced these words neutrinos existed only as a theoretical tool to conserve energy and momentum in  $\beta$  decay. It should take another fifteen years until the first glimpse of a neutrino was observed in the Poltergeist experiment by Clyde L. Cowan and Frederick Reines [RC53]. But this did not mean that the artists had applied the varnish and everything was settled: Even today, the mass of the neutrino has only an upper bound, it is unclear whether the neutrino is its own antiparticle and the mixing of different neutrino flavours is a contemporary issue in science.

The Karlsruhe Tritium Neutrino (KATRIN) experiment will add another brushstroke to the canvas: It aims at determining the neutrino mass down to the sub electronvolt level. The current upper limit is  $2.05 \text{ eV}/c^2$  [ABB<sup>+</sup>11]. This corresponds to  $3.7 \times 10^{-36} \text{ kg}$ , so direct mass measurement with current methods are inconceivable because this precision can only be reached with charged particles. Thus, instead of detecting the neutrino mass directly, KATRIN uses the tritium  $\beta$  decay and determines the maximal electron energy in the  $\beta$  spectrum with a Magnetic Adiabatic Collimation combined with an Electrostatic Filter (MAC-E-Filter). The energy difference between the initial tritium and the final helium and electron must be carried away by the neutrino. A part of this energy is the rest mass of the neutrino.

However, to be able to reach a level of precision of  $0.2 \text{ eV}$  in  $18.6 \text{ keV}$ , the systematic effects have to be either small or well known. Therefore, it is important to reduce and monitor the tritium flow from the tritium source towards the electron detector. Since the tritium decays into  $^3\text{He}$  and forms clusters such as  $\text{T}_3^+$  and  $\text{T}_5^+$ , a broad band mass spectrometer ( $3 \text{ u}$  to more than  $15 \text{ u}$ ) with a comparatively high precision (better than

$1 \times 10^{-4}$ ) is needed.

Both requirements can easily be fulfilled by broad-band Fourier Transform Ion Cyclotron Resonance Mass Spectrometry (FT-ICR MS) – a standard tool in chemistry and biology for particle identification because a precision  $\delta m/m$  of  $10^{-6}$  is even reached by commercial systems. The Penning traps used by these systems to store the particles of interest and to perform the mass measurements can be designed in such a way that they will not reduce the beam radius of KATRIN while still being in the beam tube all the time. Thus, on-line monitoring of the tritium flow becomes possible. No other type of mass spectrometer can combine all these advantages. Hence, a set of two Penning traps will be installed at the entrance and exit of one of KATRIN's pumping sections.

In this work, a Penning trap similar to the KATRIN traps is characterised with a test set-up at the Max-Planck-Institut für Kernphysik (MPIK) in Heidelberg. First an overview about neutrino physics in general and the KATRIN experiment in particular is presented. Then a short introduction to Penning trap physics is given where it is explained how particles are stored and their mass is measured. For conditions similar to the KATRIN experiment, the trapping procedure is simulated in the following chapter. Additionally, the magnetic field of the MPIK magnet is reviewed by experiment and simulation because precise mass measurements in Penning traps require a homogeneous magnetic field. To show that the FT-ICR MS system is able to resolve tritium and helium isobars and to show that the efficiency of the pumping sections can be monitored, the accuracy of the traps is analysed depending on the employed detection method. A final test of all KATRIN equipment was set up and tested. Thus, the commissioning is presented together with a final conclusion and outlook.





# 1 Neutrinos

## 1.1 Discovery

In 1930, the neutrino was postulated by Pauli to recover energy-momentum conservation in the  $\beta$  decay [Pau30]. At that time, it had been assumed that the  $\beta$  decay is a two-body process where one neutron decays into one electron and one proton. However, this would have meant that, similar to the  $\alpha$  decay, the electron energy should be discrete. Measurements indicated that the electron energy is distributed continuously between 0 eV and a certain energy threshold. This wide range would only be possible, if energy-momentum conservation was violated or a third particle was being produced:

$$n \rightarrow p + e^- + \bar{\nu}_e. \quad (1.1)$$

In 1934, Fermi put forward his own theory of the  $\beta$  decay [Fer34], which heavily relied on the existence of a particle called neutrino<sup>1</sup>. Today, it is known that neutrinos are fermions with spin  $1/2$  which interact by the weak and the gravitational forces. They do not interact via the electromagnetic or strong force, so neutrinos carry neither an electric charge nor a colour. This is one of the reasons why the exact neutrino mass could not be determined yet – only an upper bound is known [OW08].

Due to the low effective cross section of neutrinos, it was impossible to directly observe neutrinos until the middle of the twentieth century. The first observation is attributed to Cowan and Reines in 1953 [RC53] and was awarded with the Nobel-prize in 1995. They used the high flux of antineutrinos coming from a nuclear reactor to observe an antineutrino induced  $\beta^+$  decay

$$p + \bar{\nu}_e \rightarrow n + e^+. \quad (1.2)$$

Water was used to supply the protons since the natural abundance of  $^1\text{H}$  is 99.99%. The high anti-neutrino background resulted from fission products. These usually undergo  $\beta^-$  decay because they are neutron rich. This is simply due to the fact that they are produced from heavy, neutron rich elements like uranium.

Later, it was discovered that there are three different kinds of neutrinos. They are the electron neutrino, the muon neutrino [DGG<sup>+</sup>62] and the tau neutrino

[KUA<sup>+</sup>01]. Their names derive from the corresponding neutrino flavour.

## 1.2 Neutrino oscillations

The first hint that neutrino oscillations occur came from the Homestake experiment in the late 1960s [DHH68]. The aim of this experiment was to determine the flux of solar neutrinos arising from the numerous fusion reactions happening in the sun. The expected number of events can be calculated from the solar power, the on-going reactions and their energy balance. But there was a tremendous deviation between theory and experiment [CDRD<sup>+</sup>98] known as the solar neutrino problem.

A possible explanation for this discovery is that electron neutrinos – the only kind of neutrinos produced by the sun – are converting into muon and tau neutrinos, which were undetectable for Homestake. Later Super-Kamiokande [FHI<sup>+</sup>98] tried to reproduce this effect with atmospheric neutrinos. Atmospheric neutrinos are created when cosmic rays hit the atmosphere and produce kaons and pions. These non stable particles decay partly into electron and muon neutrinos. Super-Kamiokande tried to measure these with a massive water tank and Čerenkov detectors. In this large volume of water, fast neutrinos will interact with the electrons and nuclei of the water molecules. This can create charged particles faster than the speed of light in water. Similar to an ultrasonic boom, a Čerenkov light cone is created spreading through the water. The direction of the cone contains information about the direction of the neutrino and its diffuseness is linked to the neutrino flavour. Muons (which are created by muon neutrinos) have a longer scattering length so they create a clear cone in contrast to electrons.

Super-Kamiokande found out that there are more muon neutrinos reaching the experiment from upwards than from the direction of the earth's core. Shielding effects can be ruled out as an explanation because of the low cross section of neutrinos. It rather indicates a conversion into other neutrino flavours depending on the time of flight.

---

1. The word neutron originally suggested by Pauli had already been used for the neutral particles in the nucleus.

Eventually, the solar neutrino problem was solved by the Sudbury Neutrino Observatory (SNO) [AAA<sup>+</sup>08], which is a set-up similar to Super-Kamiokande, except that normal water is replaced by heavy water (<sup>2</sup>H<sub>2</sub>O). This enables different reactions and thus the detection of tau neutrinos became possible. The total solar neutrino flux detected with SNO was well compatible with the Standard Solar Model (SSM).

There is the possibility of neutrino oscillations in a slightly extended Standard Model (SM) of particle physics. The most promising ansatz is to assign a different mass to each neutrino flavour and let the flavour eigenstates be a superposition of the mass eigenstates. This results in an oscillation as can be seen with the propagation operator of quantum mechanics for a free particle of initial momentum  $p_0$  and mass  $m$

$$U(t, p, p_0) = \exp\left(-i\frac{p^2}{2m}t\right) \delta(p - p_0). \quad (1.3)$$

Let us assume for simplicity that only two neutrino flavours exist. It is directly obvious that an electron neutrino which is consisting of two mass eigenstates oscillates between its two orthogonal flavour eigenstates as it propagates through space. This happens because the relative phase between the two mass states changes resulting in a mixing of flavour states.

For two flavours this results in a transformation probability  $P$  [Sch97]:

$$P = \sin^2(2\Theta_m) \sin^2\left(\frac{\Delta(m^2)L}{4E}\right), \quad (1.4)$$

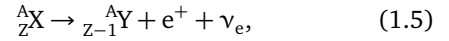
where  $E$  is the energy of the neutrino,  $\Theta_m$  is the so-called mixing angle between the mass and flavour eigenstates,  $\Delta(m^2)$  is the difference of the mass squared and  $L$  is the travelled distance of the neutrino. As can be deduced from Eq. (1.4), a mixing angle of  $\pi/4$  (plus multiples of  $\pi/2$ ) leads to complete oscillations between the two flavour states.

If all three flavours are taken into account, the Pontecorvo–Maki–Nakagawa–Sakata matrix has to be applied [BCG<sup>+</sup>96, Chap. 15]. It is the natural extension of the mixing formalism to three constituents similar to the Cabibbo–Kobayashi–Maskawa matrix in quark mixing.

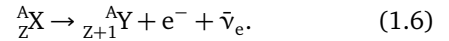
## 1.3 Determination of the neutrino mass

### 1.3.1 $\beta$ decay

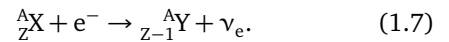
The  $\beta$  decay results from weak interaction whereby an up quark is converted into a down quark via an intermediate W boson. As there are no solitary quarks, this effect is commonly observed as a transformation of a proton with quark content (up, up, down) into a neutron with (up, down, down) or vice versa. One differentiates three types of  $\beta$  decay: The  $\beta^-$  decay,  $\beta^+$  decay and electron capture. In  $\beta^+$  decay, a proton is transformed into a neutron while a positron and an electron neutrino are emitted:



where X and Y are the respective mother and daughter nuclei. This process is energetically possible, if the total mass of the positron, electron neutrino and daughter nucleus is less than the mass of the mother nucleus. For  $\beta^-$  decay a similar process takes place: A neutron is transformed into a proton; an electron and an electron antineutrino are emitted



The electron capture is a partial reversal of the  $\beta^+$  decay. The nucleus captures one electron. This results in the conversion of a proton into a neutron while an electron neutrino is emitted. Energetically this process is allowed, if  $\beta^+$  decay is possible. The following equation holds



According to the Particle Data Group (PDG) [BAB<sup>+</sup>12], the current lowest upper bound for the neutrino mass (2.05 eV) comes from the Troitsk  $\beta$  decay experiments [ABB<sup>+</sup>11]. The underlying idea of these kind of experiment is to closely observe the endpoint of the electron spectrum released by the radioactive  $\beta$  decay in Eq. (1.5). The kinetic energy of the electron is limited by the difference between the rest mass of the mother nucleus and the sum of the rest masses of the daughter nucleus, the electron and the neutrino. This means that the endpoint energy is sensitive to the neutrino mass, if all other values are known with sufficient precision. The effect of a finite neutrino mass on the energy spectrum of electrons emitted in the  $\beta$  decay of tritium is simulated in Fig. 1.1.

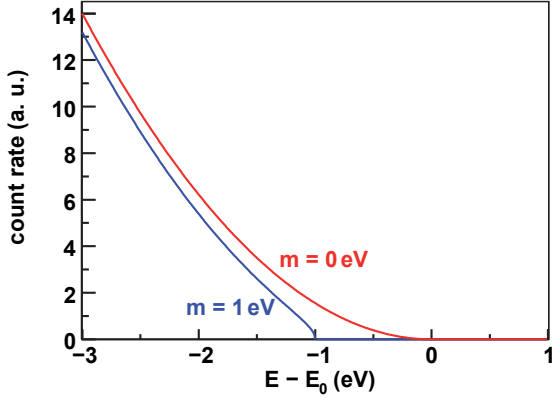


Fig. 1.1: Impact of the neutrino mass on the endpoint of the tritium  $\beta$  spectrum.  $m_\nu = 0\text{ eV}$  in red and  $1\text{ eV}$  in blue, respectively. A heavy neutrino reduces the maximum electron energy and changes the curvature of the count rate significantly. The relative change in electron count rate is approximately 1 in  $10^{-13}$ .  $E_0$  is the maximum kinetic energy of the electrons in the case of a vanishing neutrino mass. Adapted from [Hö09].

For the calculation of the count rate Fermi's Golden Rule can be used:

$$\frac{d^2 N}{dE dt} = \frac{2\pi}{\hbar} |M^2| \rho(E). \quad (1.8)$$

Where  $N$  is the number of counts,  $E$  the electron energy,  $M$  the nuclear transition matrix element and  $\rho$  the phase space available to the electron. The calculation is not too difficult and has been carried out for a hard sphere without inner degrees of freedom by Weinheimer [Wei03]. For convenience let  $\epsilon = E_0 - E$  where  $E_0$  is the maximum electron energy in case of a massless neutrino. Then the count rate per energy interval equals

$$\frac{d^2 N}{dE dt} = C(E) \epsilon \sqrt{\epsilon^2 - m_\nu^2 c^4} \Theta(\epsilon - m_\nu c^2). \quad (1.9)$$

$\Theta$  is the Heaviside function and  $C$  is a factor independent of the neutrino mass and given by

$$C = \frac{G_F^2 \cos^2 \Theta_m}{2\pi^2 \hbar^7} |M^2| F(E, Z+1) p (E + m_e c^2). \quad (1.10)$$

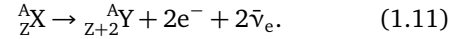
With the Fermi coupling constant  $G_F$ , the Fermi function  $F$  and the momentum of the electron  $p$ .

Clearly, a major disadvantage of this method is the low count rate that has to be detected. Usually, experiments of this kind are carried out with gaseous molecules or solids. So internal degrees of freedom and binding energies have to be corrected as well. Since there is a clear indication of neutrino oscillations, not only one mass will be measured. Rather a superposition of the three distinct mass states will lead to one combined count rate that is in turn a linear superposition of the individual count rates.

Despite these drawbacks the major advantage of the method is that for free particles it relies only on well-established energy-momentum conservation – no other theoretical input is needed.

### 1.3.2 Neutrinoless double $\beta$ decay

Since the double  $\beta$  decay is a second order process, it is only visible, if a nucleus cannot undergo single  $\beta$  decay. According to the Bethe-Weizsäcker mass formula, nuclei with even number of neutrons and protons have a lower binding energy than those with odd numbers. As shown in figure Fig. 1.2, this leads to the fact that for these nuclei single  $\beta$  decay is energetically forbidden and double  $\beta$  decay might be visible

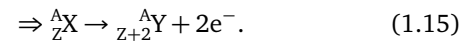
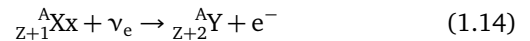
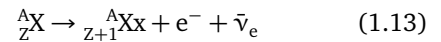


Simplified, the double  $\beta$  decay occurs when two nucleons decay simultaneously. Of course, this is only possible, if energy is released during the process. In other words

$$m({}^A_Z X) > m({}^A_{Z+2} Y). \quad (1.12)$$

Usually, the lifetime of a double  $\beta$  decay emitter is in the order of  $10^{20}$  a [KK10, p. 200].

The neutrinoless double  $\beta$  decay ( $0\nu\beta\beta$  decay) is a special case. It requires a virtual neutrino and can be written as a two step reaction involving one neutrino:



As one can see this is only possible, if the neutrino is its own anti-particle, a so called Majorana particle, and at least one mass eigenstate has a non vanishing rest mass because of the neutrino's helicity. The signature of a  $0\nu\beta\beta$  decay is a sharp peak in the energy spectrum at

$$E/c^2 = m({}^A_{Z+2} Y) - m({}^A_Z X). \quad (1.16)$$

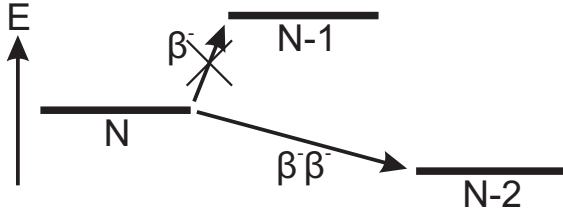


Fig. 1.2: A graphic representation of the selection rule for double  $\beta^-$  decay. All shown elements have the same number of nucleons, but the proton-to-neutron ratio changes. The number of neutrons is written below the energy of the respective nucleus ( $N$  being the number of neutrons of the mother nucleus). Double  $\beta^-$  decay is only observable, if the nucleus with one neutron less than the mother nucleus has a higher rest mass and thus the decay to this nucleus is energetically forbidden. Of course, the daughter nucleus (which has two neutrons less) must have a lower rest mass than its mother.

The Heidelberg Moscow Experiment used this technique with  $^{76}\text{Ge}$  and derived a half-life for the process and a neutrino mass of [KKDK<sup>+</sup>04]

$$T_{1/2} = 0.8 - 18.3 \times 10^{25} \text{ a} \quad (1.17)$$

$$\langle m \rangle = 0.05 - 0.84 \text{ eV}. \quad (1.18)$$

Where  $\langle m \rangle$  is the effective Majorana neutrino mass that can be calculated from the half-life, if one knows the corresponding nuclear matrix element. An overview about current progress in the calculations of nuclear matrix elements is given in [Rod12].

These results were heavily discussed in literature [ABB<sup>+</sup>02] and future experiments will have to bring light into the darkness. Generally speaking,  $0\nu\beta\beta$  decay experiments can yield interesting results, if the neutrino is a Majorana particle. However, if that is not the case, the neutrino mass is unavailable to this kind of experiments. Another drawback is the reliance on model dependent nuclear matrix elements.

### 1.3.3 Time-of-flight method

Supernovas send out a neutrino burst which is typically shorter than 10s. If electron neutrinos are a superposition of different mass states, they evolve with a different speed. Hence, after a very long time of flight, unmixing of the different mass eigenstates occurs. Instead of one, two peaks should be visible in modern

neutrino detectors. Due to the different relative phase of the mass states, there would also be a conversion between the different neutrino flavours.

The long baseline of a couple of thousand light years and a spread of the peak of 10s for a common supernova roughly correspond to an upper limit of approximately 3 eV for the neutrino mass [Sch01]. Theoretically, the time difference between the gamma ray burst and the neutrino burst could be used to investigate the speed of the neutrino, but this is again heavily model dependent and could only be used to disprove neutrinos faster than the speed of light [Sto88].

### 1.3.4 Cosmological determination

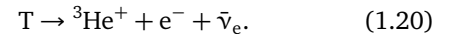
In our universe the ratio of neutrinos to baryons is approximately 1 billion to one. Naturally, this makes neutrinos a very important part of hot dark matter. As neutrinos are very light, they can stream out of regions with higher densities and thus limit the growth of density fluctuations. This means that if one tries to model the large scale structure in our universe, neutrinos and especially their mass will play a big role.

However, there are several disadvantages of the cosmological mass determination. One is the strong model dependence. Input parameters such as the ratio of hot dark matter to cold dark matter can only be estimated and it usually happens that many parameters are degenerate. Nevertheless there are many cosmological estimates on the neutrino mass, usually in the order of [KAT05, p. 19]

$$\sum_{e,\mu,\tau} m_\nu \lesssim 2 \text{ eV}. \quad (1.19)$$

## 1.4 The KATRIN experiment

The KARlsruhe TRItium Neutrino (KATRIN) Experiment aims at determining the neutrino mass [Wei02]. KATRIN exploits the tritium  $\beta$  decay (see Section 1.3.1). The underlying idea is to determine the electron energy from the following reaction<sup>2</sup>:



Of course, this is further complicated by the fact that, like hydrogen, tritium exists in molecular form only. According to the KATRIN design, neutrino masses down to 0.2 eV may be detected [KAT05]. This value is approximately an order of magnitude lower than

2. Typically, tritium is denoted with the letter T instead of  ${}^3\text{H}$ .

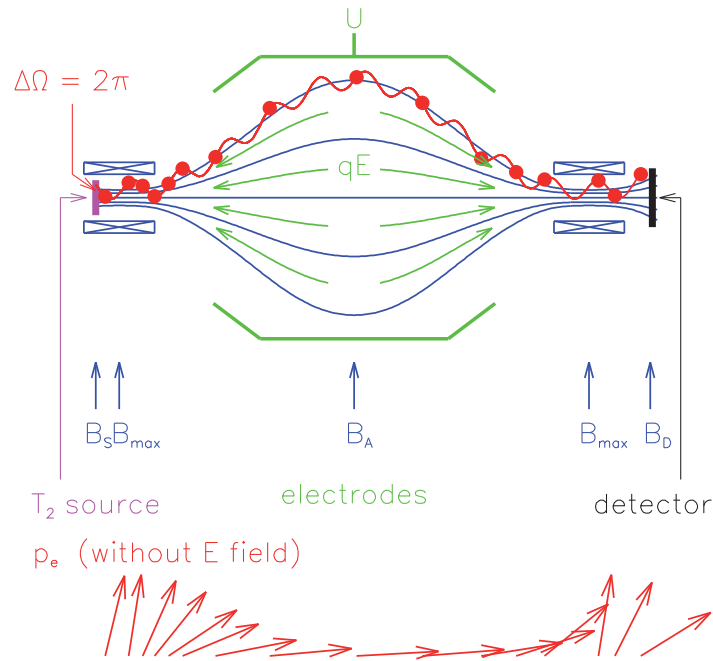


Fig. 1.3: Principle of a MAC-E-Filter. The upper part shows the general set-up with two superconducting magnets and one set of electrodes to block charged particles in between. A hypothetical particle trace without electrostatic fields is displayed in red. Below is the momentum vector  $p_e$  of the particle as it changes due to the adiabatic transport along the magnetic flux lines. The electrodes which are connected to a voltage  $U$  and the resulting electric field are shown in green. The superconducting magnets and their magnetic flux density is shown in blue. The  $B$  field at the source  $B_S$ , in the analysing plane  $B_A$ , at the detector  $B_D$  and the maximum field  $B_{max}$  are marked as well. Adapted from [KAT05].

the current limit from the Troitsk [ABB<sup>+</sup>11] and Mainz [KBB<sup>+</sup>05] experiment.

### 1.4.1 The tritium $\beta$ spectrum

The tritium decay was chosen because it has several experimental advantages concerning the determination of the neutrino mass. With  $E_0 = 18.6$  keV, tritium has the second lowest endpoint in the  $\beta$  spectrum of all known beta emitters. Thus, it becomes feasible to record only the electrons close to the endpoint. These are most important for the determination of the neutrino mass as the exact position of the endpoint strongly depends on this mass. A high intensity source of tritium occupies a rather small volume because the half-life of tritium is only  $t_{1/2} = 12.3$  a. The electron shells of mother and daughter nuclei are easy to calculate quantum mechanically and are well studied. So energy corrections from internal excitations are not too difficult to take into account. The scattering probability of  $\beta$  electrons at tritium atoms is small because of the low number of nuclides per nucleus. Last but not least, the  $\beta$  decay of

tritium is a super allowed transition. Thus, there are no corrections from nuclear transition matrix elements.

### 1.4.2 Principle of a MAC-E Filter

The design of the Magnetic Adiabatic Collimation combined with an Electrostatic Filter (MAC-E-Filter) is the main reason for the increased sensitivity of the Troitsk and KATRIN experiments.

A MAC-E-Filter consists of at least two superconducting coils, one at the entrance and one at the exit of the filter as shown in Fig. 1.3. Even fast particles are forced on cyclotron radii because of the high magnetic field in the source. Hence, nearly all ions with a positive initial axial momentum are guided by the magnetic flux lines towards the filter's central plane. This way particles emitted at a solid angle of approximately  $2\pi$  can be guided towards the detector. During their flight, the magnitude of the  $B$  field drops slowly. This way the cyclotron energy  $E_{p+}$  is converted into axial energy. This can be seen by the direction of the momentum vector in Fig. 1.3. Due to the adiabatic transport, the

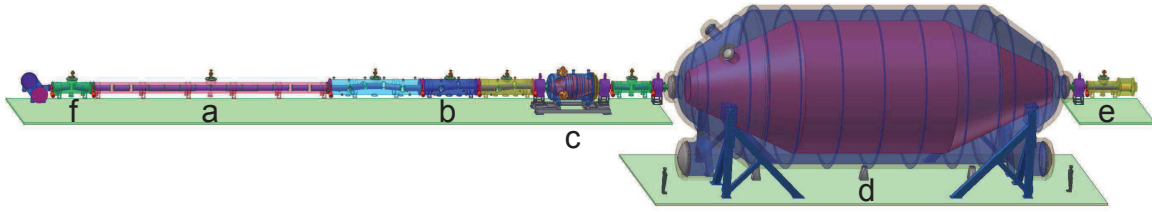


Fig. 1.4: Overview about the KATRIN set-up: Electrons are created by  $\beta$  decay in the windowless gaseous tritium source (a) and then transported and separated from remaining gas by the transport section (b). Most of the electrons are rejected in the pre-spectrometer (c) – only those with an energy close to the endpoint are energy selected in the main spectrometer (d). The remaining particles are accelerated again and guided to the detector (e). At the other side of the tritium source, the so-called rear system (f) is installed. All in all the set-up is 70 m long. Humans are added to the figure to illustrate the size of the set-up. Adapted from [KAT05].

magnetic moment  $\mu$  of the particle stays constant:

$$\mu = \frac{E_{\rho+}}{B} = \text{const.} \quad (1.21)$$

A superimposed electrostatic field is then used to block charged particles below a certain threshold energy. All in all, the MAC-E-Filter acts as a high pass, integrating filter. Its energy resolution  $\Delta E/E$  is limited by the ratio of the maximum magnetic flux  $B_{\max}$  to the magnetic flux  $B_A$  at the electrostatic blocking potential:

$$\frac{\Delta E}{E} = \frac{B_A}{B_{\max}}. \quad (1.22)$$

In practice, the magnetic field is not the highest directly at the source, but between the source and the electrodes. This ensures that particles with a very low initial axial velocity get reflected by the magnetic mirror effect. Particles that have a very high scattering probability inside the source are thus removed. For the KATRIN set-up  $B_A$  is  $3 \times 10^{-4}$  T and  $B_{\max}$  is approximately 6 T so the energy resolution is  $5 \times 10^{-5}$ . At an endpoint energy of 18.6 keV this value corresponds to 0.9 eV [KAT05].

### 1.4.3 Experimental set-up

The KATRIN experiment resides in Karlsruhe at the Campus Nord. One of the advantages of this location is that parts of the infrastructure of the Tritium Laboratory Karlsruhe (TLK) can be used for the KATRIN set-up. The TLK is the only non-military research laboratory with a closed tritium loop and it already possessed allowances for handling the tritium quantities needed for KATRIN<sup>3</sup>.

The experiment can be divided into five parts (see Fig. 1.4) which will be explained in more detail in the following sections:

- Rear system
- Windowless Gaseous Tritium Source (WGTS)
- Electron transport section
- Two electrostatic retarding filters
- Semi-conductor based detector

#### 1.4.3.1 Rear system

Behind the WGTS there is the so-called rear system as shown in Fig. 1.4. Its first part is a differential pumping system which is rather similar to the one at the front side of the source (see: Section 1.4.3.3) to keep the tritium flow symmetric. Behind the pumping section the Calibration and Monitoring System (CMS) is installed.

The CMS is mainly used to control and monitor the tritium source. For this reason there is an electron detector which monitors the  $\beta$  electrons and thus the activity of the tritium. A rear plate of a well-defined potential is also part of the CMS. Due to the high conductivity in axial direction, the electrostatic potential of the source is mainly dominated by the potential of the rear plate. This is necessary because small fluctuations of the potential energy of the tritium molecules will add as a further uncertainty. It has been seen that even

<sup>3</sup>. The daily throughput of the source is 10 g of tritium and the TLK has a licence for 40 g [KAT02, p. 20].



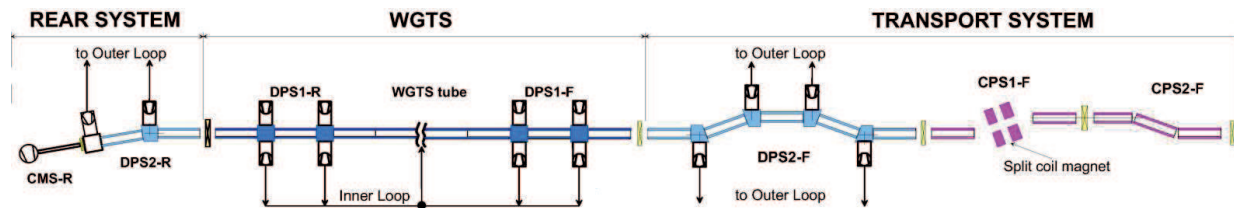


Fig. 1.5: Rear system, source and transport system. Tritium is inserted into the middle of the source, pumped at the far ends and recycled as indicated by the inner loop. Next to the source there are two more differential pumping sections (DPS2-F and DPS2-R) and even further downstream the cryogenic pumping sections (CPS). To the right side of the figure the pre-spectrometer is situated. On the far left, the control and monitor section (CMS) can be seen. The letters R and F denote the rear and front side of the source, respectively. Taken from [KAT05].

adsorption of tritium onto a surface may change the work function so much that it will make an impact on the KATRIN sensitivity. For test purposes the CMS also includes an electron gun and other calibration sources to determine the functionality of the whole KATRIN set-up.

#### 1.4.3.2 WGTS

The Windowless Gaseous Tritium Source (WGTS) is the birth place of electrons via  $\beta$  decay of tritium. It mainly consists of a gaseous column of molecular tritium and is a roughly 10 m long tube with an inner diameter of 90 mm. The tritium is kept at a temperature of 30 K and a pressure of  $10^{-3}$  mbar.

$T_2$  is injected in the middle of the source at a rate of approximately  $2 \text{ mbar l s}^{-1}$ . The amount of electrons per second is directly proportional to the number of tritium molecules being present in the source ( $N(T_2)$ ) which is in turn linked to the column density  $\rho d$ , the cross-section area  $A$  and the tritium purity  $\gamma$

$$N(T_2) = \rho d \times A \times \gamma. \quad (1.23)$$

The injected tritium is mainly pumped into the inner loop and recycled afterwards [Stu10].

The tritium leak rate, temperature, purity and the pump rates have to be stabilized in order to maintain a steady column density in the source. This is done to keep systematic effects from electron scattering in the source constant and low. The source is monitored by the help of the rear system (see Section 1.4.3.1). A magnetic field is superimposed on the whole region. This ensures the guidance of the electrons towards the spectrometer and rear section. An overview of the source and its neighbouring segments is displayed in Fig. 1.5.

#### 1.4.3.3 DPS2-F and CPS

The aim of the Differential Pumping Section at the front side of the source (DPS2-F) is to reduce the pressure by five orders of magnitude. Together with the CPS the tritium flow is reduced to only  $10^{-14} \text{ mbar l s}^{-1}$ . To achieve this, four pumping chambers with turbo molecular pumps are installed between five beam tubes with a relative angle of  $20^\circ$  to each other (see Fig. 1.6). The idea behind these angles is that only charged particles will be guided by the magnetic field lines around the corner, whereas neutral  $T_2$  molecules will impinge on the walls. This effect is further enhanced by cooling the whole DPS and by electrical dipoles. These make use of the  $\vec{E} \times \vec{B}$ -drift to deflect positive ions into the wall.

To monitor the effectiveness of the DPS and possible contaminants, ion concentrations will be detected with two Penning traps – one at the entrance and one at the

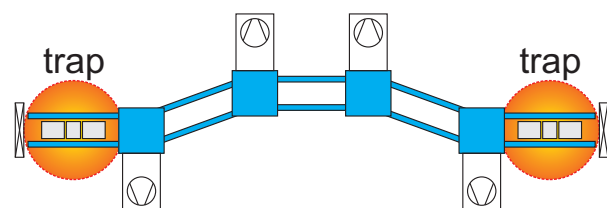


Fig. 1.6: The DPS2-F consists of five tubes set at a relative angle of  $20^\circ$  and four pumping chambers (blue squares) in between. Each pumping chamber has an attached turbo pump. All beam tubes are at cryogenic temperatures (blue) to reduce the pressure even further. In addition, two three-segmented Penning traps (grey) will be placed at the entrance and the exit of the DPS2-F to monitor ion concentrations.

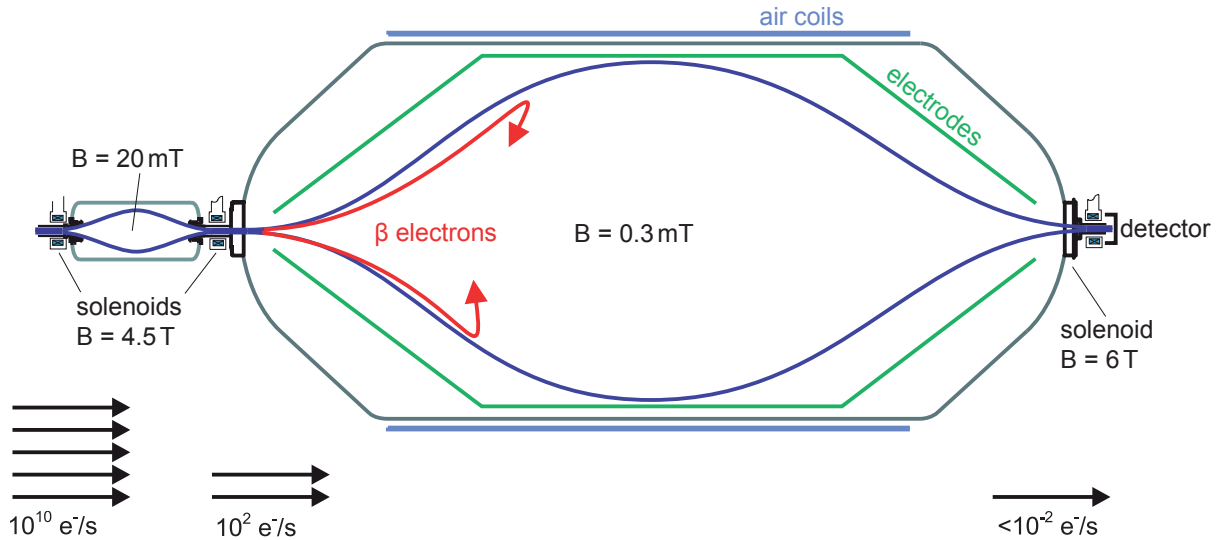


Fig. 1.7: KATRIN's spectrometers consisting of a pre-spectrometer (left) and the main spectrometer (right) with a transport solenoid in between. Three solenoids define the magnetic field (dark blue) with the aid of the air coils (light blue) to get a very well-defined magnetic field in the main spectrometer. The path of an electron slightly below the threshold energy is shown in red. The wire electrodes in the main spectrometer are displayed in green. The reduction of the electron flux by these two filters is shown below. Adapted from [Stu10].

exit of the DPS2-F [UDRL<sup>+</sup>09].

The Cryogenic Pumping Sections (CPS) are passive pumping sections that work by adsorption of tritium molecules. Their surface is cooled to 3 K – well below the boiling point of molecular tritium – to freeze out all possible contaminants that might hit the walls [Eic08]. Argon frost is used to further enlarge the adsorption surface. This way, a removal factor for molecular tritium of  $10^{-7}$  can be reached enabling the eXtreme High Vacuum (XHV) in the main spectrometer.

#### 1.4.3.4 Pre-spectrometer

The pre-spectrometer is one of the two MAC-E-Filters (see Section 1.4.2) installed in the KATRIN set-up. A high voltage (approximately 100 V below the endpoint) is applied directly to the hull of the pre-spectrometer to form a homogeneous electric field. Attached to its walls is a set of wire electrodes at a slightly lower potential. This blocks electrons emitted from the wall and is a way to limit unwanted Penning traps by clever wire layout. Unwanted Penning traps occur because of the electric and magnetic fields of the MAC-E-Filters. They are problematic because the stored particles might create electrons which will affect the recorded spectrum. The wire electrodes help to assure adiabatic transport of the  $\beta$  electrons too.

The pre-spectrometer acts as a pre-filter for the electron energy. It is 3.4 m in length and is operated at a pressure of  $\lesssim 10^{-11}$  mbar. The applied voltage is approximately  $-18.3$  kV. Directly behind the pre-spectrometer is a transport solenoid leading the remaining electrons into the main spectrometer as it is shown in Fig. 1.7. The energy resolution of the pre-spectrometer is approximately 70 eV.

#### 1.4.3.5 Main spectrometer

The main spectrometer is very similar to the pre-spectrometer (see Section 1.4.3.4), but ten times larger as illustrated in Fig. 1.7. It is the largest eXtreme High Vacuum ( $\lesssim 10^{-11}$  mbar) on earth. Its inner diameter is 9.8 m and it is 23 m in length. Fixed on the inner side of the walls is a thin wire electrode system at a slightly lower potential than the walls. This blocks electrons which are emitted from the wall and creates a well-defined electrostatic field.

Two superconducting magnets at the ends of the main spectrometer define the magnetic field inside. The field is further enhanced by two air coil systems around the vessel to correct the  $B$  field in the analysing plane and the fluctuations of earth's magnetic field. Altogether, the flux tube reaches a diameter of



9 m. The energy resolution of the main spectrometer is approximately 0.9 eV (see Section 1.4.2).

To maintain the XHV, two pump ports with several turbo molecular and ion getter pumps are set up. The whole spectrometer can be baked out at 350 °C to get rid of possible contaminants.

#### 1.4.3.6 Electron detector

The requirements for the electron detector are a high efficiency (90 %) for electrons with an energy of up to 50 keV and an energy resolution of 1 keV for background discrimination. Count rates of up to 100 kHz are expected [KAT05].

It is possible to fulfil all these prerequisites by using a multi pixel silicon semiconductor with a very thin entrance window and a diameter of 9 cm. A magnetic field of 3 T is used to compress the ion beam since a smaller detector means a better signal-to-noise ratio. Furthermore, a shielding is installed around the device to limit background radiation. The detector consists of 148 pixels that are arranged in concentric rings and cover a total area of 41.1 mm<sup>2</sup> [Ren11].



## 2 Penning traps

### 2.1 The ideal Penning trap

A Penning trap is a device to store charged particles using a superposition of a homogeneous magnetic field and a quadrupolar electrostatic field. Charged particles of mass  $m$  and charge  $q$  are radially confined in a magnetic field  $B$  because the Lorentz force acts upon them. This leads to a circular motion with the angular cyclotron frequency  $\omega_c$

$$\omega_c = \frac{q}{m}B. \quad (2.1)$$

To achieve a three dimensional confinement an electrostatic quadrupole potential  $V$  is applied:

$$V(\rho, z) = \frac{V_{\text{EC}}}{2d^2} \left( z^2 - \frac{\rho^2}{2} \right), \quad (2.2)$$

where  $d$  is a geometry parameter,  $V_{\text{EC}}$  is the applied voltage,  $z$  points in the direction of the magnetic flux lines and  $\rho$  is the radius in a cylindrical coordinate system defined by  $z$ . As can be inferred from Eq. (2.2), equipotential surfaces are hyperboloids of revolution. This is exploited in hyperbolic Penning traps. Their electrodes are approximate hyperboloids as depicted in Fig. 2.1a. To define a quadrupole potential, at least three electrodes are needed: a single hyperboloid of one sheet, called ring electrode, and one hyperboloid of two sheets, called endcap. The trapping voltage  $V_{\text{EC}}$  is applied between the ring electrode and the endcaps. For hyperbolic traps with an inner diameter  $2\rho_0$  and a distance of the two endcaps  $2z_0$ , the geometry parameter  $d$  is given by

$$d^2 = \frac{1}{2} \left( z_0^2 + \frac{\rho_0^2}{2} \right). \quad (2.3)$$

As illustrated in Fig. 2.1b, there are other types of Penning traps for example the cylindrical trap with open endcaps. This kind of trap is basically a tube cut in three parts: two endcaps and one ring electrode. By choosing the lengths of the electrodes carefully, a quadrupolar potential is created at the centre of the trap. To decrease possible deviations from the ideal quadrupolar electric field, correction electrodes are usually added.

Solving the equation of motion of a trapped particle yields three distinct eigenmotions with their respective eigenfrequencies:

$$\omega_z = \sqrt{\frac{qV_{\text{EC}}}{md^2}} \quad (2.4)$$

$$\omega_+ = \frac{1}{2}\omega_c + \frac{1}{2}\sqrt{\omega_c^2 - 2\omega_z} \quad (2.5)$$

$$\omega_- = \frac{1}{2}\omega_c - \frac{1}{2}\sqrt{\omega_c^2 - 2\omega_z}. \quad (2.6)$$

$\omega_z$  is an axial oscillation while  $\omega_+$  (modified cyclotron frequency) and  $\omega_-$  (magnetron frequency) are radial oscillations. The corresponding ion motion is shown in Fig. 2.2. Each eigenmotion has a corresponding energy which consists of a kinetic and a potential part and depends on the magnetron radius  $\rho_-$ , modified cyclotron radius  $\rho_+$  and the axial oscillation amplitude  $\rho_z$  [Bla06]

$$E_z = \frac{1}{2}m\rho_z^2\omega_z^2 \quad (2.7)$$

$$E_+ = \frac{1}{2}m\rho_+^2\omega_+(\omega_+ - \omega_-) \quad (2.8)$$

$$E_- = -\frac{1}{2}m\rho_-^2\omega_-(\omega_+ - \omega_-). \quad (2.9)$$

### 2.2 The real Penning trap

In an ideal Penning trap the eigenfrequencies are independent of the amplitude of the ion motion. However, in a real Penning trap these frequencies depend on the amplitude. Mainly, this effect arises from imperfections of the electrostatic potential and the magnetic field and from relativistic effects. All of which will be discussed in the following sections. Ions can only be detected, if they have a certain amplitude. So these imperfections cause a serious limitation of the mass resolving power.

#### 2.2.1 Field inhomogeneities and relativistic effects

##### 2.2.1.1 Magnetic field inhomogeneities

The strength of a superconducting magnet is not constant but it decreases over time. This is due to the so

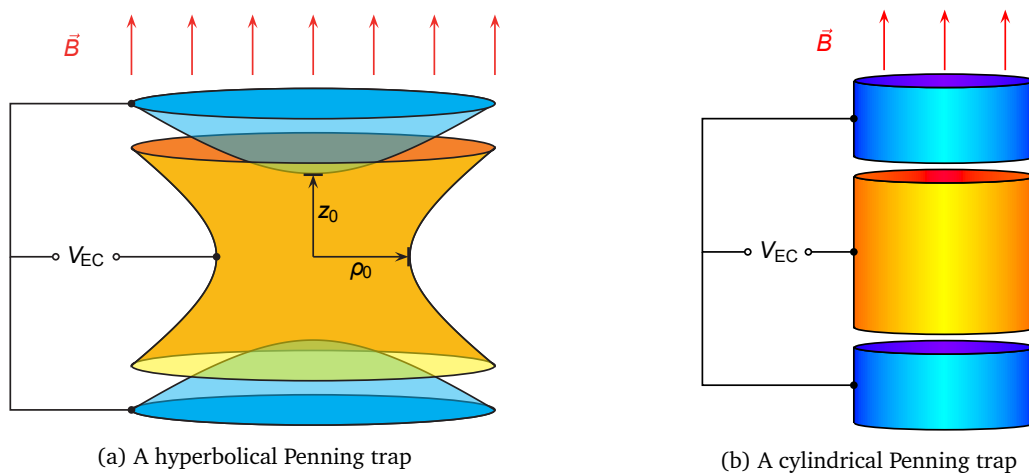


Fig. 2.1: Different kind of Penning traps: A hyperbolic trap (a) consisting of two hyperboloids of revolution (amber: ring electrode, blue: endcaps) and a cylindrical trap (b) where the endcaps and the ring electrode are marked with the same colours as in (a). The voltage  $V_{EC}$  is applied between the ring electrode and the endcaps.  $z_0$  and  $\rho_0$  are the shortest distance of the hyperboloids of revolution to the trap centre. The superimposed magnetic flux density  $B$  is drawn in red. Courtesy of Jochen Ketter.

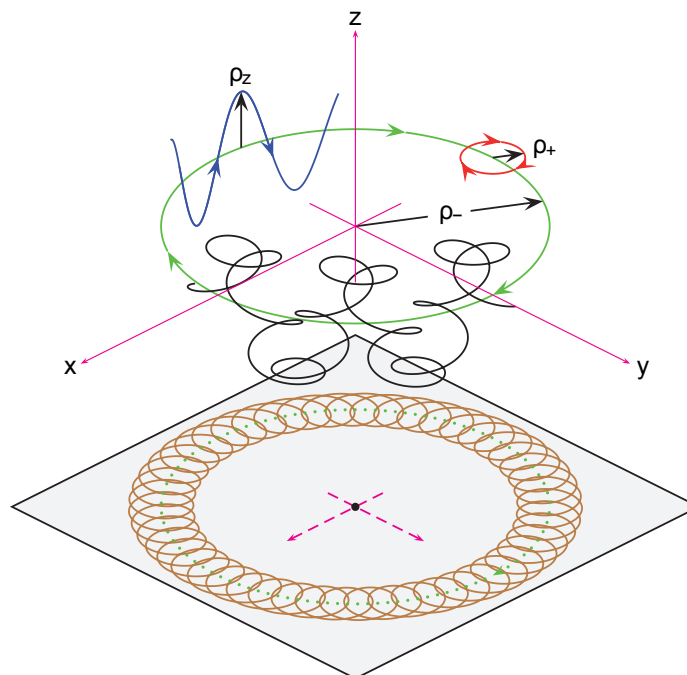


Fig. 2.2: The ion motion in a Penning trap can be reduced to its three eigenmotions: One axial oscillation (blue) with  $\rho_z$  and two radial (golden projection) with  $\rho_-$  (green) and  $\rho_+$  (red). The magnetron motion is a slow revolution with  $\rho_-$  around the trap centre and the cyclotron motion is a fast movement with  $\rho_+$  around the magnetron. The superposition of all oscillations is shown in black. Courtesy of Jochen Ketter.

called flux creep phenomenon [And62]. Furthermore, the coils do not create a perfect homogeneous field. This effect is enhanced by the fact that nearly every material has a non zero magnetic susceptibility. Generally, second order deviations from the homogeneous field can be described by

$$\Delta\vec{B} = B_2 \left( \left( z^2 - \frac{1}{2}\rho^2 \right) \frac{\vec{z}}{z} - z\vec{\rho} \right). \quad (2.10)$$

According to [BG86] this results in an energy dependent frequency shift

$$\begin{pmatrix} \frac{\Delta\omega_+}{\omega_+} \\ \frac{\Delta\omega_z}{\omega_z} \\ \frac{\Delta\omega_-}{\omega_-} \end{pmatrix} = M_B \begin{pmatrix} E_+ \\ E_z \\ E_- \end{pmatrix} \quad (2.11)$$

$$M_B = \frac{1}{eV_{EC}} \frac{B_2 d^2}{|B|} \begin{pmatrix} -\left(\frac{\omega_z}{\omega_+}\right)^2 & 1 & 2 \\ 1 & 0 & -1 \\ 2 & -1 & -2 \end{pmatrix}. \quad (2.12)$$

### 2.2.1.2 Electric field imperfections

Electric field imperfections for hyperbolic traps are induced by the fact that the electrodes have a finite size or some manufacturing tolerances. For cylindrical traps there is always a non vanishing deviation from the quadrupolar potential. In the lowest order, deviations for both traps can be described by

$$\Delta V = V_{EC} \frac{C_4}{2d^4} \left( z^4 - 3z^2\rho^2 + \frac{3}{8}\rho^4 \right). \quad (2.13)$$

Usually, correction electrodes which minimize the coefficient  $C_4$  are added to the set-up. For these cases the next higher order will play a big role. As well as for the magnetic imperfections, a matrix can be found that links the particle's energy to the frequency shifts [BG86]. The overall shift is calculated in Section 2.2.1.4.

### 2.2.1.3 Relativistic effects

Due to the fast ion motion, the apparent mass of the ions seems to increase. Formally, this can be handled by substituting the rest mass by the relativistic mass

$$m \rightarrow \frac{1}{\sqrt{1 - \frac{v^2}{c^2}}} m. \quad (2.14)$$

It is obvious from Eqs. (2.1) and (2.4) that this results in a decrease of the cyclotron and axial frequency for

increasing ion energy. As with other frequency shifts, Ref. [BG86] lists a matrix connecting the ion energy to its frequency shifts.

### 2.2.1.4 Frequency shifts on $\omega_+$ and $(\omega_+ + \omega_-)$

With the help of the energy frequency shift correlation matrices and the equations for the energy (Eqs. (2.7) to (2.9)), the frequency shifts depending on the ion's axial amplitude  $\rho_z$ , magnetron  $\rho_-$  and modified cyclotron radius  $\rho_+$  can be calculated. The first order corrections for the modified cyclotron frequency  $\omega_+$  and the sum frequency  $\omega_{\bar{c}} = \omega_+ + \omega_-$  are given by [BG86]:

$$\begin{aligned} \Delta\omega_+ = & \left( -\frac{1}{2} \frac{B_2}{|B|} \omega_+ + \frac{3}{2} \frac{C_4}{d^2} \omega_- - \frac{1}{2} \frac{\omega_+^3}{c^2} \right) \rho_+^2 + \\ & \left( \frac{1}{2} \frac{B_2}{|B|} \omega_+ - 3 \frac{C_4}{d^2} \omega_- - \frac{1}{2} \frac{\omega_+^2 \omega_-}{c^2} \right) \rho_z^2 + \\ & \left( -\frac{1}{2} \frac{B_2}{|B|} \omega_+ + 3 \frac{C_4}{d^2} \omega_- - \frac{\omega_+ \omega_-^2}{c^2} \right) \rho_-^2 \end{aligned} \quad (2.15)$$

$$\begin{aligned} \Delta\omega_{\bar{c}} = & \left( -\frac{3}{2} \frac{C_4}{d^2} \omega_- - \frac{1}{2} \frac{\omega_+^3}{c^2} \right) \rho_+^2 + \\ & \left( \frac{1}{2} \frac{B_2}{|B|} \omega_+ - \frac{1}{2} \frac{\omega_+^2 \omega_-}{c^2} \right) \rho_z^2 + \\ & \left( -\frac{1}{2} \frac{B_2}{|B|} \omega_+ + \frac{3}{2} \frac{C_4}{d^2} \omega_- - \frac{\omega_+ \omega_-^2}{c^2} \right) \rho_-^2. \end{aligned} \quad (2.16)$$

These calculations make use of the fact that

$$\omega_{\bar{c}} = \omega_+ + \omega_- \approx \omega_{\bar{c}} \quad , \quad (2.17)$$

$$\omega_+ \gg \omega_- \quad (2.18)$$

$$\text{and } \omega_- \approx \frac{V_0}{2d^2 B}. \quad (2.19)$$

Considering Eq. (2.16), it is a very interesting fact that the sum frequency  $\omega_{\bar{c}}$  as a function of the modified cyclotron radius does not depend on the  $B$  field inhomogeneities and is independent of the  $C_4$  as a function of the axial amplitude. This allows the measurement of field inhomogeneities and the ion's radius by observing frequency shifts.

## 2.2.2 Misalignment and distortion of fields

Another source of frequency shifts is a tilt of the electrostatic field axis relative to the B-field axis. An angle

of  $\Theta$  between the two will lead to a shift in the sum frequency of

$$\Delta\omega_{\epsilon} \approx \frac{9}{4}\omega_{-} \left( \sin^2 \Theta - \frac{2}{9}\epsilon^2 \right). \quad (2.20)$$

The parameter  $\epsilon$  describes the asymmetry of the electrostatic potential. This ellipticity is described by replacing Eq. (2.2) with [Wei88]

$$V = \frac{V_{\text{EC}}}{2d^2} \left( z^2 - \frac{\rho^2}{2} - \frac{1}{2}\epsilon(x^2 - y^2) \right). \quad (2.21)$$

### 2.2.3 Coulomb interaction

The three eigenmotions of a charged particle in a Penning trap are of course affected by the interactions with other charged particles. Ideally, one tries to work with a single ion. However, especially for broadband detection, the signal of a single ion is too low. Instead, more than twenty thousand ions are needed for a detectable signal.

If two ions are present in the trap and their masses are closer than the resolving power of the detection system, only one peak will be visible in the spectrum. Usually, the width of the peak is then smaller than expected from the addition of the single peaks. On the other hand, if the eigenfrequencies can be resolved separately, one observes a shift to lower frequencies and the two frequencies will approach each other [Bla06].

Yet, there is no easy model to describe a large number of particles. Simulation studies with Coulomb interaction show that ion density, ion number and the ion distribution have a great influence on the observed shifts [VG12].

### 2.2.4 Image charges

The movement of ions in a trap can be compared to the oscillation of a point charge between two parallel metal plates – the most simple capacitor. The moving charge induces charges on the electrodes to maintain an equipotential across their surface. These induced charges act back on the moving particle and thus cause a frequency shift of the magnetron frequency  $\delta$  and a shift of the modified cyclotron frequency  $-\delta$ . For a spherical ion trap of radius  $a$  this shift has been calculated to be [VDMFS89]

$$\delta = \frac{3}{2} \frac{qc}{Ba^3}. \quad (2.22)$$

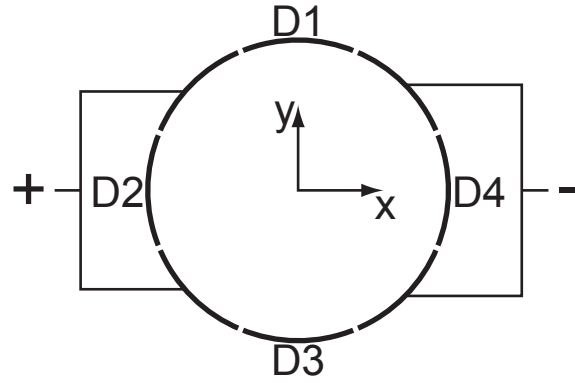


Fig. 2.3: Dipolar excitation with an eight segmented ring electrode. Plus and minus denote a relative phase shift of  $\pi$  between the applied signals. The electrodes D1 to D4 are used for detection. The orientation of the excitation segments corresponds to Eq. (2.23).

## 2.3 Excitation methods

There are several ways to excite ions in a trap. They range from a sinusoidal signal on one electrode to predefined frequency spectra translated into the time domain distributed over several electrodes. In this work the excitation signal is applied to the eight segmented ring electrode. Four of the segments are used for detection and four for excitation. A phase shift between the various segments leads to different field geometries according to the multipole expansion in classical electrodynamics. The following sections explain the first and second order term which are most commonly called dipolar and quadrupolar excitation.

### 2.3.1 Dipolar excitation

For dipolar excitation a sinusoidal signal is applied to at least two opposite electrodes with a relative phase difference of  $\pi$ . If one applies a sinusoidal signal with an amplitude of  $V_{\text{rf}}$ , an angular frequency of  $\omega_{\text{rf}}$  and a global phase  $\phi$  on a set of electrodes symmetrical to the  $x$ -axis with an inner radius  $a$ , the electric field is

$$\vec{E} = \frac{V_{\text{rf}}}{a} \cos(\omega_{\text{rf}} t + \phi) \begin{pmatrix} 1 \\ 0 \end{pmatrix}. \quad (2.23)$$

This driving field will result in a linear increase of the ions' radius with time. An example for a dipolar excitation with an eight segmented ring electrode is shown in Fig. 2.3.

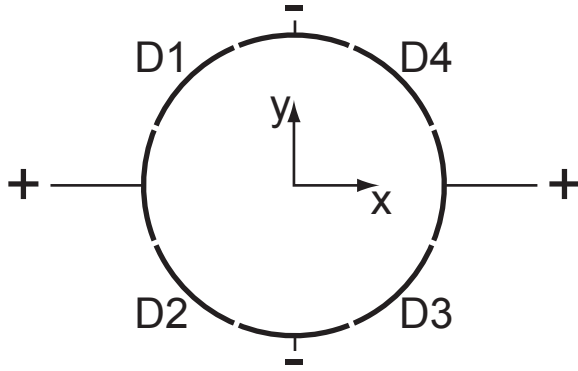


Fig. 2.4: Quadrupolar excitation with an eight segmented ring electrode. Plus and minus denote a relative phase shift of  $\pi$  between the applied signals. The electrodes D1 to D4 are used for detection. The figure is slightly rotated compared to Fig. 2.3 to match Eq. (2.24).

### 2.3.2 Quadrupolar excitation

Quadrupolar excitation is achieved by applying a signal with a relative phase shift of  $\pi$  to four electrodes. Neighbouring electrodes have a relative phase of  $\pi$  as depicted in Fig. 2.4. If the electrodes are symmetric to the x- and y-axes, the electric field in x and y direction is

$$\vec{E} = \frac{2V_{\text{rf}}}{a^2} \cos(\omega_{\text{rf}} t + \phi) \begin{pmatrix} y \\ x \end{pmatrix}. \quad (2.24)$$

This field configuration has the ability to couple magnetron and modified cyclotron motion. If the applied frequency equals the sum frequency ( $\omega_{\text{rf}} = \omega_{\text{c}}$ ) a complete conversion from magnetron to cyclotron motion and back can occur depending on the duration and amplitude of the excitation signal. The modified cyclotron radius decreases while the magnetron radius increases until a full conversion has taken place and the conversion runs backwards. If the applied radio frequency does not match the cyclotron frequency, this conversion will be incomplete.

According to [Kre07], the conversion from a pure magnetron motion  $\rho_{-}(t_0)$  by a single pulse of length  $\tau$  and angular frequency  $\omega_{\text{rf}}$  is given by

$$\rho_{+}(\tau) = \rho_{-}(t_0) \sqrt{\frac{4g^2}{\omega_{\text{R}}^2} \sin^2\left(\frac{1}{2}\omega_{\text{R}}\tau\right)} \quad (2.25)$$

$$\omega_{\text{R}} = \sqrt{4g^2 + (\omega_{\text{rf}} - \omega_{\text{c}})^2}. \quad (2.26)$$

Where  $\omega_{\text{R}}$  is the so called Rabi frequency and  $g$  the

coupling parameter of magnetron and modified cyclotron motion.

### 2.3.3 Fourier limit and SWIFT

All of the excitation methods have in common that the signal is applied for a certain time only. This directly leads to spread in frequency space due to the nature of the Fourier transform. If a signal  $V_{\text{rf}}(t)$  is applied for a certain time  $t_0$ , one can calculate the frequency spectrum by applying a Fourier transform  $\mathcal{F}$

$$V_{\text{signal}}(t) = V_{\text{rf}}(t) \times \text{rect}\left(\frac{t}{t_0}\right) \quad (2.27)$$

$$\Rightarrow \mathcal{F}V_{\text{signal}}(t) = \mathcal{F}V_{\text{rf}}(t) * \mathcal{F}\text{rect}\left(\frac{t}{t_0}\right) \quad (2.28)$$

$$\text{with: } \mathcal{F}\text{rect}\left(\frac{t}{t_0}\right) = |t_0| \text{sinc}\left(\frac{\omega t_0}{2}\right). \quad (2.29)$$

Nota bene:

$$\mathcal{F}\cos\omega_{\text{rf}}t = \pi(\delta(\omega - \omega_{\text{rf}}) + \delta(\omega + \omega_{\text{rf}})) \quad (2.30)$$

$$\mathcal{F}\sin\omega_{\text{rf}}t = -i\pi(\delta(\omega - \omega_{\text{rf}}) - \delta(\omega + \omega_{\text{rf}})). \quad (2.31)$$

Hence, the frequency domain covered by a single sinusoidal signal with an angular frequency  $\omega_{\text{rf}}$  is the convolution of a delta distribution at  $\omega_{\text{rf}}$  and a sinus cardinalis. In other words, it is a sinus cardinalis of width  $2t_0$  shifted to  $\omega_{\text{rf}}$ .

From these observations, it is directly clear that a shorter excitation time results in a broad range of excitable ion frequencies. Whereas a long sinusoidal excitation covers a narrow band of frequencies only.

The Stored Waveform Inverse Fourier Transform (SWIFT) technique tries to overcome this obstacle. Instead of defining the excitation signal in the time domain, one defines the frequency spectrum of the excitation. By applying the inverse Fourier transform one can obtain the signal in time domain. The most simple excitation scheme would be to equally excite all frequencies between two boundaries: a rectangular function in frequency space. As this is the convolution of a rect function and a delta distribution, the reversal of the law in Eqs. (2.27) and (2.28) can be applied. The result is a sinus cardinalis in the time domain. This is unfavourable because the signal amplitude sharply increases which is problematic due to the limited voltage of function generators.

It has been shown that an additional phase shift which scales quadratically with the frequency will distribute the amplitudes more evenly in the time domain [GM96]. This way the spectral power can be increased.

## 2.4 Detection via induced image charges

The detection of induced image charges relies on the currents induced by the ion motion on the segmented ring electrode. The ion absorbs energy from the excitation field and releases the stored energy via the input resistance of the detection system. This detection scheme has the advantage of being a non-destructive method. This means that the ions remain in the Penning trap for further measurements.

For ions between two parallel plates at a distance  $D$  the image current  $I$  is [Sho38]

$$I(t) = q \frac{\omega_{\text{osc}} x(t)}{D}. \quad (2.32)$$

Where  $x(t)$  is the position of the ion and  $\omega_{\text{osc}}$  is the angular frequency of the oscillation. Usually, this small signal is increased by two amplification stages. The time signal gets recorded and a Fourier transform is performed. This yields a frequency spectrum containing the ion's eigenfrequencies.

The detection method is called Fourier Transform Ion Cyclotron Resonance (FT-ICR) and can be done with a narrow or a broadband amplification. For narrow band detection, usually a resonance circuit is tuned to the frequency of the ion. The signal of the interaction of the ion with the resonance circuit is recorded. For a broadband detection active amplifiers with a very low noise level are used.

Both, a dipolar or quadrupolar detection scheme can be applied depending on the wiring of the electrodes. In principle the same wiring as in Figs. 2.3 and 2.4 is used, but now the detection electrodes (D1-D4) are connected. For quadrupolar detection the channels are summed so that neighbouring electrodes have opposing phase

$$D1 - D2 + D3 - D4. \quad (2.33)$$

For a dipolar signal two adjacent electrodes have the same phase

$$D1 + D2 - D3 - D4. \quad (2.34)$$

This can be done either analogue with phase shifting circuits or digitally.

The theoretical Fourier amplitude of the induced currents has been calculated by [Kre12]. With a radial detection system more than the two radial eigenfrequencies can be detected. In principle all frequencies

satisfying the equation

$$\omega_{\text{FFT}} = m_+ \omega_+ + m_- \omega_-, \quad (2.35)$$

with  $m_+$  and  $m_-$  integers, are detectable. However, for higher absolute values of  $m_-$  and  $m_+$  the signal amplitude decreases rapidly. Dipolar detection selects all odd values for  $m_+ + m_-$  and suppresses the even. Quadrupolar detection is complementary and selects all even combinations. Due to their high amplitude and the  $1/\nu$  noise of the amplifier, the lowest order high frequency peaks at  $\omega_+$  (dipole mode) and  $\omega_+ + \omega_-$  (quadrupole mode) are most important. The signal amplitudes for dipolar ( $A_{\text{DD}}$ ) and quadrupolar detection ( $A_{\text{QD}}$ ) are given by

$$A_{\text{DD}} = \rho_+ C_{\text{DD}}(\rho_z) \quad (2.36)$$

$$A_{\text{QD}} = \rho_+ \rho_- C_{\text{QD}}(\rho_z). \quad (2.37)$$

The factors  $C_{\text{DD}}$  and  $C_{\text{QD}}$  are given by the trap geometry and calculated for the KATRIN trap in [Kre12]. It should be noted that these geometry factors strongly depend on the axial oscillation amplitude.



### 3 FT-ICR set-up at the MPIK in Heidelberg

The FT-ICR set-up at the Max-Planck-Institut für Kernphysik in Heidelberg consists of a superconducting magnet and a vacuum chamber. For the ion production, a thermionic emission source with a  $^{6,7}\text{Li}$  pellet is used. The beam is directed into a Penning trap by an einzel lens and detected with a Faraday cup at the end of the set-up. A sketch of the apparatus is shown in Fig. 3.1. A detailed description of the most important parts is given in the following sections.

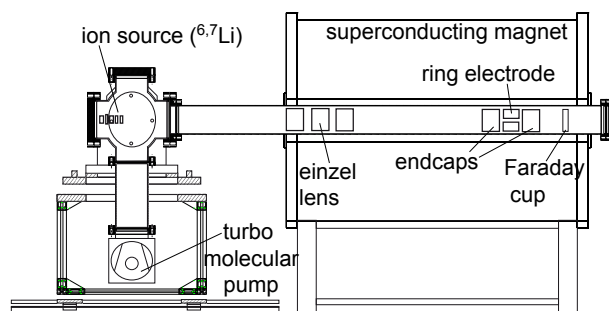


Fig. 3.1: FT-ICR set-up at the MPIK consisting of a superconducting magnet and a vacuum chamber. Ions are produced by the  $^{6,7}\text{Li}$  thermionic emission source and are guided into the Penning trap by an einzel lens. The number of trapped particles can be determined with a Faraday cup at the end of the set-up.

#### 3.1 Thermionic emission source

The thermionic emission source used in this set-up is equipped with a  $^{6,7}\text{Li}$  pellet containing the isotopes  $^6\text{Li}$  and  $^7\text{Li}$  in natural abundance (7.4%  $^6\text{Li}$  to 92.6%  $^7\text{Li}$ ). It consists of a molybdenum filament and a porous tungsten matrix with embedded  $\beta$ -Eucryptite ( $\text{Li}_2\text{O} \cdot \text{Al}_2\text{O}_3 \cdot 2\text{SiO}_2$ ). The filament is heated by an external power supply, which is in turn floated by a positive voltage to define the ion energy.

The lithium ions are created by the so-called thermionic emission: A process where ions or electrons are released by heating. This effect has been well known for hundred years and was first observed for electrons [Ric21]. In  $\beta$ -Eucryptite the lithium atoms are loosely

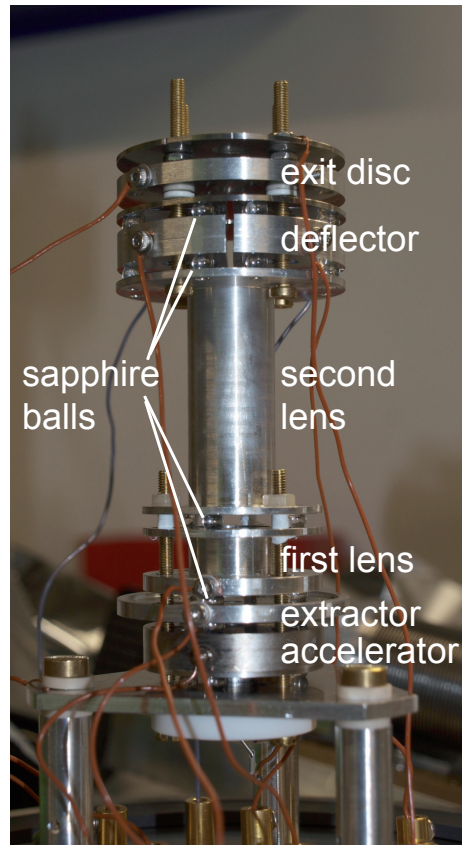


Fig. 3.2: Thermionic emission source consisting of a  $^{6,7}\text{Li}$  pellet (not visible) and an attached ion optics. From bottom to top, one can see the accelerator and extractor (two small cylindrical plates), two lenses (longer cylindrical objects), the four segmented deflector and the exit disc. Sapphire balls are placed between the elements for insulation.

bound to the oxygen atoms and sit in large interstitial lattice holes. The oxygen has strong bonds to the silicon and aluminium which cause the structure to expand non-uniformly when heated. This widens the lattice openings for the lithium atoms and thus they are dragged to the surface of the pellet by the externally applied electric field. Due to the low work function of  $\beta$ -Eucryptite, which is only 1.94 eV [FO95], lithium atoms are readily ionized. These ions are repelled by the floating voltage of the pellet; thus a continuous ion beam is achieved [BJ36, Gan91].

These newly generated ions are accelerated and extracted by two cylindrical discs with a hole in the middle called accelerator and extractor as illustrated in Fig. 3.2. A set of two lenses and four deflectors can be used to focus and deflect the ion beam. The individual parts of the source are insulated from each other by sapphire balls. The whole source is mounted on a CF-160 flange with custom made Safe High Voltage (SHV) feed-throughs. The typical lithium current is approximately 20 nA directly behind the last optical element, although up to 1 mA can be reached [Gan91].

## 3.2 Ion optics

To focus the beam, an einzel lens has been added to the set-up. Basically, einzel lenses consist of a cylinder cut in three cylindrical pieces. A high voltage applied to the middle electrode widens the ion beam at the centre of the lens. Because the electrostatic potential of the lens is symmetric, a widening in the middle automatically results in a compression at the exit of the lens. Hence, the beam is focussed. The source is approximately one and a half metres from the homogeneous region of the magnet, so this ion guidance is necessary. Otherwise, the magnetic mirror would greatly limit the transmission through the magnet.

In this set-up, the three equal einzel lens segments are each subdivided into four hyperbolic electrodes, which form a quadrupole as illustrated in Fig. 3.3. This enables ions to be deflected in the  $x$  and  $y$  direction and to be focussed. If the lens is used for deflection purposes, two neighbouring electrodes of one segment are usually connected to ground and the opposing electrodes are connected to a high voltage supply. To repel and attract ions this device has to provide negative and positive voltages. If the lens is solely used for focusing purposes, the four electrodes of each segment are connected to the same voltage.

The einzel lens was manufactured by the RoentDek Handels GmbH<sup>1</sup> and special care was taken to select non-magnetic materials so that the lens can be placed



Fig. 3.3: Einzel lens consisting of three segments in longitudinal direction which in turn are subdivided into four electrodes. Latter form a set of three quadrupoles.

in the inhomogeneous region of the magnetic field. For all high voltages an HV 500 from Stahl-Electronics was used. This device has voltage fluctuations of only 0.6 mV for a DC voltage of 10 V [Hec12].

## 3.3 Superconducting magnet

The superconducting magnet was assembled by Oxford Instruments<sup>2</sup> and has a homogeneous field strength of 4.6993(2) T. The inhomogeneity per cubic centimetre was calculated to be  $\delta B/B = 5.42 \times 10^{-6}$  [UD11].

A deviation from a homogeneous magnetic field can be described by a  $B_2$  term as shown in Eq. (2.10). Previously, a value of  $-182(11)$  nT mm<sup>-2</sup> has been measured for  $B_2$  with an NMR probe. However, as the magnet was shimmed during the work presented in this thesis, its value has changed slightly between the different measurements. The major part of this thesis relies on measurements that were conducted after the magnet was shimmed. The only exception is the Coulomb interaction study presented in Section 5.4. For a

1. RoentDek Handels GmbH, Im Vogelshaag 8, D-65779 Kelkheim, Germany

2. Oxford Instruments Head Office, Tubney Woods, Abingdon, Oxfordshire, OX13 5QX, United Kingdom

detailed description of the shimming of the magnet see Section 4.2.3.

The magnetic flux decreases over time because of the flux creep phenomenon (see [And62]). A temporal stability measurement yielded a  $\Delta B/(B\delta t)$  of  $2.50 \times 10^{-11} \text{ min}^{-1}$  which causes a negligible frequency shift for the measurements presented in this thesis. All the initial magnet tests are presented in [UD11]. The thermal fluctuations were determined to be  $1 \mu\text{T K}^{-1}$  [Hec12].

### 3.4 Penning trap

For all experiments a cylindrical, three-electrode Penning trap was used. It was designed by Stahl-Electronics<sup>3</sup> for the KATRIN experiment and modified at the MPIK. The eight segmented ring electrode and two segmented endcaps are shown in Fig. 3.4. The segmentation of the ring electrode is necessary to define electric fields with dipolar or quadrupolar symmetries and to separate detection and excitation. Four of the segments are used for detection and four for excitation. The KATRIN traps that are presented in Chapter 6 have a four segmented ring only. In both cases the ring electrode has a length of 56 mm and the endcaps are 89 mm long with a gap of 3 mm in between ring electrode and endcaps.

The electrodes are made out of oxygen free copper (1 mm) that is in turn plated with  $50 \mu\text{m}$  silver and  $0.5$  to  $1 \mu\text{m}$  gold to minimize oxidation and to ensure a well-defined surface potential across the electrodes. The inner diameter is 70 mm and the trap has a total length of 260 mm. For insulation PolyEther Ether Ketone (PEEK) spacers with PEEK screws are placed between electrodes and housing. PEEK has the advantage of a low outgasing rate compared to other polymers.

The housing is made out of aluminium magnesium alloy to limit its influence on the  $B_2$  term of the magnetic field. On top of it, the filter and preamplifier boards are mounted. The filter boards are used to limit noise on the endcaps and consist of RC filters that limit high-frequency noise and diodes that bypass the filters to allow fast switching of the endcaps. The preamplifier and filter board are shown in Fig. 3.5 and discussed in Section 3.5.1.1.

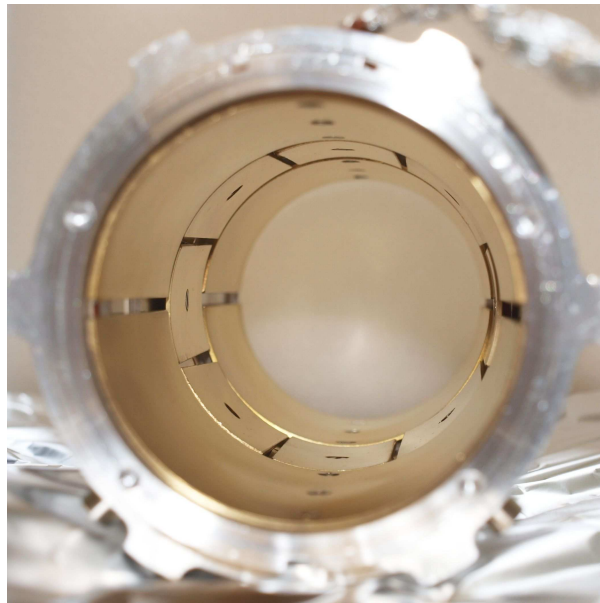


Fig. 3.4: The cylindrical Penning trap consists of two  $180^\circ$ -segmented endcaps (one close and one further away) and an eight segmented (each  $45^\circ$ ) ring electrode in between. All electrodes are made of gold plated oxygen free copper. The housing is made of aluminium magnesium alloy.

## 3.5 Detectors

### 3.5.1 Image charge detection system

An estimate using Eq. (2.32) yields that a couple of thousand ions moving in a Penning trap result in induced currents of a few pico-amperes. To detect these, a two stage amplification set is used. The first (pre-) amplifier is mounted directly onto the Penning trap and the second (post-) amplifier is situated just outside the vacuum.

#### 3.5.1.1 Preamplifier

The preamplifier consists of two identical electronic boards which have four identical channels in total, one for each detection segment. It is mounted directly onto the Penning trap as shown in Fig. 3.5. This ensures least cable length to the electrodes resulting in a better signal-to-noise ratio. The aim of the preamplifier is to increase the signal just enough for the postamplifier which is connected by 1.5 m of cryogenic coaxial cable.

<sup>3</sup> Stahl-Electronics, Hauptstrasse 15, D-67582 Mettenheim, Germany



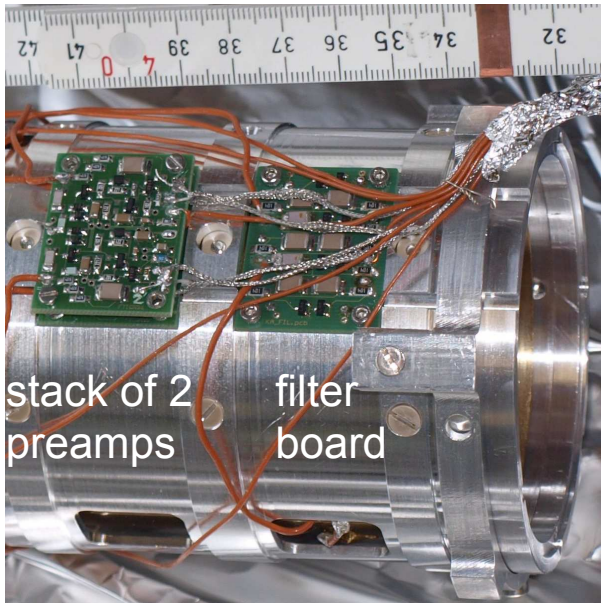


Fig. 3.5: The preamplifier is mounted directly onto the Penning trap housing. As the trap originally had two detection electrodes, two copies of the original board are mounted on top of each other. The filter board is used to reject high-frequency noise to the endcaps. The filters for the excitation electrodes are not connected.

It is designed as a broadband amplifier with a range of approximately 50 MHz.

The KATRIN amplifier has high impedance inputs with GaAs Field Effect Transistors (FETs) to be able to detect small currents. GaAs has been chosen due to its low input current noise, but has the deficiency of requiring a thorough selection. The preamplifier is able to do a voltage amplification by 7 dB at 5 MHz and converts a high input impedance of 1 M $\Omega$  and 1 pF to 75  $\Omega$  output impedance. This results in a high power amplification. The preamplifier has a low input voltage noise density of 1 nV Hz<sup>-1/2</sup> at 300 K and was designed by Stahl-Electronics. For details see [UD11]. The preamplifier for the MPIK set-up has similar characteristics but the GaAs FETs are exchanged by Si transistors.

### 3.5.1.2 Postamplifier

The postamplifier is mounted on a CF-160 flange with vacuum feedthroughs. This has the advantage of keeping cables short and ensuring a good ground connection. As depicted in Fig. 3.6, the housing of the amplifier is equipped with several coaxial and a power plug to facilitate the connection process.

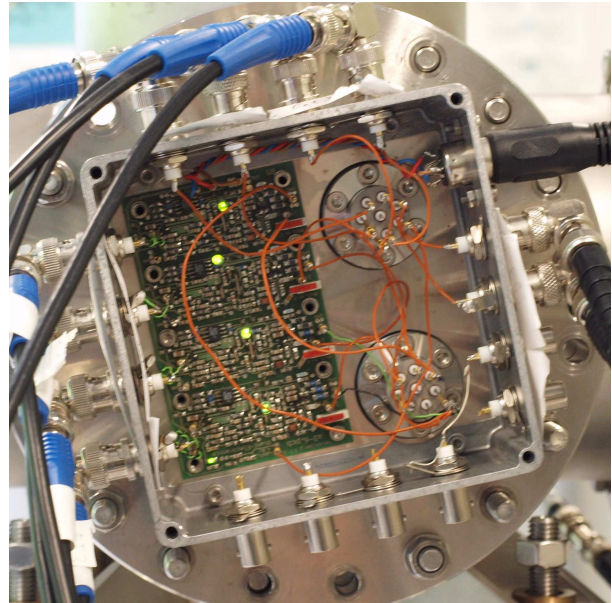


Fig. 3.6: The postamplifier is mounted directly on a CF-160 feedthrough flange and has four light emitting diodes indicating that the four channels of the preamplifier are working. The upper feedthrough is used for all ingoing signals (excitation, endcaps and power supply) and the lower for all outgoing signals (detection and ground).

The amplifier itself is silicon based and has a 100 fold voltage amplification without termination (measured at 1 MHz). It works in field strengths of up to a few millitesla. Additionally, a power supply for the preamplifier is placed on the board of the postamplifier to limit noise that might arise from external voltage sources. As well as the preamplifier, the flange and the board were designed by Stahl-Electronics.

## 3.5.2 Faraday cup

The principle of a Faraday cup is to detect charged particles impinging onto a metal plate. Sensitive amperemeters are able to measure small currents in transmission measurements (a few nanoamperes). The Faraday cup depicted in Fig. 3.7 is home made and has the two basic ingredients needed: an insulated metal plate for ion detection and an insulated grid that serves two purposes. On one hand, it can be used to reflect secondary electrons emitted from the metal plate and thus increase the signal amplitude. On the other hand, it limits the influence of stray fields. For example,



Fig. 3.7: Faraday cup with a metal grid attached to it. The grid can be used to reflect emitted secondary electrons and reduces induced signals from switching the endcaps of the Penning trap. Polyamide screws (ivory-coloured) are used to insulate the cup from the holder (not shown). Taken from [UD11]

switching the endcaps results in a high induced signal on the metal plate, if no grid is used.

To be able to determine the number of ions ejected from the Penning trap, a Quick Charge amplifier (QCP) can be connected to the Faraday cup. It has been calibrated by applying a sinusoidal signal to the input to retrieve the amplification factor. In a second step, a capacitor with precisely known capacity  $C_1$  was added in line with the Faraday cup and a small sinusoidal signal was applied with a function generator. The two capacitors act as a voltage divider as illustrated in Fig. 3.8. Hence, the unknown capacity ( $C_2$ ) can be calculated by applying a sinusoidal signal of amplitude  $V_{\text{applied}}$  and angular frequency  $\omega$

$$\frac{V_{C1}}{V_{C2}} = \frac{\frac{1}{i\omega C_1}}{\frac{1}{i\omega C_2}} \quad (3.1)$$

$$C_2 = C_1 \frac{V_{\text{applied}} - V_{C2}}{V_{C2}}. \quad (3.2)$$

The voltage drop over the Faraday cup was determined with the QCP and its amplification. The well-known formula  $Q = CV$  and the amplification factor were

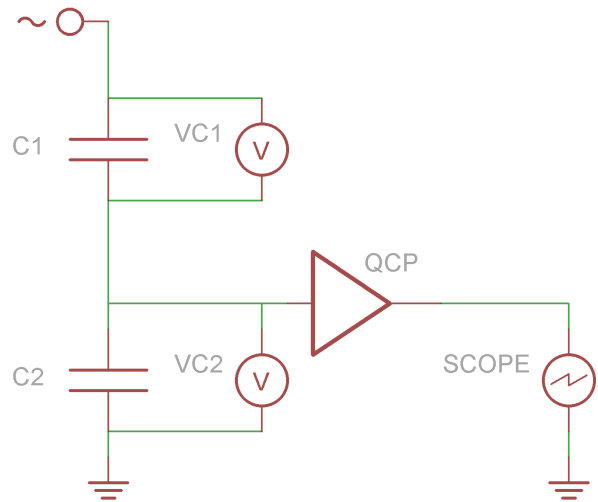


Fig. 3.8: The network used for determining the capacity of the Faraday cup consists of a precisely known capacitor  $C_1$ , the capacity of the Faraday cup  $C_2$  and the QCP. A function generator is used to apply a sinusoidal signal with an amplitude of  $V_{\text{applied}}$ . The voltages  $V_{C1}$  and  $V_{C2}$  cannot be measured directly.

then used to determine the sensitivity of the detection. The signal of the QCP corresponds to approximately  $5 \text{ mV}/10\,000 e^+$ .

### 3.6 Transient recorder

The transient recorder is a LabVIEW controlled data acquisition PC card by Spectrum Systementwicklung Microelectronic GmbH<sup>4</sup> that records input signal at discrete time points. The model used (M2i.3026) has the advantage of four input channels. This makes it possible to record all detection channels simultaneously, which enables the digital selection and simultaneous use of quadrupolar and dipolar detection schemes, respectively.

The card features a recording rate of 50 MHz when four channels are recorded and has a 12 bit analogue digital converter with a variable input voltage range. Due to the Nyquist–Shannon sampling theorem, this allows the simultaneous recording of signals of up to 25 MHz. The data acquisition is externally triggered by the function generators used to apply the excitation.

<sup>4</sup> Spectrum Systementwicklung Microelectronic GmbH, Ahrensfelder Weg 13-17, 22927 Großhansdorf, Germany

An external reference clock is connected to ensure frequency measurements with an accuracy better than 0.1 Hz in 21 MHz. This value is currently limited by the data size of the four transients.

The transient length  $t_{\text{tr}}$  can be calculated from the number of samples  $N$  and the recording rate  $\nu_{\text{tr}}$

$$t_{\text{tr}} = \frac{N}{\nu_{\text{tr}}}. \quad (3.3)$$

## 4 Ion Transport

The ion transport into the Penning trap is governed by two effects: the deflection and focussing of the beam by electrostatic potentials and the guidance and radial compression by the magnetic field lines. Using the Simion<sup>1</sup> programme both can be simulated.

### 4.1 Simulation of the trapping procedure with Simion

#### 4.1.1 Simulation and calculation of the magnetic field

For a simulation of the ion trajectory it is important to pay attention to the diverging magnetic fields since they cause compression and reflection of the beam. Unfortunately, Simion does not support fields with a non-vanishing curl natively. Only gradient fields are supported. This limitation was overcome by the use of a user defined Simion programme which can alter Simion's field map.

To implement the magnetic field, it is necessary to know the magnetic field vector at every position in space. As it is not feasible to measure all three vector components at every point in the set-up, a different scheme was used. The magnetic flux density along the symmetry axis was measured with an NMR probe in the homogeneous region and with a Hall probe in the inhomogeneous region as shown in Fig. 4.1. The magnetic field was modelled with a pair of Helmholtz coils which turned out to be inaccurate both in the homogeneous and inhomogeneous region. As a next step five current loops with the same radius, but independent axial positions were fitted to the data. The radius and the position of these loops were used in a second step to model the overall field using Biot-Savart's law.

For a loop  $\gamma$  with a current  $I$  and the vacuum permeability  $\mu_0$  the  $B$  field is given by

$$\vec{B} = \frac{\mu_0}{4\pi} \oint_{\gamma} \frac{I d\vec{l} \times \vec{r}'}{|\vec{r}'|^3}. \quad (4.1)$$

Where  $\vec{r}'$  is the displacement vector and  $\vec{l}$  the vector along the current loop. For a cylindrical loop around the origin, which is parametrized by  $\theta$  (which runs

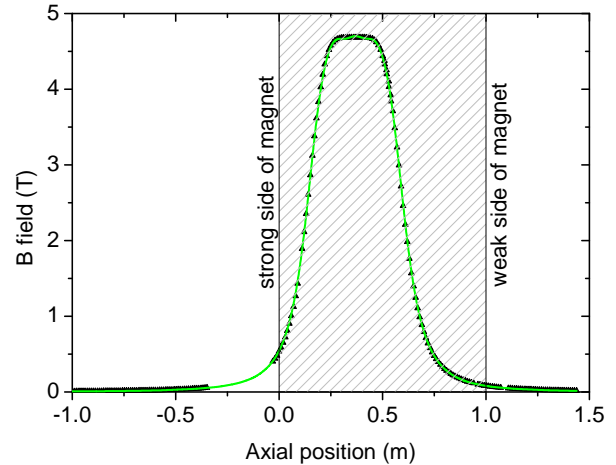


Fig. 4.1: The magnetic field along the symmetry axis of the magnet. A hall probe and an NMR probe were used for the inhomogeneous and homogeneous region, respectively. A fit of five current loops with the same radius and current is shown in green. The data are shown as black triangles. The bore of the magnet is approximately 1 m long (shaded area). The homogeneous region is not in the centre of the magnet but shifted to one side: the so-called strong side of the magnet.

from 0 to  $2\pi$ ) and which has a certain radius  $R$ , the path  $\gamma$  is given by the vector  $\vec{l}$

$$\vec{l} = R \begin{pmatrix} \cos \theta \\ \sin \theta \\ 0 \end{pmatrix} \quad (4.2)$$

$$\Rightarrow d\vec{l} = R \begin{pmatrix} -\sin \theta \\ \cos \theta \\ 0 \end{pmatrix} d\theta. \quad (4.3)$$

Thus, the displacement vector  $\vec{r}'$  is

$$\vec{r}' = \begin{pmatrix} x - R \cos \theta \\ y - R \sin \theta \\ z - 0 \end{pmatrix}. \quad (4.4)$$

1. Scientific Instrument Services, Inc., 1027 Old York Road, Ringoes, New Jersey 08551-1054, United States of America

Because the problem is symmetric around the z-axis the angular component of  $\vec{B}$  vanishes. Using this, the radial, azimuthal and axial component,  $B_r$ ,  $B_\phi$  and  $B_z$ , can be calculated from the xz-plane only:

$$\vec{B}|_{y=0} = \frac{\mu_0 IR}{4\pi} \int_0^{2\pi} \frac{\begin{pmatrix} -\sin \theta \\ \cos \theta \\ 0 \end{pmatrix} \times \begin{pmatrix} x - R \cos \theta \\ 0 - R \sin \theta \\ z - 0 \end{pmatrix} d\theta}{\left| \begin{pmatrix} x - R \cos \theta \\ 0 - R \sin \theta \\ z - 0 \end{pmatrix} \right|^3} \quad (4.5)$$

$$B_r = \frac{\mu_0 IR^2}{4\pi} z \int_0^{2\pi} \frac{\cos \theta d\theta}{(r^2 + R^2 - 2rR \cos \theta + z^2)^{\frac{3}{2}}} \quad (4.6)$$

$$B_\phi = 0 \quad (4.7)$$

$$B_z = -\frac{\mu_0 IR}{4\pi} x \int_0^{2\pi} \frac{(r \cos \theta - R) d\theta}{(r^2 + R^2 - 2rR \cos \theta + z^2)^{\frac{3}{2}}}. \quad (4.8)$$

These integrals were calculated numerically on a rectangular grid of 1 mm step size. The resulting field map was shifted according to the position of the five fitted current loops. The overall field was scaled to a homogeneous field strength of 4.699 T and then added to Simion as a user programme. For points that do not lie on the grid, a bilinear interpolation is applied by the programme.

### 4.1.2 Transport simulation

To get a better control over the ion beam, the whole set-up was modelled in Simion. A programme was written to scan the transport through the apparatus depending on the voltage applied to the lenses. The experiment behaved qualitatively similar to the simulations, but it was not possible to observe the experimental transmission through the magnet in the simulation and vice versa.

The low experimental transmission was reproduced in Simion when the magnetic field's symmetry axis was shifted or tilted relatively to the symmetry axis of the electrostatic potential. The impact of this misalignment on the transmission is quite severe. Even tilting angles in the range of one degree can change the transmission from nearly unity to nearly zero.

It could be observed both in the simulation and in the experiment that the voltage source used in this set-up which delivers  $\pm 500$  V is not strong enough to affect the ions within a region of 1 m around the homogeneous region. This corresponds to a range from  $-0.1$  m to  $0.9$  m for  $z$  in Fig. 4.1. The reason is that as the ions of charge  $q$  and velocity  $\vec{v}$  enter higher magnetic fields  $\vec{B}$ , the force  $\vec{F}$  acting on them gets governed by the magnetic component rather than the electric:

$$\vec{F} = q (\vec{E} + \vec{v} \times \vec{B}). \quad (4.9)$$

Considering an electric field  $E$  of  $500 \text{ V dm}^{-1}$  and  ${}^7\text{Li}^+$  with 20 eV kinetic energy, the force due to the 4.7 T magnetic field is twenty times stronger than the one from the electric. In the inhomogeneous region, the  $\vec{E} \times \vec{B}$  drift causes an additional motion in the azimuthal direction. This makes a focussing even more complicated.

### 4.1.3 Trapping efficiency

The trapping procedure can be analysed with the aid of Simion. The simulation was performed without any excitation in the following way: The region between the centres of the two endcaps, a cylinder with a length of 151 mm ( $2 \times \frac{1}{2} \times 89$  mm for the endcaps, 56 mm for the ring electrode and  $2 \times 3$  mm for the gaps between these three electrodes) and a diameter of 70 mm, was randomly filled with ions of 16 eV and a momentum in the positive axial direction. The endcaps were switched on simultaneously and with a negligible raise time. This raises the total energy of the ions according to the electrostatic potential at their respective position so that not all of them get trapped. Each ion was recorded for 2 ms, which is in the order of the time needed for one revolution of the magnetron motion. This study was carried out for numerous trapping voltages with at least two thousand trapped ions to obtain the high statistics needed for a comparison of the simulation runs.

The configuration of this simulation is similar to the KATRIN experiment where the whole beam tube is filled with particles. For the MPIK set-up, the ion beam is smaller than the trap diameter and thus the trapping efficiency depends on the trapping location. However as the exact trapping location is unknown, this simulation can be used as an estimate.

The trapping efficiency was calculated by the number of trapped particles divided by the total number of particles generated in the trap volume. This is illustrated in Fig. 4.2. Depending on the trapping location the ions have an initial magnetron and an initial axial



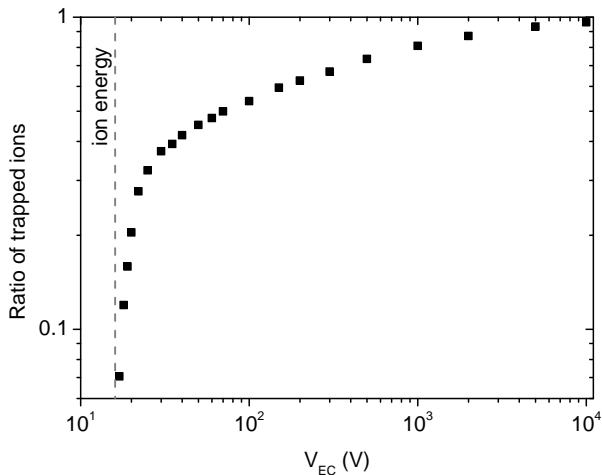


Fig. 4.2: The simulated trapping efficiency for varying trapping voltages  $V_{EC}$  increases as the voltage increases. This happens because the ions gain potential energy when the endcaps are switched on. As expected, the efficiency drops to zero as the trapping voltage approaches the ion energy of 16 eV.

amplitude. The cyclotron motion is negligible because the magnetic field lines are nearly parallel to the initial momentum.

As expected, the trapping efficiency (displayed in figure Fig. 4.2) decreases with decreasing trapping voltage. There are two reasons: On one hand, the Penning trap has open endcaps so the ions see a different barrier depending on the radius. The highest barrier is observed close to the ring electrode, at large radii. On the other hand, ions gain energy as the endcaps are switched on which is added to their initial kinetic energy which causes less ions to be trapped. This effect plays a smaller role for higher trapping voltages: The kinetic energy becomes negligible compared to the electrostatic potential. Then the turning points are defined by the energy which the ions gain when the endcaps are turned on and hardly any ions are lost.

With this information, one is able to estimate the number of trapped ions, if the transmission current is known. The number of particles  $N$  in the trap volume of length  $\Delta l$  can be calculated from the ion energy  $E$  and the transmission current  $I$  with the help of the speed of the ions  $v$ , their mass  $m$  and the time  $\Delta t$

needed to fly through the trapping volume

$$\begin{aligned} N &= \frac{Q}{e} = \frac{I \Delta t}{e} = \frac{I \Delta l}{ev} \\ &= I \frac{\Delta l}{e \sqrt{2E/m}}. \end{aligned} \quad (4.10)$$

This roughly corresponds to 45 000 ions per nA at an ion energy of 16 eV. Of course, this has to be corrected by the trapping efficiency from Fig. 4.2. Overall, this agrees roughly with the ion number measurements in Section 5.4. Yet, deviations occur because the actual trapping scheme is to raise the voltage of the endcaps consecutively so ions are reflected in the trap. This increases the efficiency roughly by a factor of two. Another source for deviations is the raise time of the used switches, which is in the order of 10 ns. This raise time decreases the amount of trapped particles – especially if they are fast.

During the simulation, the position of the ions was recorded every 0.1  $\mu$ s. The position histograms for different trapping voltages are shown in Fig. 4.3. For low voltages, one can observe that it is impossible to catch ions in the middle of the trap. This occurs, because the electrostatic potential in the trap centre is not zero but rather a fifth of the trapping voltage. The result is that the ions get an extra kick which they do not receive close to the ring electrode where the electrostatic potential is zero. The electric potential of the endcaps does not create a uniform barrier across the radius either. Towards the middle, the barrier drops to 95 % of its value at the electrodes which makes trapping in the middle even more unlikely. All in all, this results in a high magnetron radius for most ions which causes unwanted frequency shifts.

As expected, all of the panels of Fig. 4.3 show that more ions are trapped at higher radii, if the beam tube is uniformly flooded with ions. This is simply due to the fact that the volume element for a given radius scales with the circumference which increases, of course, linearly with the radius. As a result the Fourier signal will be dominated by the outer ions. Not only because they are more numerous, but also because the signal amplitude increases with decreasing distance to the electrodes.

Another aspect that should be noted is that the shape of the trapped ion cloud changes from a ‘ $\wedge$ ’ to a ‘ $\vee$ ’. The bright peaks in Fig. 4.3 at the axial edges of the potential occur because the ions are the slowest at the turning point which results in a high probability density. Close to the walls of the Penning trap this turning point is fixed by the very steep gradient of the electrostatic

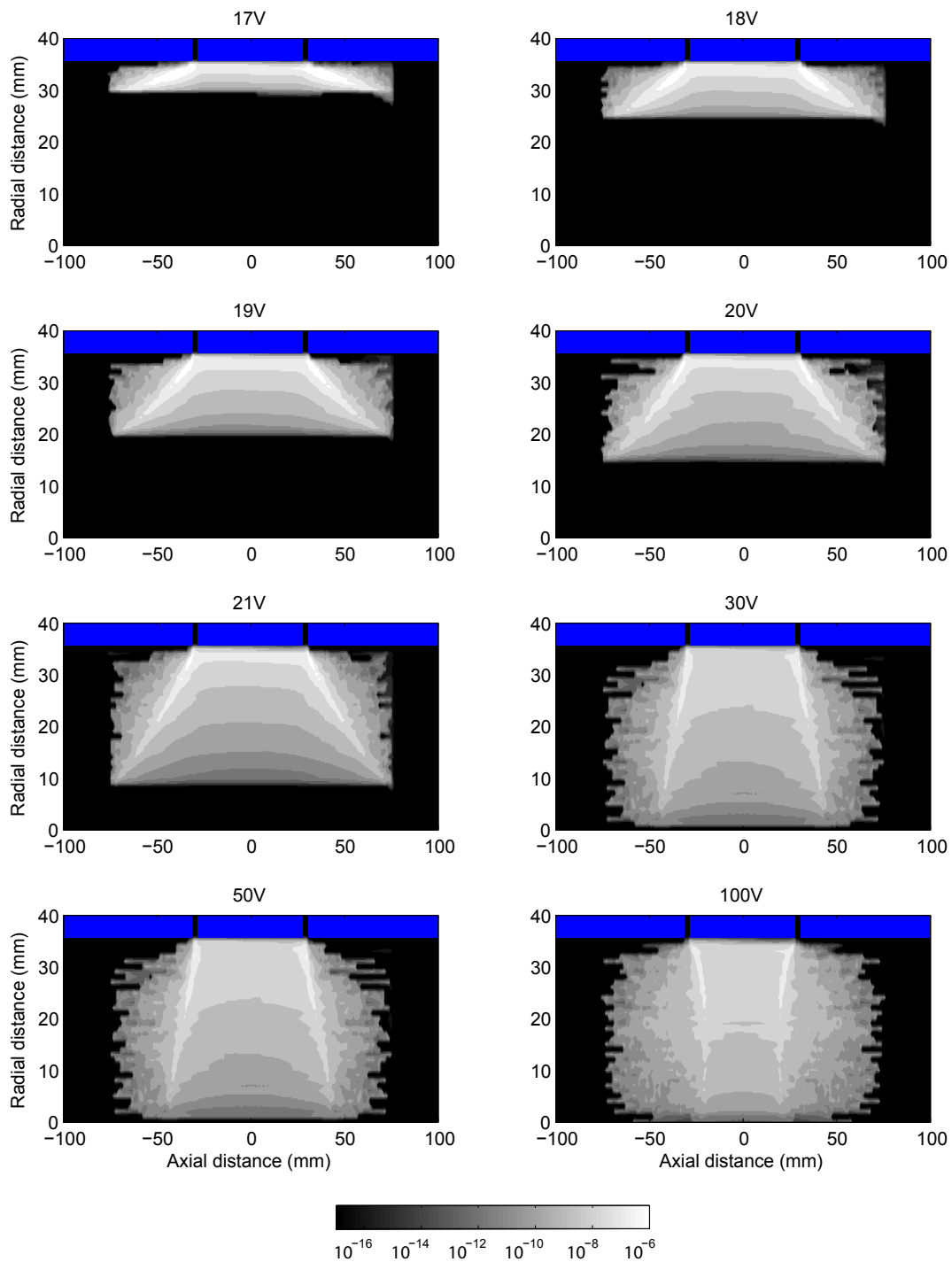


Fig. 4.3: Probability density of trapped ions with varying trapping voltages. The electrodes are shown in blue. For low voltages trapping cannot occur in the centre due to the low electrostatic barrier (the ion energy is 16 eV). One step in the colour code corresponds to a factor of 10 in probability density. Note that the ions are getting axially compressed by high trapping voltages near the centre but not near the electrodes. All histograms are normalized so that the total probability is equal to unity. For details see text.

potential at the gap between the endcaps and the ring electrode. In the centre of the trap the electrostatic field is less steep. Thus, the turning point is set by the ratio of the initial kinetic energy and the height of the electrostatic barrier. This ratio approaches zero as the trapping voltage increases. So a compression of the original ‘ $\wedge$ ’ shape to the denser ‘ $\vee$ ’ shape can be observed.

## 4.2 Magnet tests

### 4.2.1 NMR-probe measurements

The homogeneous region of the magnetic field was measured with a nuclear magnetic resonance probe from METROLAB<sup>2</sup> (Precision NMR Teslameter PT 2025). This device detects the magnetic flux by the frequency needed to drive the nuclear spin flip of deuterium which in turn depends on the  $B$  field. A holder with cylindrical plates that fit exactly into the beam tube and that are equipped with holes to accommodate the NMR probe was used. The axial position was measured from the strong side of the magnet. The radial plane is denoted by  $r$  and  $\varphi$  where  $\varphi$  is measured mathematically negative from the right hand side (in  $z$  direction) of the horizontal axis as shown in Fig. 4.4.

Figure 4.5 displays the magnetic field along the  $z$ -axis. The magnitude of the  $B$  field is asymmetric around its maximum which indicates a magnet that is not well shimmed. The axial position of the maximum of the magnetic field is not constant for all displayed radii which indicates either a tilt or a non-quadrupolar magnetic field. Both of these field errors can be reduced by changing the current in the correction coils of the magnet. There are three correction or shim coils in the MPIK magnet. Each is used for a shift in the direction of a different axis:  $x$ ,  $y$  and  $z$ .

The  $\varphi$  dependence of the magnitude of the magnetic field is illustrated in Fig. 4.6. If the magnet was ideally shimmed, there would be no  $\varphi$  dependence. The sinusoidal oscillations can arise from a shift or a tilt between the centre of the magnet and the centre of the quadrupolar field of Eq. (2.10). The amplitude of the oscillation increases with the radius because of the  $B_2$  term of the shifted/tilted field. This also leads to a shift of the mean value for a given radius. Since the minimum of the magnetic field is at an angle of  $240^\circ$ , the centre of the quadrupolar field is shifted to the top left.

Changing the current in the coils of a superconducting magnet always happens at the risk of quenching the whole magnet and it is connected to a high helium

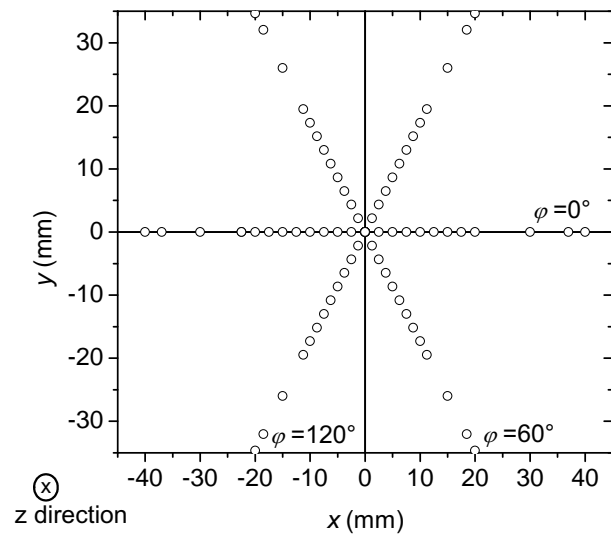


Fig. 4.4: Position of the possible measurement points (marked by a circle) for all NMR probe measurements in this chapter. In particular all of these points were used to obtain Fig. 4.9. The  $z$  axis is pointing into the paper and its origin coincides with the strong edge of the magnet (see Fig. 4.1).  $\varphi$  is measured mathematically negatively as illustrated.

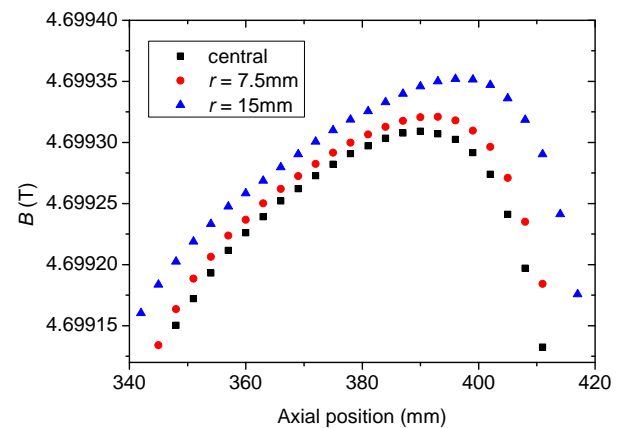


Fig. 4.5: The magnetic field  $B$  along the  $z$ -axis for different radii  $r$ . If the magnet was well shimmed, the curve should be symmetric around the maximum and the maximum for different radii should be at the same axial position.

<sup>2</sup> Metrolab Technology SA, 110, chemin du Pont du Centenaire, CH-1228, Plan-les-Ouates, Geneva, Switzerland

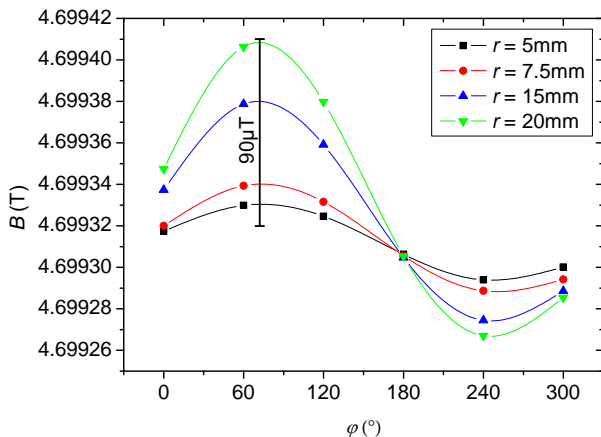


Fig. 4.6: The magnetic field  $B$  as a function of the angle  $\varphi$  along a fixed radius  $r$  displays sinusoidal oscillations which indicates that the centre of the magnet is not the centre of the magnetic field. The mean values of the oscillations increase with increasing radius because of the quadrupolar nature of the magnetic field. The data points are connected to guide the eye.

consumption. So while both of the observed shifts in the  $B$  field could be corrected with the shim coils, it was decided to first look for ferromagnetic materials in the laboratory. These have the ability to draw magnetic field lines towards them which causes the overall magnetic field to shift.

#### 4.2.2 Hall-probe measurements

The laboratory was carefully searched with a permanent magnet to detect any bigger aggregation of ferromagnetic material that might explain the irregularities of the  $B$  field. Unfortunately, the rails of the holder of the whole set-up proved to be magnetizable. To determine their influence a Hall probe from F.W. Bell<sup>3</sup> (Modell 7010 Gauss/Teslameter) was used. A probe holder was assembled from polystyrene foam to be able to maintain a constant distance to the magnet's hull.

The magnetic field in the axial direction was measured around the homogeneous region as illustrated in Fig. 4.7. The radius was set to the distance of the ferromagnetic rails from the magnet. These were the only ferromagnetic objects in the laboratory that could have caused a vertical shift. If they were the source for the inhomogeneity, a severe deviation from the expected sinusoidal should be seen. Unfortunately, it was not easy to position the holder exactly resulting in a large

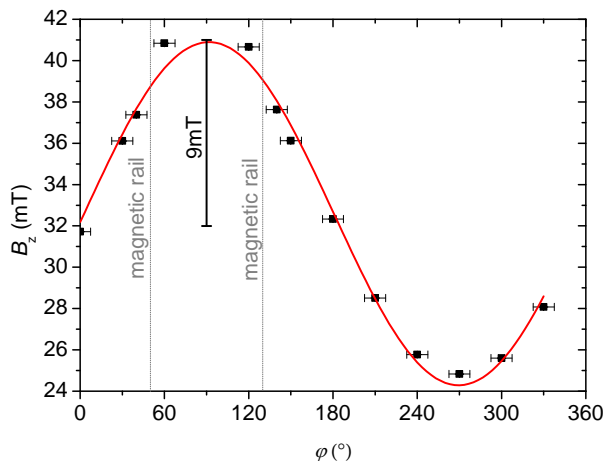


Fig. 4.7: Hall probe measurements of the magnetic field  $B_z$  in the axial direction around the centre of the magnet. The ferromagnetic rails are marked. A sinus (red) is fitted to the data. The oscillation amplitude is two orders of magnitude higher than in Fig. 4.6. Whether this is due to the shim coils cannot be determined without any specific information on the coil geometry.

error on the angle. Yet, within the error bars the data points fit quite well to the expected sinus.

As all other possibilities to remedy the shifted magnetic field were ruled out, it was decided to shim the magnet.

#### 4.2.3 Shimming of the magnet

The superconducting magnet was shimmed using the 10 Channel Shim Supply delivered with it. The connection to the coils is made via a socket in the liquid helium reservoir. In order to gain access, a protection plug has to be unscrewed with a long metal rod. Then a current lead can be installed. Initially, the shim coils were charged with the values of the last charging procedure which was back in August 2008. This serves the purpose of verifying the starting conditions as there is no possibility to check the actual current in the coils. During the whole procedure, the current in the main coil was not changed as there is a high possibility of inducing a severe quench. No deviation from the previous magnetic field could be detected with the NMR probe after the initial recharging.

3. Meggitt PLC, Atlantic House, Aviation Park West, Bournemouth International Airport, Christchurch, Dorset, BH23 6EW, United Kingdom

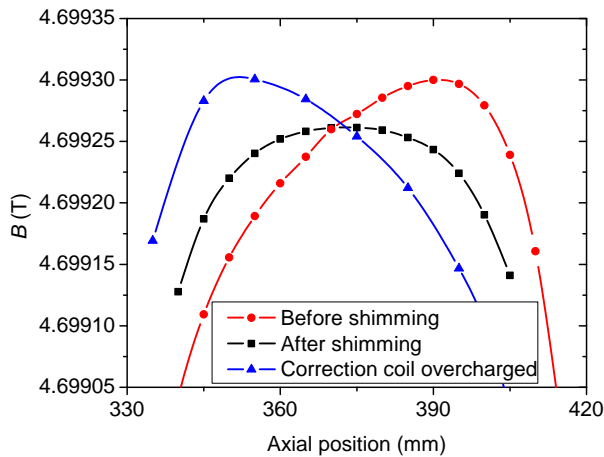


Fig. 4.8: Shimming the z correction coil shifts the maximum of the magnetic flux density to lower values of  $z$ . The initial state is shown in red, the optimized state after shimming is shown in black. Blue shows what happens, if the shimming coil is charged too much: The  $B$  field is as asymmetric as the initial state, but the steep and the flat edge are exchanged. Note that the optimal state is symmetric regarding the maximum. The data points are connected to guide the eye.

The shimming procedure itself is an iterative process: The current in one shim coil is decreased slightly and the magnetic field monitored after the current has stabilised. If the field is closer to the wanted configuration, the change was in the right direction and can be repeated. Otherwise the current has to be increased. This process is repeated until the right value for the current is found. Ideally, the shim coils do not affect each other, but in reality this is the case. So, after all coils are set, one has to repeat the whole process until a stable configuration is reached.

An example for the z shim coil is shown in Fig. 4.8. The starting configuration is not optimal as it is very asymmetric. The shimming procedure is finished when a symmetric  $B$  field is achieved. If the shim current has been changed too much, a similar curve as in the beginning is measured – the only difference is that it the steep and flat edge are exchanged.

In the present magnet there are one main coil and three shim coils to correct the field in x, y and z direction. Unfortunately, it was not possible to change the current in the x and y shim coils. No change in the  $B$  field could be detected with the NMR probe, when the current in those coils was varied. As all coils are in the liquid helium reservoir, it is very difficult to say

why this happened. Superconducting coils are charged by heating a small part of them to destroy the superconducting phase in this area. As the resistance of the coil is then non-zero, a voltage can be applied. This directly leads to a current in the coil. After the charging is complete, the heating device is turned off and the coil becomes completely superconducting again. The power supply indicated that the heater itself was working for both coils, so probably the coils got disconnected from the plug.

Generally, there are two major events that can cause a coil to become disconnected. Either the magnet is shaken too much during transport or something magnetic is lost inside the magnet. Usually, the coils are suspended with small wires to limit heat conductivity. This makes them very fragile concerning oscillations and large forces. Four years ago, a steel plate fell into the bore of the magnet. Due to the strong magnetic force, a pulley had to be used to detach it from the magnet. According to Newton's third law the same force was acting on the suspension of the coils which might have destroyed some of the wires. Yet, it could not be determined whether the shim coils were working the last time the magnet was charged as there had been no NMR probe available to check the magnetic field. So the observed shifts could have been present for a long time.

What is more problematic than the fact that the correction coils cannot be used any more is the fact that they are still superconducting and possibly charged. If one uses room temperature coils to shim the magnet, those will inevitably change the current in the superconducting coils. If by accident the critical field density is reached, a sudden phase collapse will occur releasing all the energy stored in the coil. This would probably result in massive evaporation of liquid helium so all other coils would lose their superconductivity as well. The magnet would quench.

The coefficient  $B_2$  of the shimmed magnetic field was determined from Fig. 4.8 to be  $-57.9(19) \text{ nT mm}^{-2}$  in axial direction. The quadratic fit was performed between 360 and 385 mm from the strong side of the magnet at a radius of 0 mm. The value of  $B_2$  decreased by a factor of three compared to the value in Section 3.3 of  $-182(11) \text{ nT mm}^{-2}$ .

Figure 4.9 displays the magnitude of the magnetic flux density for different axial positions. One would expect a quadratic well in the radial direction which is visible in Fig. 4.9h. Towards the axial centre of the homogeneous region, the centre of the well moves to the top left and even leaves the plane detectable with the holder due to reasons that might be explained by the simulation performed in Section 4.2.4. Yet, at both

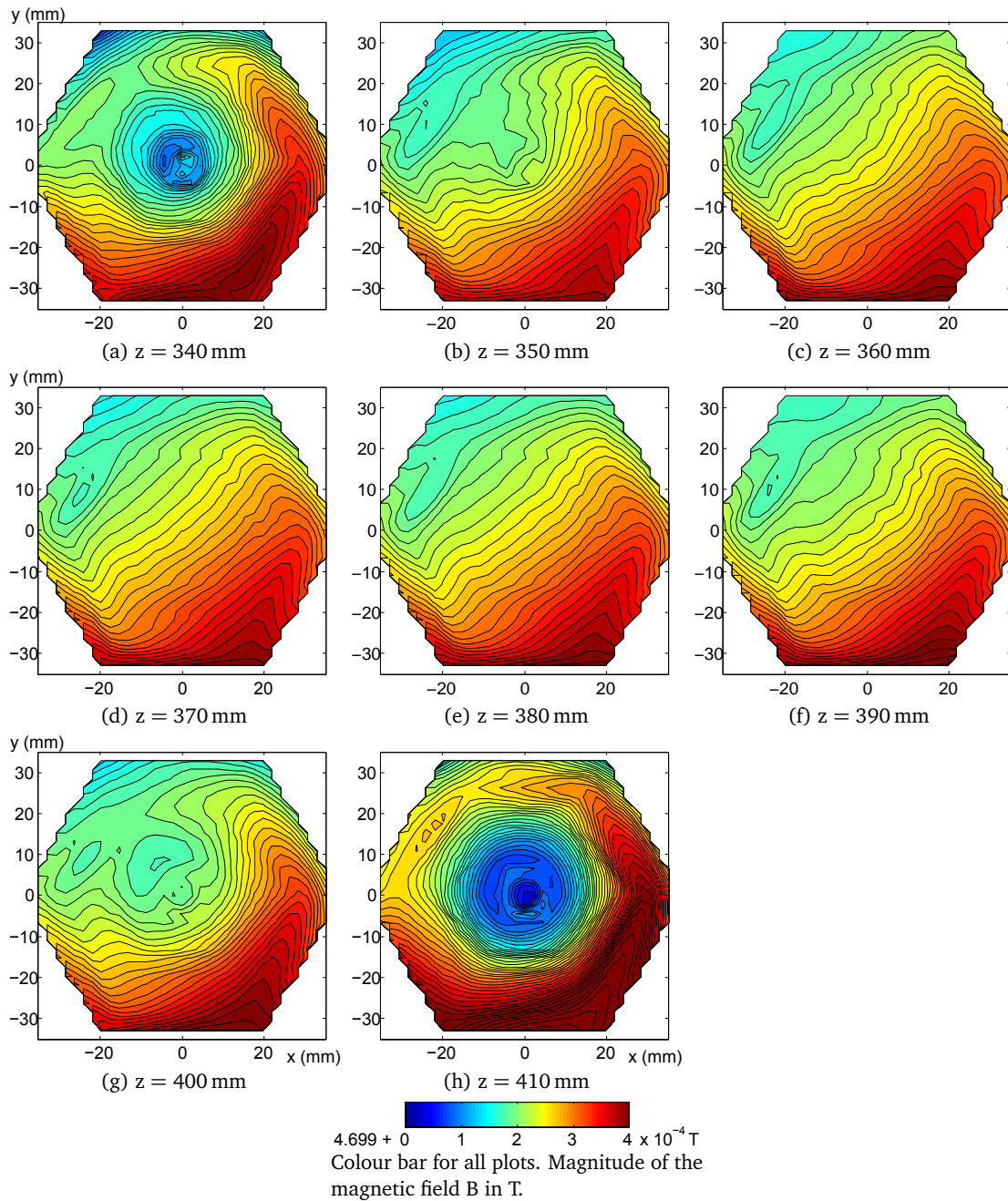


Fig. 4.9: The magnitude of the magnetic field in the plane perpendicular to the magnet's symmetry axis for different positions  $z$ . All planes are shown from the strong side of the magnet. The axes are scaled in mm. The colour code represents the deviation from 4.699 T. According to Fig. 4.8 the homogeneous region is between 370 and 380 mm. The expectation is to see a clear minimum in the centre of the plot as in panel (h). It can be seen that the homogeneous region in the radial direction leaves the detectable plane at 350 mm and only returns 5 cm later. The reason might be explained by the simulation in Section 4.2.4.



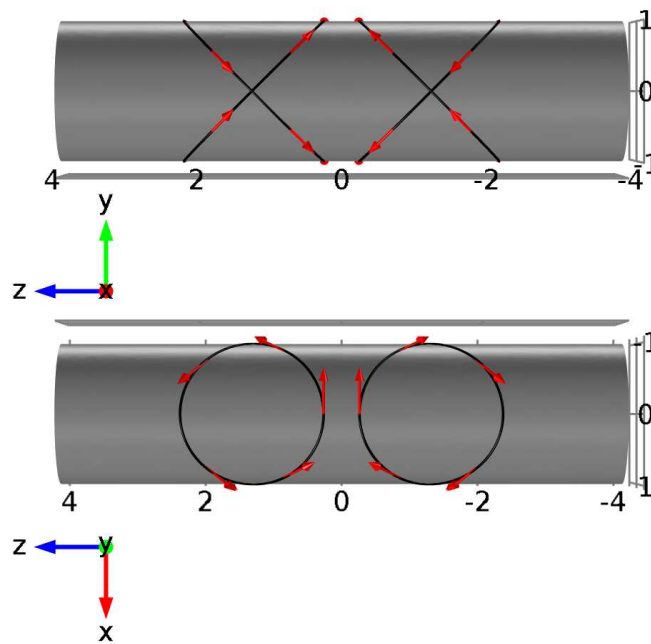


Fig. 4.10: Model for the simulation of the shim coils, all dimensions are in arbitrary units. The centres of the current loops of the correction coil are at 1.25 units and  $-1.25$  units. The direction of the current is given by the red arrows.

axial ends of the homogeneous region the plots look as expected.

#### 4.2.4 Simulation of the magnetic field

To reproduce the data from Fig. 4.9 the magnetic field was simulated. As there is no information about the internal structure of the magnet available, possible configurations were tried until the result matched the experiment best. The chosen coil configuration is displayed in Fig. 4.10 and was taken from [RH84, Fig. 7]. This kind of coil is responsible for a first order correction in  $y$  direction. One exemplary current loop, represented by the path  $p$ , is given by

$$\vec{p} = \begin{pmatrix} -\cos \xi \\ \sin \xi \\ 1.25 + \sin \xi \end{pmatrix} \quad (4.11)$$

where  $\xi$  runs from 0 to  $2\pi$ . The other current loops are likewise. This configuration causes a shift in the radial direction. However, the way this works is rather involved because it is an interaction of a quadrupolar field with the field of the correction coils. The interested reader is referred to [RH84], which deals in great detail with the construction of shim coils for all direc-

tions and various orders of correction. The MPIK magnet is only equipped with three first order correction coils so no higher order effects were simulated.

For the main coil, a cylinder with a length of 8 units and a diameter of 2 units was chosen. A current was set to circulate around the whole surface of this cylinder with a current density of  $1 \times 10^6$  A/unit. As expected, this leads to a quadrupolar  $B$  field at the centre of the coil. The current in each loop was set to be 200 A. The currents in main and shim coil were chosen arbitrarily until their effect was clearly visible. There is no possibility to compare these currents with the experimental values as the number of windings and the exact geometry of the coils are unknown. The result is illustrated in Fig. 4.11 and shows some resemblance to Fig. 4.9. Looking at the  $B$  field in planes perpendicular to the symmetry axis of the main coil, one observes a shift of the minimum of the magnetic field away from the radial centre. If one moves towards the axial centre of the main coil, this minimum moves out in radial direction. This is nearly the same behaviour as seen in Fig. 4.9.

It has been mentioned in Section 4.2.3 that the  $x$  and  $y$  shim coils are not (dis)chargeable any more. Yet, they remain superconducting and might still be charged. Thus, the similarity between Fig. 4.9 and

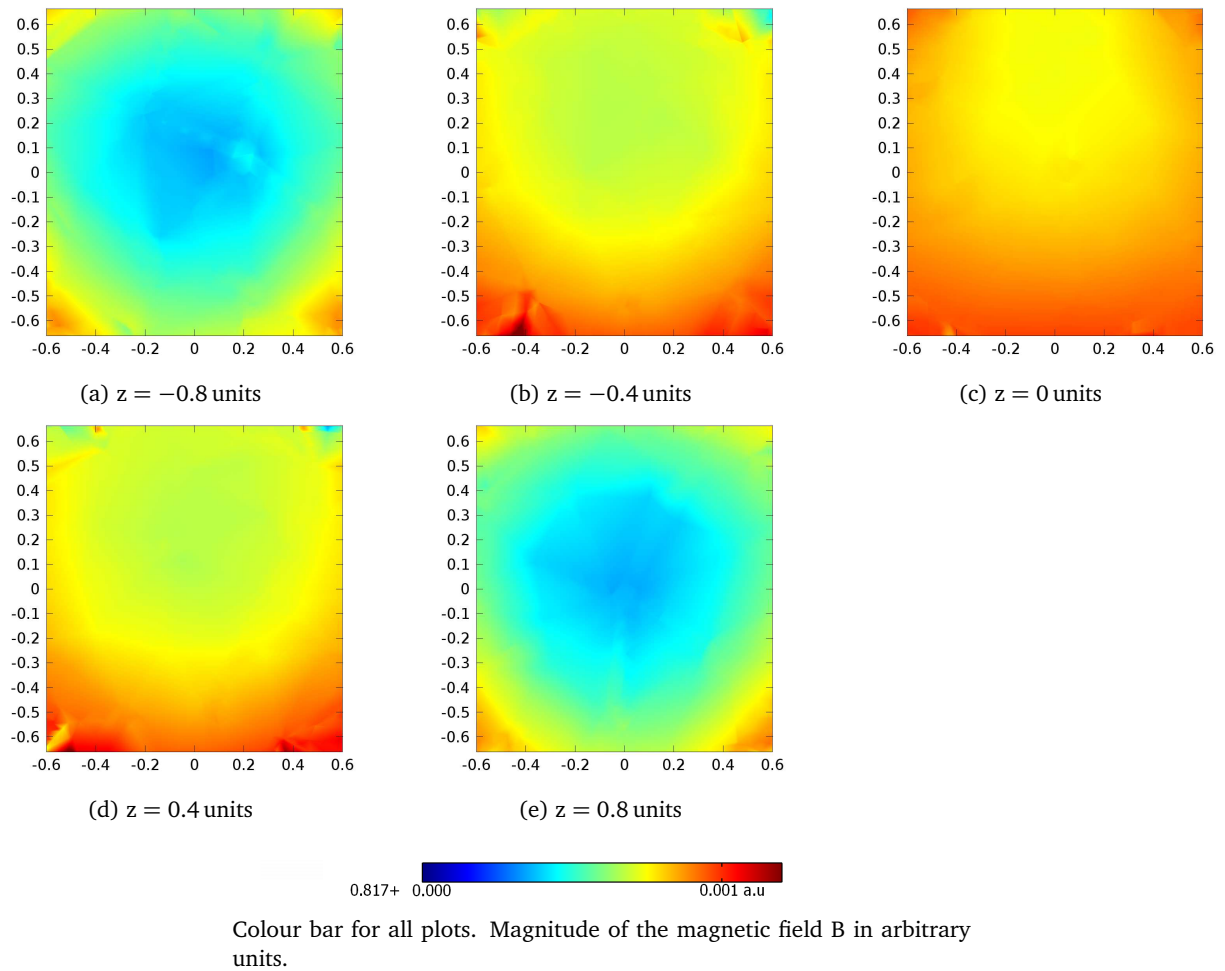


Fig. 4.11: Simulated  $B$  field of the model shown in Fig. 4.10. Similar to Fig. 4.9 cuts perpendicular to the symmetry axis at different axial positions are shown. The colour represents the magnitude of the magnetic flux. All values are given in arbitrary units. As in Fig. 4.9 the minimum of the magnetic field moves radially out of the detection plane as the axial centre of the magnet is reached. The shift in the  $B$  field is symmetric around  $z = 0$ .



Fig. 4.11 could mean that the two correction coils are charged and perturb the magnetic field in an unwanted way. However, the direction of the shift is not the same in simulation and experiment (upwards compared to up-left) because there is only one shim coil present in the simulation. Since the Maxwell-equations are linear, shim coils in  $x$  direction should have the same influence as the ones in  $y$  direction. If both are charged with different currents, any displacement in the radial direction can be achieved. Thus, it is sufficient to show that the simulation of one shim coil causes a rotated version of the data.

While this simulation is able to reproduce the data, it is not the only way to do so. For example a kink in the middle of the main coil produces exactly the same shift. There might be no obvious reason why this kink should be present, but as the magnet is more than twenty-five years old there have been numerous possibilities for one of the suspension threads (which are quite slender because this limits heat conductivity) to break. Furthermore, care should be taken because there is no sketch of the magnet's interior available. In principle the coils might look very different from the configuration of Fig. 4.10. The only way to settle the issue would be to open the magnet. But as the reassembling could take a couple of months, it is not advisable. A possibility to remove these currents is to quench the magnet, but loading the main coil might induce new currents in the disconnected shim coils. For the moment there is no option but to continue with measurements that are not affected by this  $B$  field shift.

#### 4.2.5 $B_2$ measurement with ${}^7\text{Li}^+$ after shimming

To verify the magnetic field data from Section 4.2.3 another measurement was performed using ions to probe the field. The equation for the free cyclotron frequency Eq. (2.1) can be used to determine the magnetic flux density  $B$  at a certain position in space. If these values are plotted against the axial position of the trap, the magnetic bottle term can be determined. If one divides the free cyclotron frequency of one ion species by its maximum, one can obtain  $B_2/|B|$  by a second-order polynomial fit in  $z$  because  $\omega_c$  is proportional to  $B(z)$ . The data are presented in Fig. 4.12. The free cyclotron frequency  $\omega_c$  was approximated by the sum frequency  $\omega_{\pm}$  and the whole beam tube was shifted in axial direction to measure different axial positions of the Penning trap.

The curvature of the quadratic fit in Fig. 4.12 was multiplied by the approximate maximum  $B$  field of

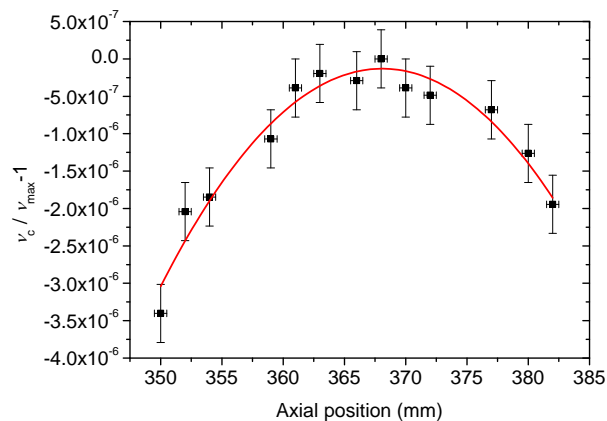


Fig. 4.12:  $B_2$  can be deduced from the frequency shift using equation Eq. (2.1). Therefore,  $\omega_+ + \omega_-$  is normalized to its maximum and plotted against the axial position  $z$ . The red curve is a quadratic fit in  $z$  to the data points. For this measurement, the centre of the Penning trap was moved in axial direction by moving the whole beam tube.

4.699 T. This leads to a value of  $-42(5) \text{ nT mm}^{-2}$  for  $B_2$ . This value is roughly equal to the value of  $-57.9(19) \text{ nT mm}^{-2}$  detected with the NMR probe in Section 4.2.3. These two values cannot be expected to be completely identical, as any material with a magnetic susceptibility different than air will change the field configuration. This does not only happen because of the different affinity for field lines, but also because currents are induced in the superconducting coils when any matter (e.g. the trap) enters their magnetic field.



## 5 Frequency ratio measurements

In order to determine the accuracy of mass measurements with the Penning traps, frequency ratio measurements have been carried out. This is of importance for KATRIN because the amounts of  ${}^3\text{He}^+$  and  $\text{T}^+$  must be determined separately to obtain an estimate on the systematic effects. To differentiate between the two, their frequencies have to be determined with an accuracy better than  $1 \times 10^{-4}$  and the resolution should be better than  $1 \times 10^4$  (i.e. no overlap between the Fourier peaks occurs). For the accuracy determination of the Penning trap, lithium was chosen because  ${}^6\text{Li}$  is a non-radioactive isobar of molecular tritium.  ${}^7\text{Li}^+$  serves as a second frequency probe to calculate the frequency ratio  $R$ . According to Eq. (2.1), the frequency ratio of the free cyclotron motion is equal to the mass ratio and can be compared to the one from literature. In principle, this scheme could be used for mass measurements of  ${}^6\text{Li}$  (whose mass is not as well known as the one of  ${}^7\text{Li}$ ), if the accuracy and precision of the KATRIN traps were high enough.

In this chapter, different frequency ratio measurements are presented and compared. Furthermore, the deviations from the ideal Penning trap are examined after a brief overview of the data acquisition.

### 5.1 Timing scheme and data acquisition

An exemplary timing scheme for the following experiments is displayed in Fig. 5.1. Initially, both endcaps are switched on and the first endcap is lowered for one millisecond to load the trap with ions. It is advantageous to introduce a small cooling period (6 ms) afterwards. This way ions with high oscillation amplitudes leave the trap and the remaining ions have approximately equal amplitudes. First, the more abundant ion species (93%  ${}^7\text{Li}^+$  to 7%  ${}^6\text{Li}^+$ ) is excited using a dipolar excitation at the modified cyclotron frequency. The sinusoidal excitation pulse is 4.1 ms (42 000 cycles) long and has a peak-to-peak amplitude of 4.5 V. Secondly, the less abundant ion species ( ${}^6\text{Li}^+$ ) is excited at its modified cyclotron frequency in dipolar mode for 3.5 ms (42 000 cycles) at 1.5 V.

Moreover, a short waiting time (50  $\mu\text{s}$ ) is inserted after the excitation, just before the detection as it is

shown in Fig. 5.1. This is done to limit the induced signal from the excitation on the detection electrodes. The induced current is recorded for 100 ms at a sampling rate of 42 MHz and stored on the computer. As the last step, the second endcap is lowered and all ions are ejected towards the Faraday cup where they are counted. This cycle repeats and the average of the stored waveforms is calculated. A Fast Fourier Transform (FFT) is applied after ten rounds. An example of such an FFT spectrum is shown in Fig. 5.2. The modified cyclotron frequency  $\nu_+$  can be determined with a dipolar detection scheme and the sum frequency  $\nu_+ + \nu_-$  is obtained from the quadrupolar detection scheme. A Gaussian is fitted to the  $\nu_+$  and  $\nu_+ + \nu_-$  peaks of  ${}^6\text{Li}^+$  and  ${}^7\text{Li}^+$ , respectively. Centre of the peak, its width, its height and the noise level are saved. If the fit does not work – for example because the signal-to-noise ratio of the amplitude is too low – the maximum from the spectrum is saved instead. As a last step, the voltage for dipolar excitation of either  ${}^6\text{Li}^+$  or  ${}^7\text{Li}^+$  is increased and the whole cycle restarted. If the maximum excitation voltage set on the utilised programme is reached, the cycle is restarted with the minimum excitation voltage. No magnetron excitation is applied because the ions are not trapped in the centre of the Penning trap which directly results in an initial magnetron (see Section 5.2.4).

A Matlab script reads the data files. For each excitation voltage this script calculates the average and standard deviation of the centre and amplitude of the fitted Gauss peak. If the fit did not work, the same was done for the maximum values instead. However, for these values the standard deviation was set to at least 5 Hz because of the bin size (for 100 ms detection time the bin width is 10 Hz, thus the error is half the bin size). An example for such a scan is displayed in Figs. 5.3 and 5.4 where the frequency and the Fourier amplitude are shown as a function of the excitation amplitude. Care has to be taken because all measurements are resulting in frequencies  $\nu$  instead of angular frequencies  $\omega$  which are used in the theoretical equations. A conversion can be done by dividing the angular frequency by  $2\pi$

$$\nu = \frac{\omega}{2\pi}. \quad (5.1)$$

Event	Duration	Timing scheme
First endcap (injection)	1.0 ms	
Dipolar excitation at $\nu_+$ for ${}^7\text{Li}^+$	4.1 ms	
Dipolar excitation at $\nu_+$ for ${}^6\text{Li}^+$	3.5 ms	
Detection	100 ms	
Second endcap (ejection)	1.0 ms	
Trapping time	$\approx 400$ ms	

Fig. 5.1: Typical timing scheme for lithium detection (not to scale). The first endcap is briefly lowered to load the trap. After a short cooling period  ${}^7\text{Li}^+$  and  ${}^6\text{Li}^+$  are excited consecutively. To minimize induced excitation signals a short waiting time is inserted before detection. At the end of one cycle the second endcap is lowered to eject the ions towards a Faraday cup. The trapping time could be lower but is limited by the computation time of the FFT.

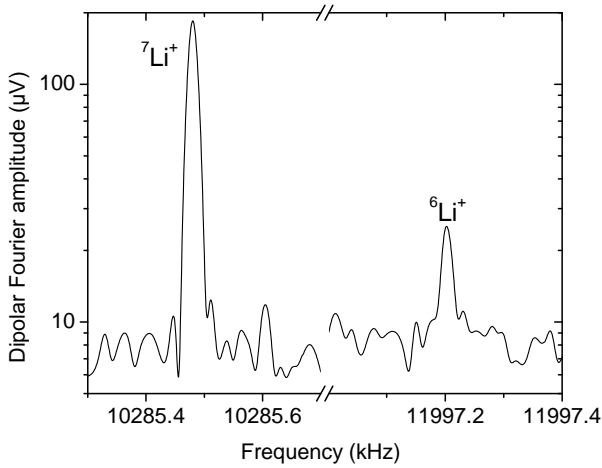


Fig. 5.2: Exemplary FT-ICR spectrum obtained by dipolar detection. The peak of the modified cyclotron frequency of  ${}^7\text{Li}^+$  (left) and  ${}^6\text{Li}^+$  (right) are clearly visible.

Figure 5.3 shows the expectation of a quadratic decrease of the Fourier frequency according to Eqs. (2.15) and (2.16). The error in the sum frequency decreases as the excitation voltage increases because the signal-to-noise ratio is increasing. Yet, the error of the modified cyclotron frequency remains nearly constant because a Gauss fit to the peak was not applicable and thus the resolution is limited to the bin size.

Theoretically, the amplitude of the modified cyclotron peak and the sideband peak at  $\nu_+ + \nu_-$  of Fig. 5.4 should increase linearly with the excitation voltage. The plateau above 1.5 V suggests that the ions lose their phase coherence or spread over a wider range of frequencies. This effect becomes even so prominent

above 3 V that the amplitudes decrease.

The FT-ICR programme scanned the  ${}^6\text{Li}^+$  excitation voltage from 0.05 to 6.00 V peak-to-peak in steps of 0.05 V while the  ${}^7\text{Li}^+$  voltage was kept constant and vice versa. The constant excitation voltage of  ${}^7\text{Li}^+$ , while scanning  ${}^6\text{Li}^+$ , is higher than the one of  ${}^6\text{Li}^+$  (4.5 to 1.5 V) as it has been observed that the signal-to-noise ratio of  ${}^6\text{Li}^+$  is enhanced if  ${}^7\text{Li}^+$  is excited to a higher radius.

To all amplitude scans a quadratic fit was applied. According to Eqs. (2.15) and (2.16), this is right for first order corrections, if one assumes that the modified cyclotron radius  $\rho_+$  increases linearly with the excitation amplitude  $V_{\text{exc}}$  (this is suggested by Eq. (2.36)). Each fit results in an unperturbed frequency  $\omega_0$  and a curvature  $K$  of the measured frequency  $\omega$  according to

$$\omega = \omega_0 + KV_{\text{exc}}^2 \quad (5.2)$$

$$\omega = \omega_0 + \frac{K}{A^2}\rho_+^2 \quad (5.3)$$

$$\text{using } \rho_+ = AV_{\text{exc}}. \quad (5.4)$$

For the sum frequency  $\omega_{\bar{c}} = \omega_+ + \omega_-$  and the modified cyclotron frequency  $\omega_+$  this means

$$\omega_+ = \omega_{+0} + K_+V_{\text{exc}}^2 \quad (5.5)$$

$$\omega_{\bar{c}} = \omega_{\bar{c}0} + K_{\bar{c}}V_{\text{exc}}^2. \quad (5.6)$$

Additionally, different trapping voltages (20 to 35 V in steps of 5 V) were examined. The combination of all these measurements has been used to determine trap imperfections, the radius of the stored ions and, of course, the accuracy of the set-up.

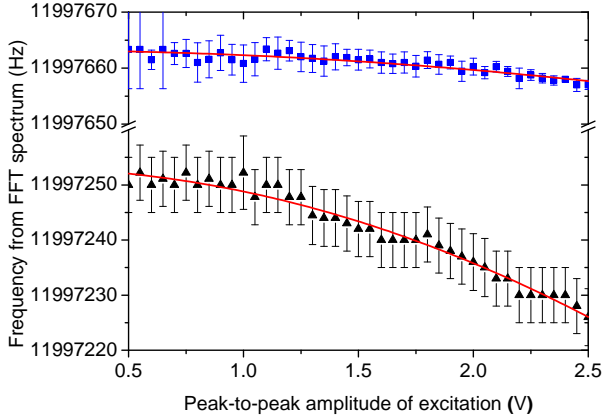


Fig. 5.3: Exemplary amplitude scan for  ${}^6\text{Li}^+$  at 35 V trapping voltage. Both the sum frequency  $\nu_+ + \nu_-$  (top) and the modified cyclotron frequency  $\nu_+$  (bottom) decrease with increasing excitation voltage. A quadratic frequency fit according to Eq. (5.2) is shown in red for each Fourier frequency because of the theoretic expectation from Eqs. (2.15) and (2.16).

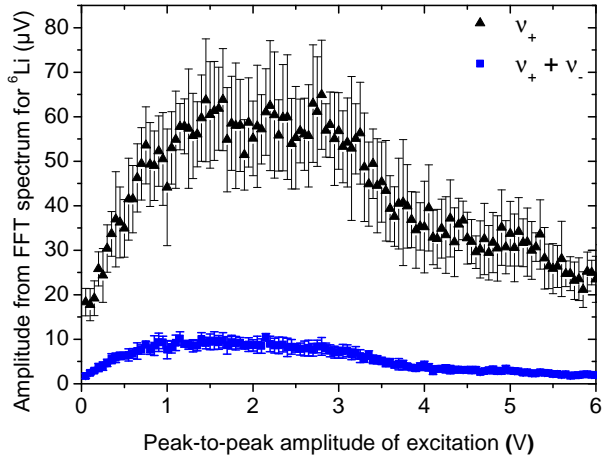


Fig. 5.4: Exemplary amplitude scan for  ${}^6\text{Li}^+$  at 35 V trapping voltage. Theoretically, the amplitude of the modified cyclotron peak (top) and the sideband peak at  $\nu_+ + \nu_-$  (bottom) should increase linearly with the excitation voltage until they hit the walls of the trap or leave the frequency range of the excitation pulse.

## 5.2 Trap imperfections

To determine the electrostatic imperfections and the magnetic bottle term, the radius of the ion cloud has to be known. The Eqs. (2.15) and (2.16) can be combined to calculate the modified cyclotron radius from the measured amplitude scans. However, no high accuracy should be expected as the results are limited by curvature of the sum frequency which is very low as shown in Fig. 5.3. For the calculation of the unperturbed frequencies it has been assumed that the magnetron radius vanishes. If one takes the values calculated in this chapter and Eqs. (2.15) and (2.16), this assumption adds a systematic error of approximately 5% on the magnetron frequency and  $5 \times 10^{-5} \%$  on the modified cyclotron frequency. These systematics are far below any statistical errors and can thus be safely ignored.

### 5.2.1 Extracting the modified cyclotron radius

The modified cyclotron radius  $\rho_+$  can be extracted from these measurements by comparing Eqs. (2.15) and (5.3) carefully. Using the curvature of the sum frequency  $K_{\bar{c}}$ , the proportionality factor  $A$  between excitation amplitude and ion radius can be calculated from

$$K_{\bar{c}} = \left[ -\frac{3}{2} \frac{C_4}{d^2} \omega_- - \frac{1}{2} \frac{\omega_+^3}{c^2} \right] A^2. \quad (5.7)$$

If one takes the difference of  $K_{\bar{c}}$  for  ${}^6\text{Li}^+$  and  ${}^7\text{Li}^+$  (denoted by the indices 6 and 7, respectively), the factor  $A$  can be obtained

$$K_{\bar{c}6} - K_{\bar{c}7} = -\frac{1}{2} \frac{1}{c^2} (\omega_{+06}^3 - \omega_{+07}^3) A^2 \quad (5.8)$$

$$\Rightarrow A^2 = -2c^2 \frac{K_{\bar{c}6} - K_{\bar{c}7}}{\omega_{+06}^3 - \omega_{+07}^3}. \quad (5.9)$$

Since a first order Taylor expansion of the magnetron frequency is independent of the ion mass, the difference of the curvature for the two ion species is governed by the well-known relativistic shift. This way  $A^2$  has been calculated in Table 5.1 using the two fit parameters of Eq. (5.2) for different trapping voltages. For this calculation, it was assumed that the effect of the magnetron radius and axial amplitude on the modified cyclotron and magnetron frequencies is negligible.

Unfortunately, the values had to be dismissed for the three lowest trapping voltages.  $A$  is a positive real number, so  $A^2$  should be greater than zero. If one takes the

$V_{\text{EC}}$ (V)	$A^2$ ( $10^{-7} \text{ m}^2 \text{ V}^{-2}$ )
20	$4 \pm 15$
25	$-7.2 \pm 9.4$
30	$-139 \pm 103$
35	$49 \pm 17$

Tab. 5.1:  $A^2$  for varying trapping voltages. As  $A$  is defined by  $\rho_+ = AV_{\text{EC}}$ , its square should be greater than zero. For all following calculations the value for 35 V is assumed. For details see text.

relative uncertainty into account as well, the measurement for 35 V trapping potential is the only one which gives a physically reasonable and significant value for  $A^2$ . For all further calculations  $A^2$  was assumed to be  $49(17) \times 10^{-7} \text{ m}^2 \text{ V}^{-2}$ . However, it should be noted that all values for  $A^2$  agree within two sigma. The reason why the results of this calculation have such a high error is obvious from Fig. 5.3: For all measurements, the curvature of the sum frequency  $K_{\bar{c}}$  is just at the border of being detectable and has a large uncertainty, so the difference of these two curvatures has a large relative error which limits the precision of  $A^2$ .

The value for  $A^2$  at 35 V trapping potential (see Table 5.1) corresponds to an  $A$  of  $2.2(13) \text{ mm V}^{-1}$ . This result is in a sensible range as the trap has a radius of 35 mm. Furthermore, it has been observed that the ion signal disappeared as the excitation amplitude approached its limit of 10 V peak-to-peak, so roughly at a radius of 2 cm. The reason is probably not that ions hit the walls of the trap, but rather that ions leave the homogeneous region and start to spread over a wide range of cyclotron frequencies because they start to see higher order terms of the electrostatic and magnetic field. Thus, they lose their phase coherence which causes a decrease of the induced current even well before an excitation amplitude of 10 V. The FFT signal decreases as seen in Fig. 5.4.

## 5.2.2 Electrostatic shifts

Once the motional radius of the lithium ions is known, all trap imperfections can be calculated from the data. Using Eq. (5.7), the electrostatic imperfections  $C_4/d^2$  can be calculated

$$\frac{C_4}{d^2} = -\frac{2}{3} \left( \frac{K_{\bar{c}}}{A^2} + \frac{1}{2} \frac{\omega_{+0}^3}{c^2} \right) \frac{1}{\omega_{\bar{c}0} - \omega_{+0}}. \quad (5.10)$$

The magnitude of the magnetron frequency is estimated by the expression  $\omega_{\bar{c}0} = \omega_{-0} + \omega_{+0}$ .

The electrostatic imperfections have been calculated for  ${}^6\text{Li}^+$  and  ${}^7\text{Li}^+$  at trapping voltages from 20 to 35 V in steps of 5 V. To obtain an error on  $C_4/d^2$ , the errors on  $A^2$  and on the fit values have been considered. As these are not independent of each other, a maximum uncertainty propagation has been used instead of the Gaussian method.  $C_4/d^2$  was found to be  $-5.6(23) \times 10^2 \text{ m}^{-2}$ . This value is in accordance with a finite element study and analytical calculations for the KATRIN trap that will be presented in [Hec12].

As the geometry parameter  $d$  of the trap has been measured to be  $34.3(2) \text{ mm}$  (see [UD11, p. 62]), the  $C_4$  coefficient is  $-0.66(27) \times 10^{-4}$ . Stahl-Electronics chose the lengths of the electrodes in such a way that  $C_4$  nearly vanished in their simulations, so the experimental results confirm their effort.

## 5.2.3 Shifts from the magnetic bottle

Using Eq. (2.15) for  $\Delta\omega_+$  the ratio  $B_2/|B|$  can be calculated from the curvature of the modified cyclotron frequency given in Eq. (5.3)

$$K_+ = \left[ \frac{3}{2} \frac{C_4}{d^2} (\omega_{\bar{c}0} - \omega_{+0}) - \frac{1}{2} \frac{B_2}{|B|} \omega_{+0} - \frac{1}{2} \frac{\omega_{+0}^3}{c^2} \right] A^2 \quad (5.11)$$

$$\frac{B_2}{|B|} = -2 \frac{K_+}{\omega_{+0} A^2} - \frac{\omega_{+0}^2}{c^2} + 3 \frac{C_4}{d^2} \frac{\omega_{\bar{c}0} - \omega_{+0}}{\omega_{+0}}. \quad (5.12)$$

This was done for all scans: for both lithium isotopes and for the four trapping voltages. The mean value was calculated and the same error calculation technique was applied as in Section 5.2.2. This leads to a value of  $1.3(32) \times 10^2 \text{ nT mm}^{-2}$  for  $B_2$  (assuming  $|B|$  is 4.699 T). If one compares the result with the one of Section 4.2.5 ( $B_2 = -42(5) \text{ nT mm}^{-2}$ ), the two values agree within  $0.5 \sigma$  due to the large error of this section's method. The reason for the error is that  $B_2/|B|$  is derived from the values of  $K_+$ ,  $A^2$  and  $C_4/d^2$  which have a large relative error. Because  $B_2/|B|$  is calculated from the same data as the other values these errors are not independent.

## 5.2.4 Extracting the magnetron radius

As mentioned in Section 5.1, there is an initial magnetron radius when the ions are trapped. Since the magnetron radius causes a certain frequency shift, it is important for systematic error calculation to have an

$V_{\text{EC}}(\text{V})$	$\Delta v_{\tilde{c}0}(V_{\text{EC}})$ (Hz)	
	for ${}^7\text{Li}^+$	for ${}^6\text{Li}^+$
20	$-234.6 \pm 0.6$	$-264.2 \pm 0.3$
25	$-299.1 \pm 0.3$	$-317.7 \pm 0.3$
30	$-354.6 \pm 1.7$	$-383.7 \pm 0.3$
35	$-410.3 \pm 0.5$	$-447.2 \pm 0.5$

Tab. 5.2:  $\Delta v_{\tilde{c}0}(V_{\text{EC}})$  for different trapping voltages and both lithium isotopes according to Eq. (5.13). As expected the shift decreases with decreasing voltage.

estimate on its magnitude. Additionally, one gets an estimate where the ions are trapped radially.

There are two ways that were exploited to extract the magnetron radius  $\rho_-$ . Without any additional measurements, one can extrapolate the sum frequencies at  $\rho_+ = 0$  mm to 0 V trapping potential. Equation (2.16) leads to a deviation of the sum frequency  $\Delta\omega_{\tilde{c}0}(V_{\text{EC}})$  given by

$$\Delta\omega_{\tilde{c}0}(V_{\text{EC}}) = \omega_{\tilde{c}0}(V_{\text{EC}}) - \omega_{\tilde{c}0}(0\text{V}) \quad (5.13)$$

$$\Delta\omega_{\tilde{c}0}(V_{\text{EC}}) = \overbrace{\frac{1}{2} \frac{B_2}{|B|} (\rho_z^2 - \rho_-^2) \omega_{+0}}^{\text{const for } V_{\text{EC}}} + \underbrace{-\frac{1}{2c^2} \rho_z^2 \omega_{-0} \omega_{+0}^2}_{\approx \rho_z^2 \times 80 \text{ rad s}^{-1} \text{ m}^{-2}} + \frac{3}{2} \frac{C_4}{d^2} \rho_- \omega_{-0} \quad (5.14)$$

$$\rho_-^2 \approx \frac{\Delta\omega_{\tilde{c}0}}{\frac{3}{2} \frac{C_4}{d^2} \omega_{-0}}. \quad (5.15)$$

The values for  $\Delta\omega_{\tilde{c}0}(V_{\text{EC}})$  were calculated from an extrapolation of  $\omega_{\tilde{c}0}(V_{\text{EC}})$  to 0 V and then taking the difference according to Eq. (5.13). They are shown in Table 5.2. The effect of  $\rho_z$  on  $\Delta\omega_{\tilde{c}0}(V_{\text{EC}})$  can be safely ignored as the term is approximately  $0.8 \text{ rad s}^{-1}$  (0.1 Hz) for an axial amplitude of 10 mm. This is well below the detection limit displayed in Table 5.2. The difference between the frequencies of  ${}^6\text{Li}^+$  and  ${}^7\text{Li}^+$  cannot be assigned to the uncertainty of the frequency shift. A possible explanation is that both isotopes see a slightly different  $C_4$ . This happens, if the ion cloud is dense enough for Coulomb interaction to play a role.  ${}^7\text{Li}^+$  is twelve times more abundant than  ${}^6\text{Li}^+$  and the excitation separates the two isotopes, so its effective  $C_4$  is expected to be different from  ${}^6\text{Li}^+$  because the ions create their own electrostatic field. Depending on the size of the cloud, this changes the electrostatic potential and thus the effective  $C$  coefficients seen by

the ions. Yet, the error on  $C_4/d^2$  is so large that this error in frequency does not make a difference to the final magnetron radius. All in all, this leads to a value of 12(10) mm for  $\rho_-$ .

The initial magnetron radius occurs without any excitation because the ions are not trapped in the centre of the Penning trap. The reason for this is most probably the shift of the  $B$  field observed in Fig. 4.9. The magnetic field lines force the ions to a high initial magnetron radius. This could be compensated by moving the set-up relative to the magnet. However, there is not sufficient space to fully compensate the effect and it has been seen that the FFT signal was lost when the vacuum tube was moved too far. The disappearance of the signal has not been fully understood. A possible explanation would be that by moving the beam tube, the ions are created at a different magnetic field line. Only field lines parallel to the velocity of the ions enable particles to enter the homogeneous region of the magnet. If they start with too much cyclotron energy, the magnetic mirror simply reflects all ions. This and the limited space for moving the tube in the bore of the magnet might make it very hard to trap ions without any initial magnetron motion.

To determine the magnetron radius more accurately a second method has been used that relies on quadrupolar conversion profiles. These profiles have been recorded as part of the frequency ratio determination scheme in Section 5.3.4. The main idea is to use a quadrupolar field to convert all initial magnetron motion to modified cyclotron motion. Then the modified cyclotron FFT amplitude is recorded while scanning the frequency of the quadrupolar excitation field. This way  $\omega_{\tilde{c}}$  can be obtained according to Eq. (2.25).

The sum frequencies obtained from the FFT spectrum after a dipolar excitation  $\omega_{\tilde{c}0}$  and from the quadrupolar conversion profiles  $\omega_{\tilde{c}Q}$  were compared. Because it is known which frequency shift corresponds to which cyclotron amplitude from Section 5.2.1, these two values can be used to determine the cyclotron radius after the quadrupolar conversion pulse. This radius is equal to the magnetron radius because all initial magnetron quanta have been converted to cyclotron quanta (see Eq. (2.25)). Using Eq. (2.16) the following equation can be obtained

$$\omega_{\tilde{c}0} - \omega_{\tilde{c}Q} = \Delta\omega_{\tilde{c}} \Big|_{\rho_+=0} - \Delta\omega_{\tilde{c}} \Big|_{\rho_-=0, \rho_+=\rho_-} \quad (5.16)$$

$$= \left( -\frac{1}{2} \omega_{+0} \frac{B_2}{|B|} + 3 \frac{C_4}{d^2} \omega_{-0} + \frac{1}{2} \frac{\omega_{+0}^3}{c^2} \right) \rho_-^2 \quad (5.17)$$

$$\rho_-^2 = \frac{\omega_{\tilde{c}0} - \omega_{\tilde{c}Q}}{-\frac{1}{2}\omega_{+0}\frac{B_2}{|B|} + 3\frac{C_4}{d^2}\omega_{-0} + \frac{1}{2}\frac{\omega_{+0}^3}{c^2}}. \quad (5.18)$$

For  $\omega_{\tilde{c}0}$  the extrapolated fit values were used and for  $\omega_{\tilde{c}Q}$  the values for the sum frequency of  ${}^7\text{Li}^+$  from Section 5.3.4 were taken. The quadrupolar conversion profiles of  ${}^6\text{Li}^+$  were not considered due to their very poor quality (for a discussion see Section 5.3.4). As a result, the magnetron radius was determined to be 4(4) mm. This is in accord with the magnetron radius calculated using the first method. The error on the result is dominated by the error on  $C_4/d^2$ . Getting better estimates on  $\rho_-$  with the current set-up will not be easy because the sum frequency of the less abundant  ${}^6\text{Li}^+$  has to be detected. This requires a high amount of trapped ions which changes the effective  $C_4$  seen by the ion cloud.

### 5.2.5 Misalignment of fields

A misalignment of the electrostatic and magnetic field causes a magnetron dependent frequency shift  $\Delta\nu$  according to Eq. (2.20). The beam tube is typically aligned to the ion trap by less than one degree. The magnetic field has to be aligned to the beam tube by a few degrees as the ions would be reflected by the magnetic mirror otherwise. A direct measurement of this misalignment is nearly impossible as any probe (Hall, NMR, . . .) distorts the magnetic and electric field too much. However, using Eq. (2.20) the influence of such a frequency shift can be calculated and added as a systematic error to all accuracy measurements. As the shift is equal for  ${}^6\text{Li}$  and  ${}^7\text{Li}$  the influence on the frequency ratio can be calculated by

$$R = \frac{\nu_{\tilde{c}07} + \Delta\nu}{\nu_{\tilde{c}06} + \Delta\nu} \quad (5.19)$$

$$\Rightarrow \Delta R = \left| \frac{\nu_{\tilde{c}07} - \nu_{\tilde{c}06}}{\nu_{\tilde{c}06}^2} \Delta\nu \right|. \quad (5.20)$$

A quite large misalignment of  $5^\circ$  has been assumed in this study because the magnetic field shows the anomalous shape of Fig. 4.9. This leads to a systematic uncertainty of  $7 \times 10^{-8}$ .

### 5.2.6 Image charges

The image charge force plays a substantial role when the particles are close to the electrodes [VDMFS89]. However, 100 000 ions and a trap radius of 35 mm together with Eq. (2.22) give a shift of only 0.04 Hz. Compared to the shifts from misalignment, which are

in the order of 5 Hz, this systematic effect is negligible. Of course, a revolution radius of approximately 10 mm is not negligible compared to the trap radius, so strictly speaking the prerequisites of Eq. (2.22) do not hold in this case. But even a twenty-five fold shift of 1 Hz will only contribute  $1 \times 10^{-8}$  to the systematic uncertainty of the mass ratio. For this reason, systematic effects due to image charges are not considered to contribute to the overall uncertainty.

The Coulomb interaction studies of Section 5.4 support this claim. If there was an image charge shift, it should scale linearly with the number of ions. Currently, there is no significant evidence in our experiment for such a shift. An exemplary amplitude scan with different ion numbers is shown in Fig. 5.5. Between 0.2 and 0.5 V excitation voltage a deviation between the different ion numbers can be seen. However, this could not be reproduced at a later stage and is most probably a deviation due to fluctuations in the power supplies or the changing surface potential of the ion optics of the source because of the deposited lithium.

## 5.3 Comparison of different mass ratio determination methods

There are numerous methods to determine the mass of an ion with the FT-ICR method. The most common ones shall be compared regarding their accuracy in the following sections.

### 5.3.1 Conventional method

The conventional method is most commonly used in commercial broadband FT-ICR set-ups and will also be the main detection mode for KATRIN. A dipolar excitation at  $\nu_+$  is used to increase the modified cyclotron radius. Then the modified cyclotron frequency  $\nu_+$  is detected in dipolar mode for several trapping voltages. For a maximum accuracy, the detected frequency is extrapolated to 0 V trapping potential where it is equal to the free cyclotron frequency. As the latter is proportional to the ion's mass, the ratio of two modified cyclotron frequencies can be used to determine the accuracy. For a typical mass measurement the second frequency would be a reference ion with a very low uncertainty in its mass value. For mass spectroscopy it is usually sufficient to approximate the free cyclotron by the modified cyclotron frequency to identify all constituents. According to Eq. (5.19) the frequency ratio  $R$



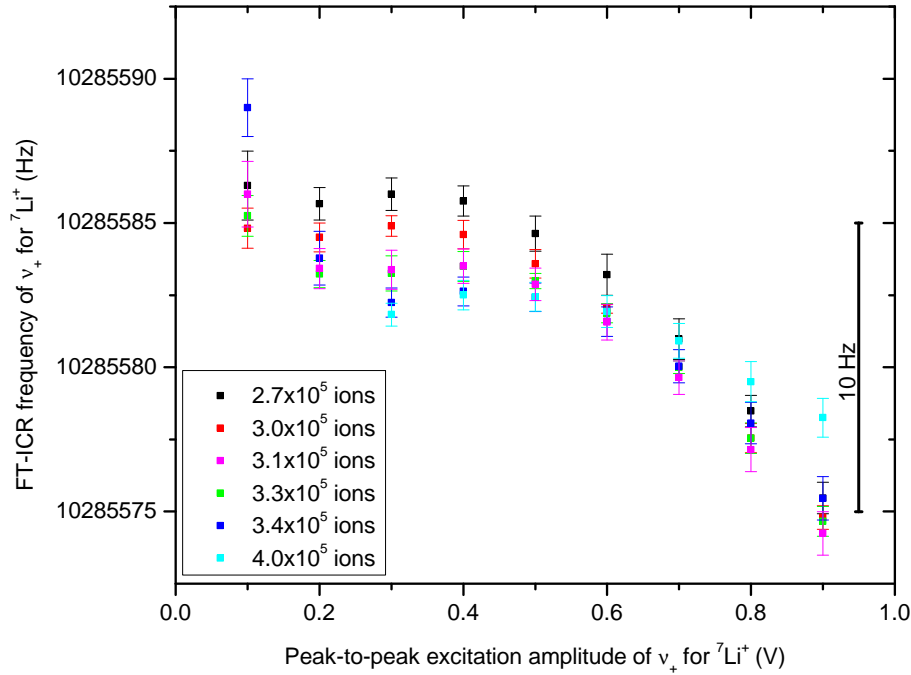


Fig. 5.5: The effect of different ion numbers on the frequency from the FFT for  ${}^7\text{Li}^+$ . If an image charge effect was present, it should scale linearly with the number of ions. The deviation between 0.2 and 0.5 V excitation amplitude could not be reproduced. The scan took a couple of hours for each ion number, so most probably the deviation is due to fluctuations in the power supplies or the changing surface potential of the ion optics of the source because of the deposited lithium. Another measurement should be performed to investigate whether this effect was a statistical fluctuation or is an image charge effect.

is given by

$$R = \frac{\nu_{+07}}{\nu_{+06}} \approx \frac{m_{6\text{Li}^+}}{m_{7\text{Li}^+}}. \quad (5.21)$$

In the case of 0V trapping potential, the frequency ratio  $R$  is exactly equal to the mass ratio of the ions (see Eq. (2.5)). Depending on the accuracy of the spectrometer, the atomic mass has to be corrected by the missing electron mass and binding energy. For the KATRIN traps it is sufficient to take the electron mass into account. According to [NFS<sup>+</sup>06], the  $R$  value for lithium is given by

$$R_{\text{lit}} = 0.857\,332\,053\,6(86). \quad (5.22)$$

Figure 5.6 shows the results for the difference of the experimental frequency ratio and the literature value for  $m_{6\text{Li}^+}/m_{7\text{Li}^+}$ . With increasing trapping potential the deviation increases. This is due to the influence of the magnetron frequency which is neglected in the approximation  $\omega_+ \approx \omega_c$ . By extrapolating the modified cyclotron frequencies of both ion species to 0V and

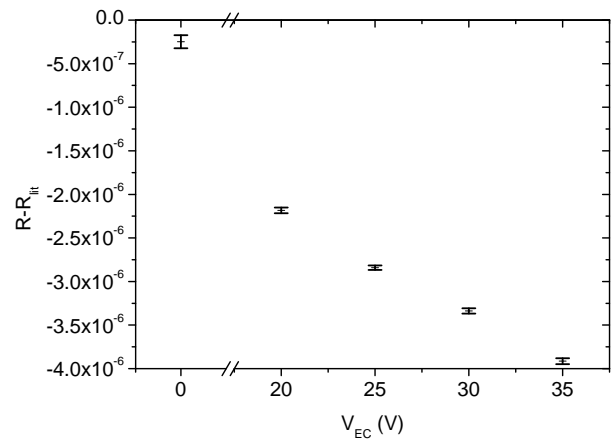


Fig. 5.6: The difference of  $R = \nu_{+07}/\nu_{+06}$  from the literature value as a function of the trapping voltage for the conventional mass determination method. Only the statistical errors are plotted. As expected, the values for a non-vanishing trapping potential are far from the literature value whereas the extrapolated value at 0V is quite close to the expectation.

then taking the frequency ratio, a deviation from the literature value of  $-2.48(74) \times 10^{-7}$  is reached. Since only statistical errors have been considered so far, the systematic influences of misalignment ( $5 \times 10^{-8}$ ) and the error from the remaining magnetron and axial motion have to be added. The shift from magnetron and axial motion can be estimated by using  $B_2/|B|$  calculated in Section 4.2.5 and Eq. (2.15). All frequencies are extrapolated to 0V; so the magnetron frequency is extrapolated to  $\nu_- = 0$ Hz. This means that only the uncertainty originating from  $B_2/|B|$  plays a role. But as this error is proportional to  $\omega_+$  it is not important for the frequency ratio  $R$  of Eq. (5.21):

$$\Delta R = \frac{\omega_{+07} + \frac{1}{2} \frac{B_2}{|B|} \omega_{+07} (z^2 - \rho_-^2)}{\omega_{+06} + \frac{1}{2} \frac{B_2}{|B|} \omega_{+06} (z^2 - \rho_-^2)} - R \quad (5.23)$$

$$= 0. \quad (5.24)$$

Altogether, this results in a deviation of  $-2.5(7)_{\text{stat}}(7)_{\text{sys}} \times 10^{-7}$  from the literature value. As zero is within two sigma of this value, the value measured here is still in accordance with the literature value. However, to be sure that no further systematic shift plays a role, this measurement should be repeated. All older measurements cannot be used for comparison since they are either lacking the  ${}^6\text{Li}^+$  amplitude scans or the scan of the trapping potential.

### 5.3.2 Sideband measurement using the quadrupolar detection

With the quadrupolar detection mode the high frequency magnetron sideband of the modified cyclotron motion can be detected. This sideband lies at  $\nu_+ + \nu_-$  which is a very good approximation for the free cyclotron frequency. Thanks to the initial magnetron motion, the same excitation scheme as in Fig. 5.1 was used without the need to do an additional excitation at the magnetron frequency  $\nu_-$ . Hence, the frequency ratio  $R$  is given by

$$R = \frac{\nu_{\tilde{c}07}}{\nu_{\tilde{c}06}}. \quad (5.25)$$

To achieve the best accuracy, the frequencies (which were recorded for 20, 25, 30 and 35 V trapping voltage) were extrapolated to 0V trapping potential and then  $R$  was calculated as illustrated in Fig. 5.7. Considering only statistical errors, this led to a deviation of  $-5(11) \times 10^{-7}$  from the literature value of  $R$ . The error from the magnetron and axial oscillation can be neglected because there is no  $B_2/|B|$  shift on  $\omega_{\tilde{c}}$

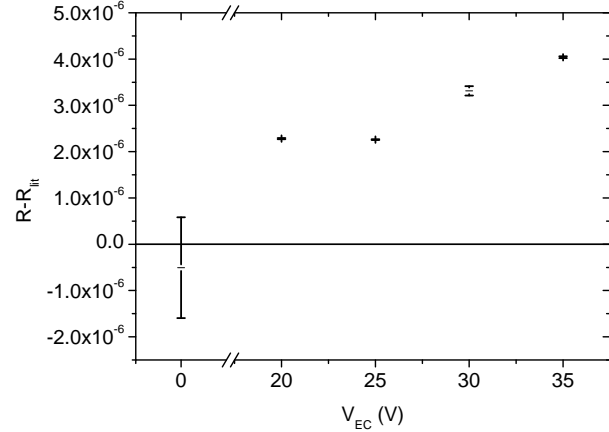


Fig. 5.7: Deviation of the frequency ratio of lithium for pure sideband detection from the mass ratio literature value for different trapping voltages. With increasing trapping potential the deviation from the literature values increases because of electrostatic and misalignment frequency shifts that are proportional to the magnetron frequency. Only statistical errors on the frequencies are shown.

(see Equation (2.16)) and the magnetron frequency is extrapolated to 0 Hz. Of course, the effects due to misalignment have to be taken into account which results in a deviation from the literature value of  $-5(11)_{\text{stat}}(1)_{\text{sys}} \times 10^{-7}$  for the mass ratio. This is well compatible with the expectation of 0 due to the statistical uncertainty which is quite high because the quadrupolar signal of  ${}^6\text{Li}^+$  has a very low signal-to-noise ratio.

### 5.3.3 Sideband measurement using the dipolar and quadrupolar detection

A new scheme has been invented that does not depend on the detection of the sum frequency of  ${}^6\text{Li}^+$  because this sum frequency has a poor signal-to-noise ratio and is not easy to detect. The idea is to use the dipole detection for  ${}^6\text{Li}^+$  and  ${}^7\text{Li}^+$ , but the quadrupolar detection for  ${}^7\text{Li}^+$  only. The magnetron frequency can be calculated from the sum and the modified cyclotron frequencies of  ${}^7\text{Li}^+$  ( $\omega_- \approx \omega_{\tilde{c}} - \omega_+$ ) and is used to estimate the sum frequency of  ${}^6\text{Li}^+$ . Hence, the frequency

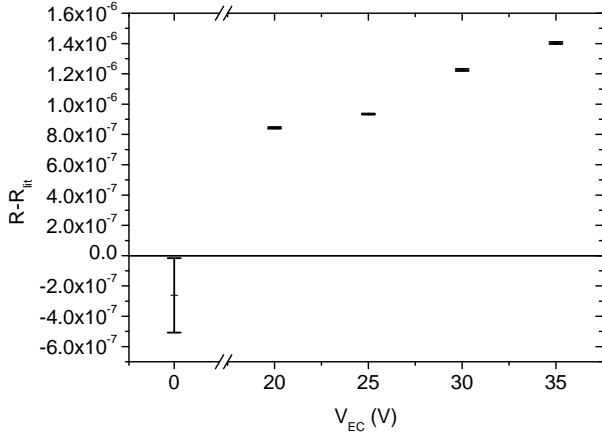


Fig. 5.8: Deviation of the frequency ratio of lithium (calculated from  $\nu_{+06}$ ,  $\nu_{+07}$  and  $\nu_{\bar{c}07}$  according to Eq. (5.27)) from the mass ratio literature value for different trapping voltages. With increasing trapping potential the deviation from the literature values increases because of electrostatic and misalignment frequency shifts that are proportional to the magnetron frequency. Only statistical errors on the frequencies are shown; note that they are hardly visible for the values at 20, 25, 30 and 35 V.

ratio  $R$  is calculated by

$$R = \frac{\nu_{\bar{c}07}}{\nu_{+06} + \nu_{-0}} \quad (5.26)$$

$$= \frac{\nu_{\bar{c}07}}{\nu_{+06} + \nu_{\bar{c}07} - \nu_{+07}}. \quad (5.27)$$

Figure 5.8 displays the results for the four measured trapping voltages and for the extrapolated frequencies. Compared to Fig. 5.6 the deviation from the literature value for a given trapping voltage were reduced by a factor of three. The value for  $R$  at 0 V trapping potential including statistical errors is  $-2.6(25) \times 10^{-7}$ . The systematic shift from the misalignment has to be added which results in a value of  $-2.6(25)_{\text{stat}}(7)_{\text{sys}} \times 10^{-7}$ . Considering its error bar this value agrees very well with the literature value. Moreover, the precision is improved by a factor of four compared to the value of Section 5.3.2 ( $3 \times 10^{-7}$  vs.  $12 \times 10^{-7}$ ).

### 5.3.4 Quadrupolar conversion profiles

The quadrupolar conversion profile is a fundamentally different method for mass measurements. In principle the same scheme as in Fig. 5.1 is used but only one ion

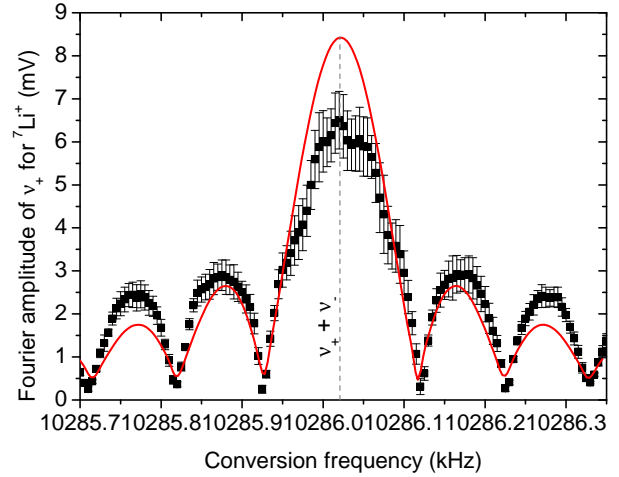


Fig. 5.9: Conversion profile of  ${}^7\text{Li}^+$  using a quadrupolar excitation at varying frequencies and 35 V trapping potential. The amplitude of the modified cyclotron motion is plotted against the excitation frequency. A nonlinear fit given by Eq. (2.25) is shown in red. The poor match between data and theory might be because of screening effects where the outer ions shield the inner ions of the cloud. This shielding should be more effective close to the resonance frequency of the ions. Thus the amplitude of the main peak is lowered.

species is excited. Another difference is the use of a quadrupolar instead of a dipolar excitation geometry. Only the modified cyclotron motion is detected and the height of the peak in the FFT spectrum is recorded. The quadrupolar excitation has the ability to couple magnetron and cyclotron motion. Thus, the initial magnetron radius can be fully converted to a pure cyclotron motion.

For 20, 25, 30 and 35 V trapping voltage a frequency scan covering 1000 Hz in steps of 5 Hz around the sum frequency  $\omega_c$  was performed. For each lithium isotope and each trapping voltage, the excitation amplitude was chosen so that the amplitude of the modified cyclotron peak in the FFT spectrum became maximal. This should be equal to a full conversion from magnetron to cyclotron radius. The number of cycles of the sinusoidal pulse was fixed to 100 000 (so approximately 8.6 ms for  ${}^6\text{Li}^+$  and 9.7 ms for  ${}^7\text{Li}^+$ ) which resulted in peak-to-peak amplitudes of approximately 1 V.

Figure 5.9 shows such a quadrupolar conversion profile for  ${}^7\text{Li}^+$ . The theoretical shape is given by Eq. (2.25) and is basically the magnitude of a sinus cardinalis with its centre at the sum frequency  $\nu_+ + \nu_-$ . This way the

radial sum frequency  $\omega_{eQ}$  can be obtained by a fit. The values for different trapping potentials are shown in Table 5.3. Thus, the mass ratio is calculated by

$$R = \frac{\nu_{eQ7}}{\nu_{eQ6}}. \quad (5.28)$$

A conversion profile for  ${}^6\text{Li}^+$  is shown in Figure 5.10. The difficulty of this frequency ratio method is directly obvious from the plot: There is only one low frequency sideband and the main peak visible. This limits the precision of the frequency determination because the fit region is quite small. A similar effect like the missing part of the spectrum is seen in a simulation performed by Simon van Gorp in [VG12] which shows that high frequency sidebands get suppressed, if one tries to excite a less abundant ion species of an ion cloud. For low frequencies this effect does not appear. It was not seen either, if the Coulomb interaction in the simulation was turned off. In the simulations of van Gorp this effect disappears, if less ions are stored in the trap. However, we could not verify this claim because we are limited by the sensitivity of the detection system. On the low frequency side of the main peak, only the first sideband is observed because the signal-to-noise ratio is too low.

Figure 5.11 illustrates how the mass ratio depends on the trapping voltage. Unexpectedly, the value that is extrapolated to 0V does not give the best accuracy. This is because the statistical error on the sum frequency of  ${}^6\text{Li}^+$  and  ${}^7\text{Li}^+$  is an order of magnitude larger than the uncertainty of the extrapolated modified cyclotron frequency in the other methods as shown in

$V_{EC}$ (V)	$\nu_+ + \nu_-$ (Hz)	
	for ${}^6\text{Li}^+$	for ${}^7\text{Li}^+$
20	$11\,997\,724.6 \pm 0.9$	$10\,286\,034.3 \pm 1.0$
25	$11\,997\,719.8 \pm 1.1$	$10\,286\,030.0 \pm 0.8$
30	$11\,997\,719.1 \pm 0.9$	$10\,286\,019.8 \pm 0.8$
35	$11\,997\,710.2 \pm 0.8$	$10\,286\,018.9 \pm 0.7$
0	$11\,997\,743.5 \pm 2.2$	$10\,286\,056.1 \pm 2.1$

Tab. 5.3: Sum frequencies ( $\nu_+ + \nu_-$ ) of  ${}^6\text{Li}^+$  and  ${}^7\text{Li}^+$  for different trapping voltages  $V_{EC}$  taken from the quadrupolar conversion profiles. The statistical error on the frequency which is shown in this table is a factor three larger than for the frequency determination from the FFT spectrum. The value for 0V trapping potential is extrapolated from the other measurements.

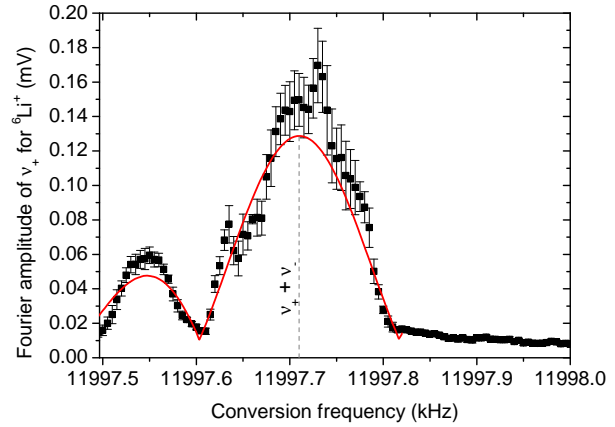


Fig. 5.10: Conversion profile of  ${}^6\text{Li}^+$  using a quadrupolar excitation at varying frequencies and 35V trapping potential. The amplitude of the modified cyclotron motion is plotted against the excitation frequency. A nonlinear fit given by Eq. (2.25) is shown in red.  ${}^7\text{Li}^+$  is not excited and there are no high frequency sidebands visible for  ${}^6\text{Li}^+$ . This is similar to a simulation presented in [VG12] where high frequency sidebands were suppressed by the Coulomb interaction between two ion species.

Table 5.3. This could be enhanced by choosing longer excitation pulses which result in sharper conversion peaks according to equation Eq. (2.25). However, due to Coulomb interaction and rest gas molecules, the coherence time is limited to approximately 20 ms at  $1 \times 10^{-7}$  mbar [UD11, p. 65]. Another source of statistical errors is that only one sideband (the first on the low frequency side of the main peak) is visible for  ${}^6\text{Li}^+$  because of the low signal amplitude and most probably Coulomb screening. This Coulomb effect has not yet been fully understood, but was observed in a similar simulation performed by Gorp in [VG12].

The extrapolation of the frequencies to 0V trapping potential leads to a value of  $5.0(24) \times 10^{-7}$  including only statistical errors for the deviation of  $R$  from its literature value. When one takes the misalignment into account, this changes to  $5.0(25)_{\text{stat}}(7)_{\text{sys}} \times 10^{-7}$ . This value is within two sigma of the literature value and well in accordance with the other methods introduced so far.

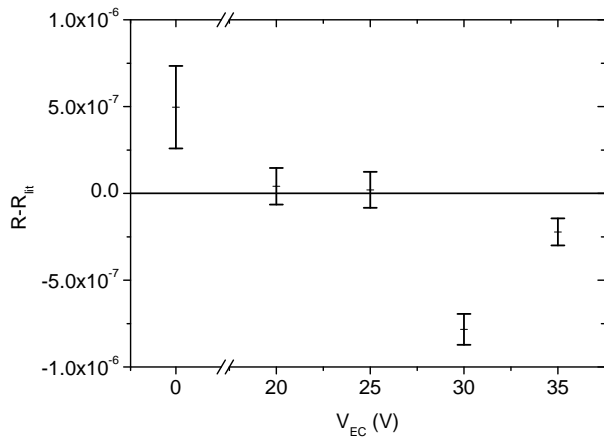


Fig. 5.11: Deviation of the frequency ratio of quadrupolar conversion profiles from the mass literature value versus different trapping voltages including the extrapolation to 0V trapping potential. The error bars arise from statistical effects only. Contrary to expectation the extrapolated value gives not the best accuracy, because there is no general trend with increasing trapping potential visible. The statistical error for 0 V is the largest, because of the extrapolation. This is similar to the behaviour in Figs. 5.6 to 5.8. For details see text.

### 5.3.5 Discussion and comparison of the four methods

If one compares all the different mass determination methods, one directly sees that the differences are marginal. In general, all methods are approximately equal. However, if one faces a specific problem it might be worthwhile to look into a certain mass measurement scheme. The best overall accuracy and precision was reached with the dipolar detection extrapolated to 0V trapping potential. This is probably due to the fact that for dipolar detection the largest signal amplitudes are measured. Of course, this greatly enhances the signal-to-noise ratio and thus the frequency can be determined with a high precision using a Gaussian fit to the respective peaks.

To limit the effect of the electrostatic field usually trapping potentials of 1 V or less are chosen. However, due to the high ion energy this is neither possible for this set-up nor for KATRIN. Correction electrodes would reduce the  $C_4$  shift and make an extrapolation more reliable. A cleaning of contaminants ( ${}^7\text{Li}^+$  in our case) has the ability to greatly enhance the signal amplitudes

which reduces the statistical error that dominated the uncertainties of most measurements.

If an extrapolation to 0V is not feasible, it is advantageous to choose one of the quadrupolar (detection or excitation) methods. The difference between quadrupolar and dipolar detection is even bigger, if one has a way of limiting the initial magnetron and axial oscillations which contribute partly to the shift in the mass ratio for a given voltage. Usually, it is better to choose the ‘sideband measurement using dipolar and quadrupolar detection’ method over the ‘sideband measurement using the quadrupolar detection’ method. Both, accuracy and precision, are better, if one dismisses the quadrupolar signal of the less abundant ion. However, this is not the case, if both ions have approximately the same abundance. Then estimating the magnetron frequency gives no advantage as both signals are about equal in amplitude.

If one cannot suppress the initial magnetron motion, the quadrupolar conversion method has the potential to reach the highest precision. This is simply due to the fact that no further energy is transferred to the ion so errors from frequency shifts remain low. However, this method is in our case limited by the vacuum and the Coulomb interaction of the ions which both decrease the coherence time of the motion. The comparison of Figs. 5.6 to 5.8 with Fig. 5.11 clearly shows the least influence of the trapping potential on the frequency ratio for the detection method of Section 5.3.4. The initial magnetron radius could not be suppressed in our experiment because the magnetic field was bent as shown in Fig. 4.9. The low energetic ions follow the magnetic field lines. This behaviour causes them to be trapped off-centre. Hence an initial magnetron motion can be detected.

In general, the accuracy  $(R - R_{lit})/R_{lit}$  and precision  $\Delta R/R$  of the trap were calculated to be  $3 \times 10^{-7}$  and  $2 \times 10^{-7}$ , respectively, varying slightly with the detection method. This value could be further enhanced by controlling the initial magnetron motion and by lowering the energy of the ions to enable lower trapping voltages. Another main source for shifts is the Coulomb screening:  ${}^6\text{Li}^+$  could only be observed in dipolar excitation, if  ${}^7\text{Li}^+$  was excited to a higher modified cyclotron radius first. To look further into this effect, a gas ionisation source will be used in future experiments which allows to set the ratio of the ion species to arbitrary values. Thus, the influence of the total number of ions and the ratio of the ion species can be detected independently. However, this will only work for gaseous samples, so the effect on lithium has to be approximated by gasses of similar mass (e.g. helium).

## 5.4 Coulomb interaction studies

Another experiment using the frequency ratio determination method of Section 5.3.3 was performed to investigate the effect of different ion numbers on the frequency ratio. In addition to the frequencies, the number of ions was recorded. For this purpose the Quick Charge amplifier (QCP) and Faraday cup were used as an ion counter as it is described in Section 3.5.2. The number of trapped particles was changed by varying the voltage applied to the exit disc of the source. This value should not alter the shape of the ion beam severely, especially as it was only changed by thirty-three per cent.

To verify the detected ion numbers, one can have a look at the Fourier amplitude of the modified cyclotron frequency for varying ion numbers. This is shown in Fig. 5.12. The expectation is to see a proportionality between the area of the FFT peak and the number of trapped particles. This should be roughly equal to a proportionality between FFT amplitude and ion number since the bin width of the discrete FFT is larger than the width of the Fourier peak. However, the plot does not meet the expectation too well since the extrapolation to an FFT amplitude of  $0 \mu\text{V}$  does not correspond to no trapped particles. Perhaps, the deviation occurs because the shape of the ion beam is changed too much by the variation of the exit disc voltage. This would cause a change of the transmission of the ion optics and thus reduce or increase the amount of trapped particles according to Section 4.1.2.

Figure 5.13 shows the influence of the ion number on the frequency ratio. Within the error bars no significant influence of the total number of ions can be detected, but for large ion numbers the error increases. This probably happens because Coulomb interaction forces the ion cloud to spread over a larger volume in space. Due to the anharmonicities of the trap, the ions lose their phase coherence, which results in lower Fourier amplitudes as seen in Fig. 5.4.

Even though no significant frequency ratio shift as a function of the total number of stored ions could be observed in Fig. 5.13, the effect of the Coulomb interaction is not negligible. This becomes obvious, if one tries to excite  ${}^6\text{Li}^+$  before  ${}^7\text{Li}^+$ : No peak in the Fourier spectrum can be observed – not even with higher excitation amplitudes. The underlying reason is most probably that a large cloud of  ${}^7\text{Li}^+$  shields the less abundant  ${}^6\text{Li}^+$  from the excitation signal. However, if  ${}^7\text{Li}^+$  is excited first, the two ion clouds are separated and  ${}^6\text{Li}^+$  can be excited.

Another example of Coulomb screening is shown in Fig. 5.14. The modified cyclotron frequency from the

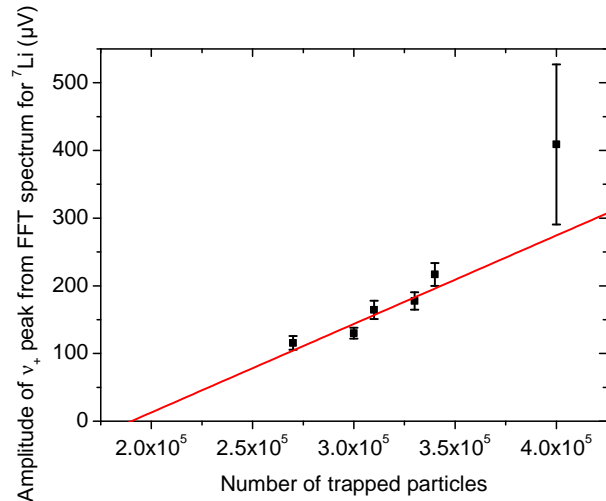


Fig. 5.12: Amplitude of the modified cyclotron peak for varying ion numbers. If the ions move coherently, the amplitude is proportional to the ion number. A linear fit to the data points is shown in red. The extrapolation to  $0 \text{ V}$  FFT amplitude does not correspond to zero ions. This suggests that the beam shape does not stay constant for varying exit disc voltages, which causes a change in the transmission as discussed in Section 4.1.2.

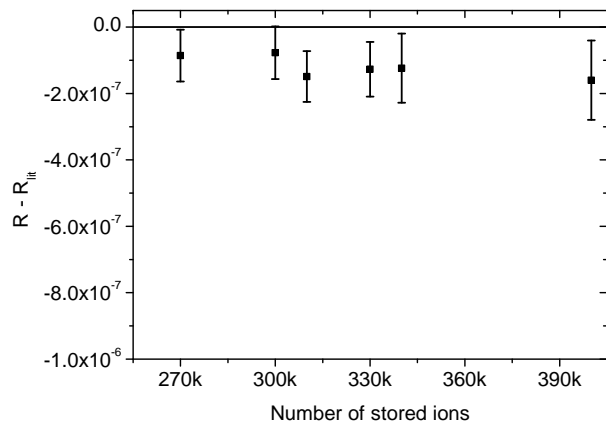


Fig. 5.13: The effect of Coulomb interaction on the deviation of the frequency ratio from the mass ratio of lithium ions for different number of ions. There is no significant trend regarding the ion number. The error bars include the systematic shift because of a non-vanishing magnetron radius, which is most probably the reason for the observed shift to lower frequency ratios. The error bar on the literature value of the mass ratio is too small to be visible. For details see text.

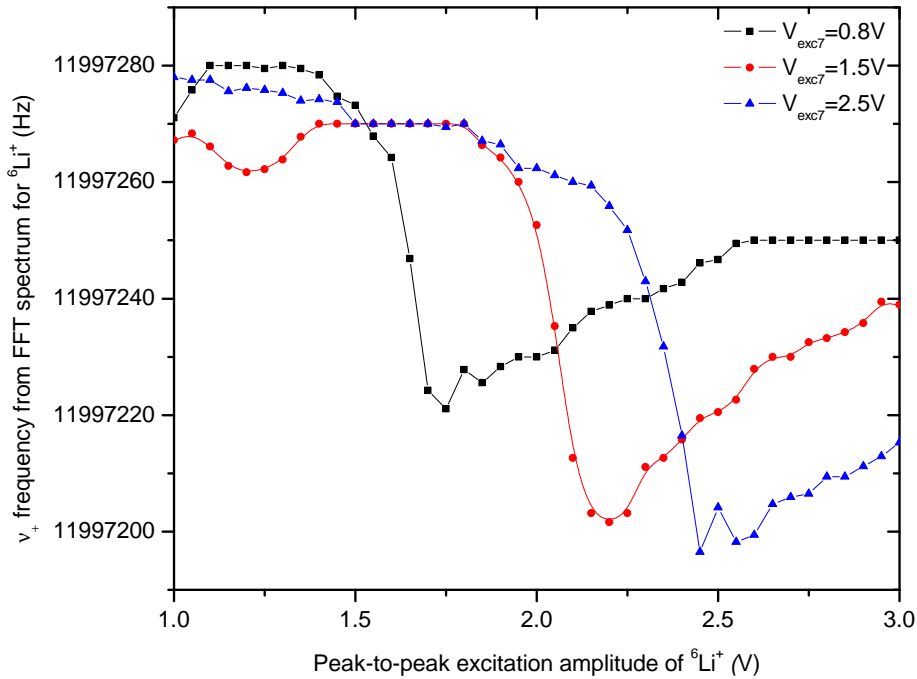


Fig. 5.14: The effect of Coulomb screening on the modified cyclotron frequency of  ${}^6\text{Li}^+$ . The modified cyclotron frequency  $\nu_+$  of  ${}^6\text{Li}^+$  is plotted versus the excitation voltage for various excitation amplitudes of  ${}^7\text{Li}^+$  ( $V_{\text{exc}7}$  (0.8V (black), 1.5V (red) and 2.5V peak-to-peak (blue))). Since  ${}^7\text{Li}^+$  is excited first, the  ${}^6\text{Li}^+$  cloud is shielded by the  ${}^7\text{Li}^+$  ions. Depending on the excitation voltage of  ${}^7\text{Li}^+$ , there is a sudden drop of the frequency. Most probably this is when the two separate ion clouds are at the same radius and thus the Coulomb force is maximal. For higher excitation voltages of  ${}^7\text{Li}^+$ , it becomes easier to reach the point of equal radii because the screening effect is decreasing as the two ion species are separated.

FFT spectrum for  ${}^6\text{Li}^+$  is plotted versus the excitation amplitude of  ${}^6\text{Li}^+$  for different excitation amplitudes of  ${}^7\text{Li}^+$ . Since  ${}^7\text{Li}^+$  is excited first, the more abundant  ${}^7\text{Li}^+$  ions shield the excitation field from the less abundant  ${}^6\text{Li}^+$  ions. Thus, it requires high excitation amplitudes for  ${}^6\text{Li}^+$  to reach equal modified cyclotron radii for both ion species. This equality can be seen in the scans as a sudden frequency drop because the Coulomb force is maximal in this condition. For 0.8V excitation amplitude of  ${}^7\text{Li}^+$ , 1.6V are required as excitation amplitude for  ${}^6\text{Li}^+$  to reach equal radii. However, for 2.5V excitation amplitude of  ${}^7\text{Li}^+$ , only 2.5V are needed for  ${}^6\text{Li}^+$ . Most probably, the Coulomb screening decreases by the large modified cyclotron radius of the  ${}^7\text{Li}^+$  cloud.





## 6 Final test of the KATRIN Penning trap installation

Before the Penning traps are delivered to the KATRIN experiment a final operation test was performed at the MPIK. The two Penning traps for the set-up are assembled, equipped with the preamplifier and the filter board and cabled. One trap was tested regarding its electronics at cryogenic temperatures and then ion trapping was performed with both traps in a room temperature set-up.

### 6.1 Cryogenic test of the KATRIN preamplifier

The preamplifier had to be tested at cryogenic temperatures with the ring electrodes connected to see whether the expected voltage noise density could be reached and whether any unwanted oscillations occur. These tests are necessary because the detection electrodes add a capacity to the input of the preamplifier. This capacity can cause oscillations and can pick up stray signals which increase the detected noise.

As a first step the transfer function of the preamplifier was determined. The amplification of the preamplifier depends on the frequency  $\nu$ . This behaviour has to be described by a low and a high pass. The low pass at  $\nu_l = 65$  MHz is given by

$$V_{\text{out}} = V_{\text{in}} \frac{1}{\sqrt{1 + \left(\frac{\nu}{\nu_l}\right)^2}}. \quad (6.1)$$

Where  $V_{\text{out}}$  and  $V_{\text{in}}$  are output and input voltage respectively. For low frequencies a high pass at  $\nu_h = 0.38$  MHz has to be taken into account:

$$V_{\text{out}} = V_{\text{in}} \frac{\frac{\nu}{\nu_h}}{\sqrt{1 + \left(\frac{\nu}{\nu_h}\right)^2}}. \quad (6.2)$$

So the combined transfer function of the preamplifier

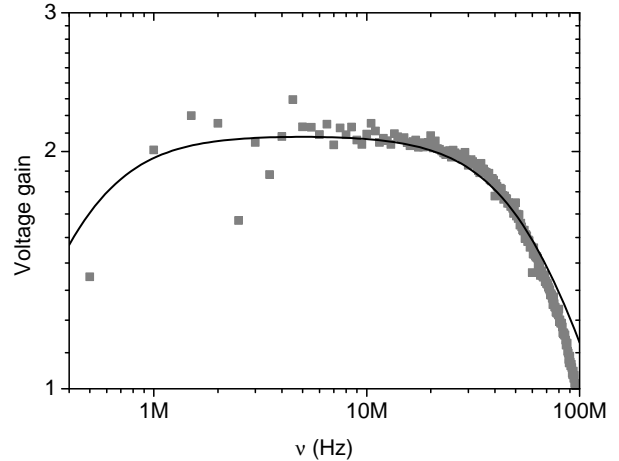


Fig. 6.1: Transfer function of the preamplifier shows two regimes: Below 380 kHz a high pass reduces the gain and above 65 MHz a low pass appears. These limits on the frequency range should be of no concern for the KATRIN experiment. The transfer function is plotted in black, data points in dark gray. The data points were scaled to match with the amplification of the supply voltage (3.3 V). Courtesy of Michael Heck.

with an amplification factor  $G$  is given by

$$V_{\text{out}} = V_{\text{in}} G \frac{1}{\sqrt{1 + \left(\frac{\nu}{\nu_l}\right)^2}} \frac{\frac{\nu}{\nu_h}}{\sqrt{1 + \left(\frac{\nu}{\nu_h}\right)^2}}. \quad (6.3)$$

The effect of this equation is illustrated in Fig. 6.1.

The Penning trap assembly (with the preamplifier and electrodes connected) was put in a cooled vacuum chamber to test the electronics. Liquid nitrogen was used for cooling and the temperature was monitored using a PT-100 element. The trap housing was at approximately 100 K during the experiment. The preamplifier is made of GaAs transistors which operate down to 4 K, so the freeze out of charge-carriers is avoided.

Furthermore, the signal was increased by the room temperature postamplifier made by Stahl-Electronics.

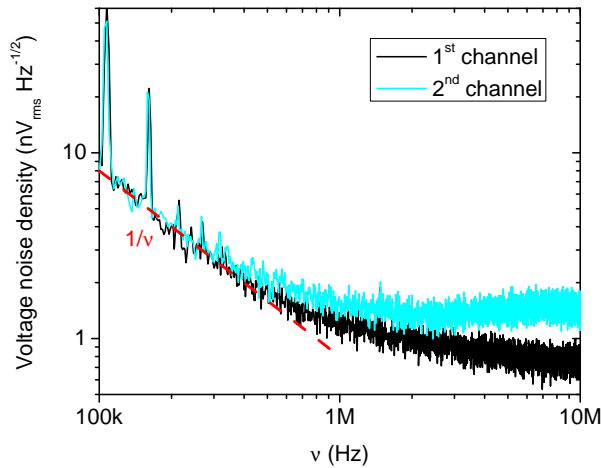


Fig. 6.2: Voltage noise density of the preamplifier as a function of frequency  $\nu$ . The regime of  $1/\nu$  noise is clearly visible (dashed red line). The voltage noise density in the white noise regime (above 1 MHz) is less than  $2 \text{ nVHz}^{-1/2}$ . Both channels show a similar behaviour. Some oscillations are visible but appear at frequencies that are not critical for KATRIN.

To limit induced noise, the amplifier was connected directly to the feedthroughs with BNC connectors and put into an aluminium box. The power supply of the preamplifier was provided by the postamplifier.

A PicoScope 3224 from Pico Technology<sup>1</sup> was used to record the voltage spectrum of each channel. To obtain the voltage noise density, the data were divided by the square root of the frequency width of each channel. Furthermore, the amplitudes were divided by  $\sqrt{2}$  to convert the peak to root-mean-square values. As we are interested in the noise of the preamplifier, the gain of the postamplifier ( $19\times$ , independent of the applied frequency) was taken into account. For the gain of the preamplifier a factor of 2.1 was measured at 3.3 V supply voltage. This value differs from the gain of 5.0 given in Section 3.5.1.1 because of a different termination of the signal line and a slightly different supply voltage.

Using the transfer function of Eq. (6.3) and the gain  $G$  of the preamplifier, the voltage noise density of the two channels can be measured. The result is illustrated in Fig. 6.2. Clearly the two regimes of  $1/\nu$  noise and white noise are visible; the corner frequency is about 1 MHz. The voltage noise density is nearly the same for both channels and is below  $2 \text{ nVHz}^{-1/2}$ . This value is similar to the  $< 1 \text{ nVHz}^{-1/2}$  in [UD11, p. 58]. The difference can be explained by the connected electrodes. Their capacitance will pick up stray signals easily. All

in all, the value is within the expectation for GaAs transistors and will be sufficient to detect unwanted ions in the KATRIN beam line. More measurements of the preamplifier (for example the current noise density) with open inputs are found in [UD11, Hec12].

Some oscillations are visible around 100 kHz in Fig. 6.2. However, they are far from the expected frequencies of the KATRIN experiment (5.1 to 38 MHz according to [UD11, p. 34] and should not pose any problem. The position and the amount of these oscillations depend strongly on the supply voltage which was changed until the least oscillations were visible in the spectrum. This leads to a value of 3.3 V. For a detailed oscillation measurement a Hameg<sup>2</sup> HM5014-2 1 GHz Spectrum Analyzer was connected to the output of each channel consecutively because it has a higher bandwidth than the PicoScope.

## 6.2 Trapping of ions

To test the functionality of the ion traps, all equipment was connected in the same manner as it will be done in the KATRIN experiment. For the high voltage, an HV 500 from Stahl-Electronics was used. For switching the endcap voltage a GHTS 60 from Behlke<sup>3</sup> was taken from the MPIK set-up. These were the only devices employed in the operational test that will not be transferred to the KATRIN set-up; equivalent equipment will be supplied by Stahl-Electronics. For triggering, the Pulse Generator 575-2C by FAST ComTec<sup>4</sup> was used. The signal was created using the Tabor Electronics<sup>5</sup> WW 1071 function generator with a user defined SWIFT excitation from 10285210 to 10285410 Hz with constant amplitudes in the frequency spectrum and a length of 18 ms. The overall peak-to-peak amplitude of the SWIFT signal was set to 10 V. The KATRIN Penning trap PC was used to control all devices and for the data acquisition. A scheme of the connections of the different devices is shown in Fig. 6.3. Only one excitation electrode of the Penning trap was connected to the function generator. The other electrode was grounded.

1. Pico Technology Ltd., James House, Marlborough Road, Colmworth Business Park, Eaton Socon, St Neots, Cambridgeshire, PE19 8YF, United Kingdom

2. HAMEG Instruments GmbH, Industriestr. 6, D-63533 Mainhausen, Germany

3. Behlke Power Electronics GmbH, Am Auernberg 4, D-61476 Kronberg im Taunus, Germany

4. FAST ComTec Communication Technology GmbH, Grünwalder Weg 28A, D-82041 Oberhaching, Germany

5. Tabor Electronics Ltd., 9 Hatasia St., Tel Hanan, Israel

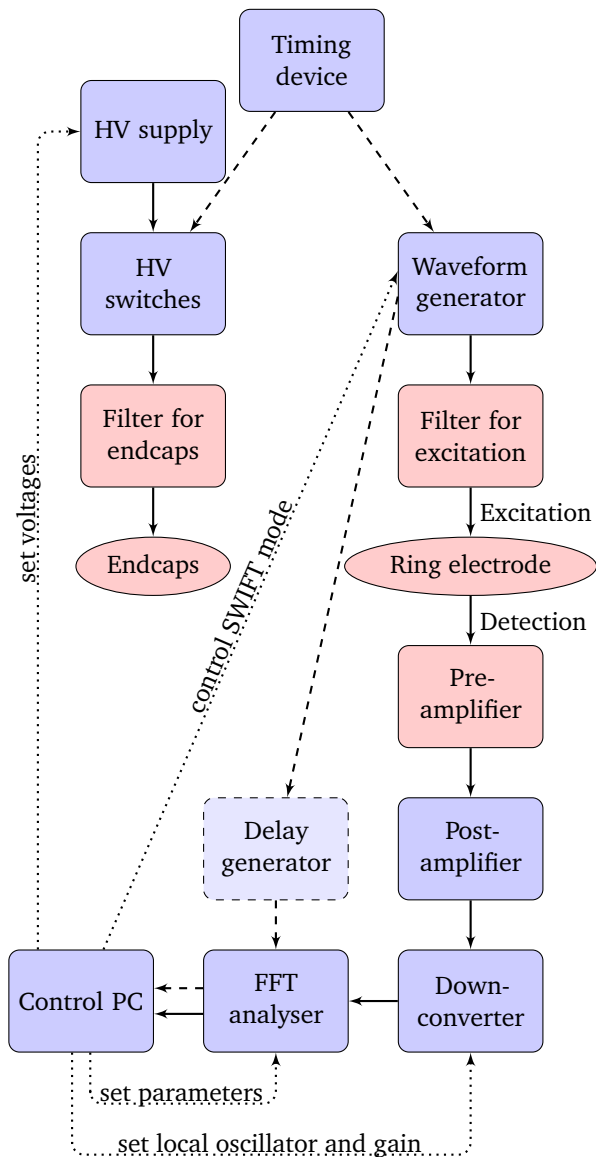


Fig. 6.3: Connection of the KATRIN devices. Signal lines are represented by a thick line; dashed lines represent the trigger and dotted lines mark the various control mechanisms. The delay generator (light blue) introduces a waiting time of approximately  $50 \mu\text{s}$  after excitation. It is not strictly necessary (for details see text). Devices that are in the vacuum chamber are marked in red. The start trigger is given every  $0.5 \text{ s}$  by the timing device.

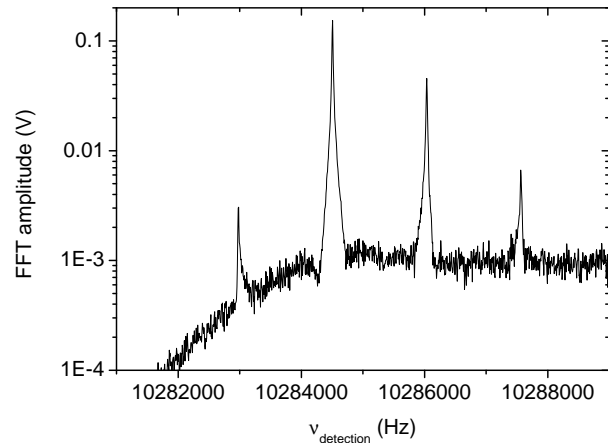


Fig. 6.4: A typical FT-ICR spectrum taken with the OR35 FFT analyzer and corrected by the local oscillator frequency of the down-converter. Only one detection electrode was used for the FT-ICR spectrum, thus all combinations of sidebands are visible. From left to right the following peaks are depicted  $\nu_+ - \nu_-$ ,  $\nu_+$ ,  $\nu_+ + \nu_-$ ,  $\nu_+ + 2\nu_-$ . A filter in the down-converter causes the drop of background noise towards low frequencies. The signal of the second detection electrode looks exactly alike.

The detection signal was amplified with the pre- and postamplifier and connected to the FD1-40 down-converter by Stahl-Electronics. The down-converted signal was then Fourier transformed and recorded for  $160 \text{ ms}$  with the OROS<sup>6</sup> OR35 NV Gate spectrum analyser. The down-converter is necessary because the bandwidth of the spectrum analyser is limited to  $40 \text{ kHz}$ .

A delay generator introduced a waiting time of approximately  $50 \mu\text{s}$  after excitation and was added for convenience because this time shift limits induced signals. This device is not strictly necessary since the same effect can be achieved by a removal of the first  $0.1 \text{ ms}$  from the signal of the FFT analyser or by introducing a waiting period in the user defined waveform for the SWIFT excitation.

Figure 6.4 displays the observed signal of  ${}^7\text{Li}^+$  on one electrode. Both electrodes were connected, but recorded separately to confirm an equal amplification of the signal. The frequency scale of Fig. 6.4 was calculated from the local oscillator of the down-converter and the recorded spectrum. The known shift of the modified cyclotron frequency with the trapping potential could

6. OROS SA, 23, chemin des Prés, ZIRST 4403, F-38944 MEYLAN cedex, France

be verified to be close to the expectation of  $15 \text{ Hz V}^{-1}$ . Together with the detection of the sideband peaks this confirms that the traps are operational. In Fig. 6.4 more sidebands are visible than in pure dipolar or quadrupolar detection schemes. The reason is that the selection rules from Section 2.4 do not exist for single electrode detection. Thus, the sum frequency and the modified cyclotron frequency are visible in the same plot. Additionally, the difference of frequencies  $\nu_+ - \nu_-$  and the sideband at  $\nu_+ + 2\nu_-$  can be seen. As expected, the modified cyclotron motion causes the highest peak. A good explanation why the peaks are asymmetric and of different height is available in [Kre12]. A low pass in the devices leads to the drop of the noise level that is observed for frequencies smaller than  $10\,284\,000 \text{ Hz}$  and has no physical meaning.

One measurement cycle (including in- and ejection of ions) takes approximately  $300 \text{ ms}$ , a time which is limited at the lower end by the time needed to apply the signal ( $\approx 20 \text{ ms}$ ) and the time needed to detect the signal with the wanted accuracy ( $160 \text{ ms}$  for  $6.25 \text{ Hz}$  bin width). The upper limit is set by the coherence time of the ions which is approximately  $20 \text{ ms}$  at  $1 \times 10^{-7} \text{ mbar}$  [UD11, p. 65].

Furthermore, a few minor changes had to be done to the trap housing: The aluminium screws that attach the holder ring to the trap got stuck in their aluminium threads. This caused the screws to break off once they were turned further. So new threads were milled and titanium screws ordered to solve the problem.

## 7 Conclusion and outlook

The off-line tests of the Penning traps for the Karlsruhe TRItium Neutrino experiment (KATRIN) at the Max-Planck-Institut für Kernphysik (MPIK) have been performed. The accuracy of the frequency ratio determination  $(R - R_{\text{lit}})/R_{\text{lit}}$  was increased by an order of magnitude compared to [UD11]. Depending on the excitation and detection schemes a value of  $3 \times 10^{-7}$  can be reached. Additionally, the resolving power needed to detect T and  ${}^3\text{He}$  simultaneously, which is  $(1 \times 10^4)$ , will be reachable with the KATRIN traps: A Fourier width of less than 10 Hz was observed at a frequency of approximately 10 MHz, which results in a resolving power of  $1 \times 10^6$ .

The homogeneous region of the MPIK magnet was mapped in great detail, but could not be improved much. The magnet was shimmed, but two of the three shim coils are not (dis)chargeable any more. The magnetic bottle term  $B_2$  could be reduced by a factor of three compared to the measurements presented in [UD11]. It could be shown that the detected distortion of the magnetic field is most probably due to still charged shim coils. The inhomogeneous  $B$  field causes an initial magnetron motion because it deflects charged particle from the trap centre. So currently, the set-up is limited to experiments that do not rely on initially centred particles.

A Simion workbench for the whole set-up was created. This will allow further systematic studies of the trapping procedure. Additionally, this Simion workbench was used to simulate the trapping efficiency and trapping location for different trapping voltages. The simulation was done with a homogeneously filled beam tube which should be a similar condition as the one in the KATRIN beam line. It could be shown that high trapping potentials cause an axial compression for ions at the trap's centre but not for ions close to the electrodes. Furthermore, it was seen that trapping occurs more easily close to the electrodes. The number of trapped particles can be estimated depending on their energy and the trapping potential according to Section 4.1.3, which resulted in  $5 \times 10^4$  ions per nA transmission current for typical settings at the MPIK set-up.

Two excitation schemes (dipole excitation and quadrupole conversion) and different detection schemes (dipole, quadrupole and a combined method) were compared regarding their accuracy. No major differ-

ence could be observed. All investigated combinations showed an accuracy of  $(R - R_{\text{lit}})/R_{\text{lit}}$  in the range of  $3 \times 10^{-7}$  to  $6 \times 10^{-7}$  for  ${}^6\text{Li}^+$  and  ${}^7\text{Li}^+$  ions. However depending on the exact conditions each method has its own advantages as mentioned in Section 5.3.5: If an extrapolation to 0 V trapping potential is not possible, it is usually advantageous to use a quadrupolar pulse and convert all initial magnetron radius to modified cyclotron radius. On the other hand, if high signal-to-noise ratios are needed the detection at the modified cyclotron frequency works best. If there is no initial magnetron motion present, then it is advisable to detect the sum frequency of the different ion species as a function of the excitation amplitude. The shifts of the sum frequencies of  ${}^6\text{Li}^+$  and  ${}^7\text{Li}^+$  were used to estimate the reduced cyclotron radius and the electrostatic imperfections of the trap.

Final tests of all three Penning traps and all equipment for KATRIN are completed. All devices are in a working condition and the Penning traps are assembled and cabled. The preamplifier has been tested at 100 K and showed the expected voltage noise density of  $2 \text{ nV Hz}^{-1/2}$ . No unwanted oscillations were detectable. Ions could be observed in the room temperature set-up of the MPIK for each trap. The known shift of the modified cyclotron frequency with the trapping potential was verified. The coherence time of the ions was high enough to enable resolving powers higher than  $1 \times 10^6$ . At 10 MHz this corresponds to approximately 100 ms. The devices will be delivered to KATRIN by Stahl-Electronics as soon as possible.

The future project at the MPIK set-up is called Piperade (PIège de Penning pour des ions Radioactifs à DEsir) [PIP12]. This Franco-German collaboration aims at using a system of two Penning traps or one Penning trap and one Multiple-Reflection Time-Of-Flight Mass Spectrometer (MR-TOF-MS) to clean and accumulate exotic nuclei. Several studies which might also be interesting for KATRIN will have to be carried out. The maximum loading capacity of the current traps will be investigated. This value is important for KATRIN because there are hints that ions are only observed, if the maximum loading capacity is not reached. Furthermore, cleaning tests will be carried out. The results of these experiments will most certainly allow KATRIN to detect less abundant contaminants more easily. Addi-

tionally, the Coulomb interaction will be studied with an electron impact source. Thus, the abundance of contaminants can be varied freely. Last but not least, the use of high performance Graphics Processing Units (GPUs) at the MPIK will enable the group to simulate large ion numbers ( $> 2000$ ) with the Simbuca[VG12] programme.

# Bibliography

- [AAA<sup>+</sup>08] B. Aharmim, S. N. Ahmed, J. F. Amsbaugh, et al. Independent Measurement of the Total Active  $^8\text{B}$  Solar Neutrino Flux Using an Array of  $^3\text{He}$  Proportional Counters at the Sudbury Neutrino Observatory. *Phys. Rev. Lett.*, 101:111301, 2008.
- [ABB<sup>+</sup>02] C. E. Aalseth, A. S. Barabash, F. Böhm, et al. Comment on ‘Evidence for Neutrinoless Double Beta Decay’. Evidence for Neutrinoless Double Beta Decay. *Mod. Phys. Lett. A*, 17(hep-ex/0202018):1475–1478. 4 p, 2002.
- [ABB<sup>+</sup>11] V. N. Aseev, A. I. Belesev, A. I. Berlev, et al. Upper limit on the electron antineutrino mass from the Troitsk experiment. *Phys. Rev. D*, 84:112003, 2011.
- [And62] P. W. Anderson. Theory of Flux Creep in Hard Superconductors. *Phys. Rev. Lett.*, 9:309–311, 1962.
- [BAB<sup>+</sup>12] J. Beringer, J. F. Arguin, R. M. Barnett, et al. Review of Particle Physics. *Phys. Rev. D*, 86:010001, 2012.
- [BCG<sup>+</sup>96] R. M. Barnett, C. D. Carone, D. E. Groom, et al. Review of Particle Physics. *Phys. Rev. D*, 54:1–708, 1996.
- [BG86] L. S. Brown and G. Gabrielse. Geonium theory: Physics of a single electron or ion in a Penning trap. *Rev. Mod. Phys.*, 58:233–311, 1986.
- [BGF<sup>+</sup>12] N. Blumm, G. Ghoshal, Z. Forró, et al. Dynamics of Ranking Processes in Complex Systems. *Phys. Rev. Lett.*, 109:128701, 2012.
- [BJ36] J. Blewett and E. Jones. Filament sources of positive ions. *Physical Review*, 50(5):464, 1936.
- [Bla06] K. Blaum. High-accuracy mass spectrometry with stored ions. *Physics Reports*, 425(1):1–78, 2006. ISSN 0370-1573.
- [CDRD<sup>+</sup>98] B. T. Cleveland, T. Daily, J. Raymond Davis, et al. Measurement of the Solar Electron Neutrino Flux with the Homestake Chlorine Detector. *The Astrophysical Journal*, 496(1):505, 1998.
- [DGG<sup>+</sup>62] G. Danby, J.-M. Gaillard, K. Goulianos, et al. Observation of High-Energy Neutrino Reactions and the Existence of Two Kinds of Neutrinos. *Phys. Rev. Lett.*, 9:36–44, 1962.
- [DHH68] J. Davis, Raymond, D. S. Harmer, and K. C. Hoffman. Search for neutrinos from the sun. *Phys. Rev. Lett.*, 20:1205–1209, 1968.
- [Edd39] A. Eddington. *The Philosophy of Physical Science*. Tarner lectures 1938. Cambridge University Press, 1939.
- [Eic08] F. Eichelhardt. *Measurement of the Tritium Pumping Properties of a 4.2 K Argon Condensate for the Cryogenic Pumping Section of KATRIN*. Ph.D. thesis, Karlsruher Institut für Technologie, 2008.
- [Fer34] E. Fermi. Versuch einer Theorie der  $\beta$ -Strahlen. I. *Zeitschrift für Physik A Hadrons and Nuclei*, 88:161–177, 1934. ISSN 0939-7922. 10.1007/BF01351864.

- [FHI<sup>+</sup>98] Y. Fukuda, T. Hayakawa, E. Ichihara, et al. Evidence for Oscillation of Atmospheric Neutrinos. *Phys. Rev. Lett.*, 81:1562–1567, 1998.
- [FO95] T. Fujii and M. Ohta. Filament thermionic sources of Li<sup>+</sup> ions in low heating power. *Journal of Physics D: Applied Physics*, 28:1268, 1995.
- [Gan91] D. Gant. *Comparison of Alkali Ion Emitters*. Master's thesis, Naval Postgraduate School, Monterey, California, 1991.
- [GFHG12] N. Gravish, S. V. Franklin, D. L. Hu, and D. I. Goldman. Entangled Granular Media. *Phys. Rev. Lett.*, 108:208001, 2012.
- [GM96] S. Guan and A. G. Marshall. Stored waveform inverse Fourier transform (SWIFT) ion excitation in trapped-ion mass spectrometry: Theory and applications. *International Journal of Mass Spectrometry and Ion Processes*, 157–158(0):5 – 37, 1996. ISSN 0168-1176.
- [Hö09] M. Hötzel. *Berechnung von KATRIN Messspektren unter Einbeziehung der Eigenschaften der fensterlosen gasförmigen Tritiumquelle*. Master's thesis, Universität Karlsruhe (TH), 2009.
- [Hec12] M. Heck. *Title to be announced*. Ph.D. thesis, Ruprecht-Karls-Universität, 2012. To be published.
- [KAT02] KATRIN Collaboration. Addendum to the Letter of Intent. Technical report, Forschungszentrum Karlsruhe, 2002.
- [KAT05] KATRIN Collaboration. KATRIN design report 2004. Technical report, Forschungszentrum Karlsruhe, 2005.
- [KBB<sup>+</sup>05] C. Kraus, B. Bornschein, L. Bornschein, et al. Final results from phase II of the Mainz neutrino mass search in tritium  $\beta$  decay. *The European Physical Journal C - Particles and Fields*, 40:447–468, 2005. ISSN 1434-6044. 10.1140/epjc/s2005-02139-7.
- [KK10] H. Klapdor-Kleingrothaus. *Seventy Years Of Double Beta Decay: From Nuclear Physics to Beyond-Standard-Model Particle Physics*. World Scientific, 2010. ISBN 9789812832351.
- [KKDK<sup>+</sup>04] H. Klapdor-Kleingrothaus, A. Dietz, I. Krivosheina, et al. Support of evidence for neutrinoless double beta decay. *Physics Letters B*, 578(1–2):54 – 62, 2004. ISSN 0370-2693.
- [Kre07] M. Kretschmar. The Ramsey method in high-precision mass spectrometry with Penning traps: Theoretical foundations. *International Journal of Mass Spectrometry*, 264(2–3):122 – 145, 2007. ISSN 1387-3806.
- [Kre12] M. Kretschmar. Model calculation of amplitudes for FT-ICR ion detection in a cylindrical Penning trap. *Applied Physics B: Lasers and Optics*, 107:1007–1017, 2012. ISSN 0946-2171. 10.1007/s00340-012-4905-0.
- [KUA<sup>+</sup>01] K. Kodama, N. Ushida, C. Andreopoulos, et al. Observation of tau neutrino interactions. *Physics Letters B*, 504(3):218 – 224, 2001. ISSN 0370-2693.
- [NFS<sup>+</sup>06] S. Nagy, T. Fritioff, M. Suhonen, et al. New Mass Value for <sup>7</sup>Li. *Phys. Rev. Lett.*, 96:163004, 2006.
- [OW08] E. Otten and C. Weinheimer. Neutrino mass limit from tritium  $\beta$  decay. *Reports on Progress in Physics*, 71:086201, 2008.
- [Pau30] W. Pauli. Offener Brief an die Gruppe der Radioaktiven bei der Gauvereins-Tagung zu Tübingen, 1930.



- [PIP12] PIPERADE. Project web page. <http://www.cenbg.in2p3.fr/piperade/>, 2012.
- [RC53] F. Reines and C. L. Cowan. Detection of the Free Neutrino. *Phys. Rev.*, 92:830–831, 1953.
- [Ren11] P. Renschler. *KESS - A new Monte Carlo simulation code for low-energy electron interactions in silicon detectors*. Ph.D. thesis, Karlsruher Institut für Technologie, 2011.
- [RH84] F. Roméo and D. I. Hoult. Magnet field profiling: Analysis and correcting coil design. *Magnetic Resonance in Medicine*, 1(1):44–65, 1984. ISSN 1522-2594.
- [Ric21] O. Richardson. *The emission of electricity from hot bodies*. Longmans, Green and co., 1921.
- [Rod12] V. Rodin. Status of calculations of the nuclear matrix elements for double beta decay. *Journal of Physics: Conference Series*, 375(4):042025, 2012.
- [Sch97] N. Schmitz. *Neutrinophysik*. Teubner Studienbücher: Physik. Teubner, 1997. ISBN 9783519032366.
- [Sch01] K. Scholberg. Supernova neutrino detection. *Nuclear Physics B - Proceedings Supplements*, 91(1–3):331 – 337, 2001. ISSN 0920-5632. Neutrino 2000.
- [Sho38] W. Shockley. Currents to conductors induced by a moving point charge. *Journal of Applied Physics*, 9(10):635–636, 1938. Cited By (since 1996) 269.
- [Sto88] L. Stodolsky. The speed of light and the speed of neutrinos. *Physics Letters B*, 201(3):353 – 354, 1988. ISSN 0370-2693.
- [Stu10] M. Sturm. *Aufbau und Test des Inner-Loop-Systems der Tritiumquelle von KATRIN*. Ph.D. thesis, Universität Karlsruhe, 2010.
- [UD11] M. Ubieto Diaz. *Off-line commissioning of a non-destructive FT-ICR detection system for monitoring the ion concentration in the KATRIN beamline*. Ph.D. thesis, Ruprecht-Karls-Universität, 2011.
- [UDRL<sup>+</sup>09] M. Ubieto-Díaz, D. Rodríguez, S. Lukic, et al. A broad-band FT-ICR Penning trap system for KATRIN. *International Journal of Mass Spectrometry*, 288(1–3):1 – 5, 2009. ISSN 1387-3806.
- [VDMFS89] R. S. Van Dyck, F. L. Moore, D. L. Farnham, and P. B. Schwinberg. Number dependency in the compensated Penning trap. *Phys. Rev. A*, 40:6308–6313, 1989.
- [VG12] S. Van Gorp. *Search for physics beyond the Standard Electroweak model with the WITCH experiment*. Ph.D. thesis, Katholieke Universiteit Leuven, 2012.
- [Wei88] R. M. Weisskoff. *Detecting single, trapped ions*. Ph.D. thesis, Massachusetts Institute of Technology, 1988.
- [Wei02] C. Weinheimer. KATRIN, a next generation tritium  $\beta$  decay experiment in search for the absolute neutrino mass scale. *Progress in Particle and Nuclear Physics*, 48(1):141 – 150, 2002. ISSN 0146-6410.
- [Wei03] C. Weinheimer. Laboratory Limits on Neutrino Masses. In K. Winter and G. Altarelli, editors, *Neutrino Mass*, volume 190 of *Springer Tracts in Modern Physics*, pages 138–140. Springer Berlin / Heidelberg, 2003. ISBN 978-3-540-40328-9. 10.1007/978-3-540-44901-0\_2.

# Danksagung

Vielen Dank an Klaus Blaum und Guido Drexlin, die diese Arbeit erst möglich gemacht haben.

Danke (merci beaucoup, teşekkür ederim, muchas gracias) auch an die Mitglieder des FT-ICR-Labors, Michael, Pauline, Burcu und Marta, ich hoffe ihr hattet soviel Spaß wie ich. Danke fürs Korrekturlesen.

Für die Diskussionen und einige Ideen vielen Dank an Stefan und Lutz.

Danke Andreas für das lustige Jahr in unserem Büro und die Informationen über die Stabilität von Rankings [BGF<sup>+</sup>12] und was für dröge Tätigkeiten andere in ihren Diplomarbeiten machen müssen: Tackernadeln kürzen [GFHG12].

Natürlich auch ganz viele Grüße an alle Mitglieder unserer Nachbarexperimente Pentatrap und The Trap, die mir immer tatkräftig (wenn auch machmal unwissentlich) mit Funktionsgeneratoren, Picoamperemetern und Rat und Tat ausgeholfen haben.

Danke Kaija für deine freiwillige Mithilfe beim Girls Day.

Danke an Ralph für deine unglaubliche Ausdauer während des Magnetfüllens und an Frau Dücker für Ihre organisatorische Unterstützung. Sowie allen Mitarbeitern und Gästen des MPIK für die erfolgreiche Zeit hier.

Danke an die Mönchgasse 4! Besonders Lisa und Mio.

Ein herzliches Dankeschön geht an Eva und meine Eltern!